FACULTY OF MATHEMATICS, PHYSICS AND INFORMATICS
COMENIUS UNIVERSITY
BRATISLAVA

Department of Nuclear Physics

Neutron Cross Sections and Interactions of Cosmic Ray Particles with Terrestrial and Extraterrestrial Matter

PhD thesis

RNDr. Daniel Kollár

Bratislava 2003

To Monika

Supervisor: Prof. RNDr. Jozef Masarik, DrSc.

Co-Supervisor: Prof. Dr. rer. nat. Rolf Michel

Abstract

A purely physical model based on a Monte Carlo simulation of GCR particle interaction with meteoroids was used to investigate neutron interactions down to thermal energies. Experimental and/or evaluated excitation functions were used to calculate neutron capture production rates as functions of size of the meteoroid and depth below its surface. Presented are the depth profiles of cosmogenic radionuclides ^{36}Cl, ^{41}Ca, ^{60}Co, ^{59}Ni, and ^{129}I for meteoroid radii from 10 cm up to a 2π irradiation. Effects of bulk chemical composition on n-capture processes are studied and discussed for various chondritic and lunar compositions. The mean GCR particle flux over the last $\approx$ 300 ka was determined from comparison of simulations with measured ^{41}Ca activities in Apollo 15 drill core. The determined value significantly differs from that obtained using equivalent models of spallation residue production.

Currently, two different sets of cross sections are used in geochemical and cosmochemical applications for spallogenic nuclide production in extraterrestrial matter. Here these sets were used for calculation of the production of cosmogenic radionuclides ^{7}Be and ^{10}Be in the Earth's atmosphere and ^{10}Be, ^{14}C, ^{21}Ne, ^{26}Al, and ^{36}Cl in terrestrial surface rocks. For the atmosphere, the production rates calculated using the two sets are not equivalent. For nuclide production on the surface, the two sets give similar results.

Within the HINDAS project, neutron activation experiments were performed in order to determine excitation functions for the production of residual nuclides up to neutron energies of 175 MeV. Here Monte Carlo simulations of neutron transport were performed for 22 irradiations in which the target stacks were irradiated with a quasi-monoenergetic neutron beam from reaction $^{7}\mathrm{Li}(p,n)$. The neutron transport calculations were performed using the LAHET Code System resulting in full neutron spectrum for each foil in an irradiated target stack. In the evaluation the spectra will be used together with measured nuclide activities for the unfolding of final excitation functions.

Acknowledgements

I am very grateful to many people who have contributed directly and indirectly to the completion of this work. First, I would like to thank to my supervisor Jozef Masarik for introducing me to the world of applied nuclear physics and directing me to the study of cosmogenic nuclides production. I am especially grateful to him for his support not only as a supervisor but also as a man, for his valuable time, many times to the detriment of his family.

Big part of the work was done during my stay at the Center for Radiation Protection and Radioecology, University of Hanover, Germany in years 2000 and 2002. I am very grateful to prof. Rolf Michel, who welcomed me at the institute. I wouldn't come too far without valuable discussions we had concerning cosmogenic nuclides, models, neutron cross sections and the activation experiments. I cannot imagine this work been done without him. Many thanks also go to Wolfgang Glasser for discussing the neutron activation experiments. I also want to thank to the whole institute staff for making me feel like at home. Special thanks go to Ulrike Müller and Jürg Lüdtke.

I also have to thank to Ingo Leya (ETH, Zürich) and Robert C. Reedy (LANL) for many enlightening scientific discussions concerning neutron cross sections and problems of cosmogenic nuclide production modeling.

Thanks go to my colleagues at the department for helping me to solve everyday problems and to my friends for the support and fun during the years.

I thank to my parents, brother and sister for their continuous support to my work.

Finally, I am greatly thankful to my wife Monika for her love, patience and support.

Table of contents

1 Introduction

In a classical epoch of the studies of cosmic ray traces in matter starting early 50's and ending with the investigation of first lunar samples two main things were accomplished. First, methods were developed for the detection of a wide range of transformations induced in matter by cosmic rays (CR). Second, using the data measured with these methods, models were developed that demonstrated that CR induced processes were running also in a distant past and that the mean galactic cosmic ray (GCR) and solar cosmic ray (SCR) intensities, according to the traces in matter, remain approximately constant.

At present, new models are developed that simulate more precisely all the processes involved with cosmic ray interactions in matter. Using the experimental data, precise models make it possible to reconstruct the history of the individual objects of the Solar system as well as of the Solar system as a whole.

Two types of models have been used to describe the interactions. One uses thick target bombardments [e.g. 1, 2] to simulate the natural conditions well enough to calculate nuclide production. This approach has the advantage of a fairly close relation between the laboratory experiment and the natural event. The other is to calculate the spectrum and the flux of nuclear particles at given depths inside an irradiated object theoreticaly. The flux is then used, along with the excitation function for each reaction of interest, to calculate the production at these depths. This approach is more easily related to the fundamental physics and therefore is easier to improve and extend as new data and theories appear.

Theoretical models differ in a way they calculate the depth dependent particle spectra and fluxes. Older models mostly tried to describe the dependencies using various analytical functions that were constructed considering available physical theories and experimental data [e.g. 3–5]. With advent of the computer era, stochastic models using Monte Carlo simulation of particle cascade in matter have been used [e.g. 6–8].

Most of these models use for the calculation of the cosmogenic nuclide (CN) production rates the nuclear cross sections. The availability of exact excitation functions for individual nuclear reactions is crucial for the applicability of the models to the cosmochemical, geochemical, geochronological and many other applications. However, there are many reactions for which the experimental excitation functions are incomplete or completely missing. For proton induced reactions relevant in cosmic ray studies this is usually not the case, since there

has been a great effort dedicated to the proton cross section measurements in thick and thin target experiments in the last two decades.

With neutrons, the situation is much more complicated as its zero electric charge does not allow for simple monoenergetic cross section measurements at energies above ≈ 14 MeV. Therefore, various indirect methods are used to fill the gaps in neutron excitation functions. There are many cases when the results from these methods do not agree with each other and one has to decide which set of cross sections is more suitable for a particular application.

Three main topics are covered in this work. First, a model for neutron capture production of cosmogenic nuclides in extraterrestrial matter is presented. A motivation for this part of work was the nonexistence of systematics for (n, γ) reactions in meteorites and planetary surfaces based on Monte Carlo simulation of particle transport. For spallation reactions such systematics exist [7, 8]. Similar model was partially used several times before [e.g. 9, 10] but no thorough investigation of all its aspects was done. Here such investigation is presented. This model aims to extend Monte Carlo models for spallation reactions down to thermal neutron energies to allow for application to complex problems in meteoritics and planetary science.

At present, two sets of cross sections are used for the simulation spallation production of cosmogenic nuclides in extraterrestrial matter. The excitation functions included in these sets differ for some reactions by more than 100% in wide energy ranges. Another topic covered in this work is the application of the two sets to the simulation of cosmogenic nuclide production in the Earth's atmosphere and surface rocks.

Besides the applications in space science, cross sections for the production of residual nuclides are of importance for many other fields of basic and applied sciences ranging from enviromental sciences, medicine, space and aviation technology to *accelerator driven transmutation of waste* (ADTW) and *energy amplification* (ADEA). The particular problem for accelerator driven technologies is that the data needs are extreme with respect to both, target element coverage and types of reaction data. Since it is practically impossible to measure all relevant data, one has to rely to a large degree on theoretical estimates. Given the fact that the predictive power of present day models and codes does not satisfy the requirements [11], an initiative was taken by a number of European laboratories to improve this situation. This initiative was realized in the 5th European Framework project HINDAS – *High- and Intermediate-Energy Data for Accelerator-Driven Systems* [12].

The author is a member of a group which works on a work-package 3 of HINDAS project, namely the production of residual nuclides by proton- and neutron-induced reactions. Last part of this work covers neutron transport Monte Carlo calculations for neutron activation experiments which are used for the determination of neutron excitation functions.

* * *

The work is divided into six chapters, references and three appendices. In chapter 1 basic

concepts of cosmic ray interactions with the Solar system matter are reviewed and an overview of history and classification of meteorites is given. Also the present state and methods used for modeling the cosmogenic nuclide production are described. In chapter 2 particular aims and problems concerned with in this work are listed.

In chapter 3 a model for neutron capture production of cosmogenic nuclides in extraterrestrial matter is presented and tested on experimental data measured in lunar samples. Chapter 4 covers the test and comparison of two different sets of nuclear cross sections when applied to numerical simulation of cosmogenic nuclide production in the Earth's atmosphere and surface rocks. In chapter 5 the simulation of neutron transport for neutron activation experiments is described.

Chapter 6 concludes the work presenting the summary and value of results and outlines the problems that need future investigation.

The work has three appendices that contain the examples of input files for the Monte Carlo calculation, all used proton and neutron excitation functions, and the basic parameters for all simulated neutron irradiations.

1.1 Cosmic rays

The primary CR flux at the Earth's orbit consists mainly of protons, α-particles and some heavier nuclei, electrons, and photons. As this work concerns isotopic changes of nuclei, under CR we will further consider only those particles of primary radiation, that are atomic nuclei and have enough energy to induce nuclear transitions.

From the aspect of origin, CR can be divided into two main parts, galactic and solar, that differ in particle composition, energy distribution, radiation intensity and nature of its temporal variations. While most of SCR particles have energies under 100 MeV, differential flux density of GCR particles is highest for energies $\sim$ 1 GeV and there are still many particles with energies $\sim$ 10 GeV and higher. Tab. 1.1 shows energy ranges and mean flux densities of particles of both components of CR at the Earth's orbit. These characteristics determine the way in which particles of each component interact with terrestrial and extraterrestrial matter. The SCR particles and heavier GCR nuclei are stopped in the upper layers of the irradiated object by ionisation, light GCR particles penetrate much deeper and induce nuclear reactions.

1.1.1 Galactic cosmic rays

GCR consists of $\sim$ 87% protons, $\sim$ 12% α-particles and $\sim$ 1% heavier nuclei [14]. It is an isotropic radiation with origin outside the Solar system. Its particles are injected into the interstellar medium by supernova explosions and accelerated by a variety of complicated processes and occasionally attain extreme energies up to $\sim 10^{24}$ eV [15]. GCR particles differential energy distribution in the interstellar space can be for energies over a few GeV

Table 1.1: Energies and mean flux densities of CR particles [13].

Radiation type	Energy [Mev nucleon^{-1}]	Mean flux density [particle cm^{-2} s^{-1}]
SCR		
Protons & α-particles	$5-10$	~ 100
Heavier nuclei	$1-50$	~ 1
GCR		
Protons & α-particles	$100-3000$	3
Heavier nuclei	~ 100	0.03

roughly described as

$$\frac{\mathrm{d}J}{\mathrm{d}E} = \text{const.}\,(1000+E)^{-2.65}\,, \tag{1.1}$$

where kinetic energy E is given in MeV [3]. For energies $E > 10$ GeV this dependence can be approximated to the power law in energy, $\sim E^{-2.65}$.

When entering Solar system, GCR particles interact with heliomagnetic field which is carried away from the Sun by the solar wind. This leads to scattering, diffusion and loss of energy and causes a modulation of energy spectra of particles that is substantial mainly for energies below 1 GeV. This modulation takes place within heliosphere reaching distance of ~ 50 AU.

The differential flux density of GCR protons near Earth is described introducing solar modulation parameter Φ [MeV] which represents the energy loss of a particle entering the Solar system and propagating to a certain heliocentric distance. This parameter is included in the semiempiric formula of Castagnoli and Lal [16]

$$\frac{\mathrm{d}J}{\mathrm{d}E} = A\,\frac{E\,(E+2E_0)\,(E+\Phi+m)^{-\gamma}}{(E+\Phi)\,(E+2E_0+\Phi)}\,, \tag{1.2}$$

where E is the kinetic energy of proton, E_0 is its rest energy, $A = 9.9\times10^8$ protons cm^{-2} s^{-1} MeV^{-1}, $m = 780\ \exp\{-2.5\times10^{-4}\ E\}$ and $\gamma = 2.65$. The spectral distributions of heavier particles are similar when energy is taken per nucleon [14].

Although changes in sources, acceleration, or interstellar propagation of the particles can change their fluxes in the Solar system, the changing solar modulation due to the time variations of solar activity during the solar cycles (11 years, 27 days) is the dominant source of the observed GCR variability. The value of solar modulation parameter Φ changes during these cycles in range $100-1000$ MeV, low values corresponding to low solar activities and high modulations corresponding to high solar activity periods. Looking at the spectra for various values of Φ (Fig. 1.1) it can be seen that the modulation is especially important for energies below a few GeV.

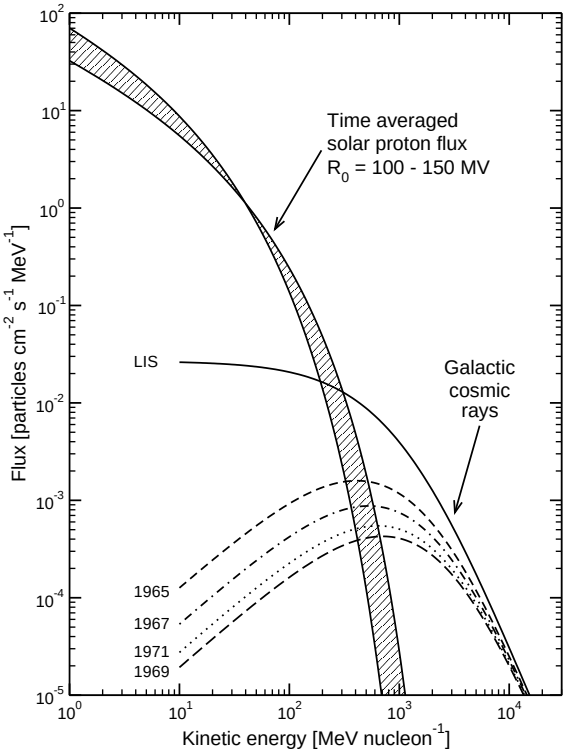

Figure 1.1: GCR proton fluxes near the Earth and in the interstellar space and time averaged SCR proton flux. GCR curves for solar modulation in years 1965, 1967, 1971, and 1969 correspond to the modulation parameter values $\Phi = 470$, 680, 880, and 1000 MeV respectively [13]. LIS holds for Local Interstellar Spectrum.

1.1.2 Solar cosmic rays

Solar cosmic radiation is emitted from the Sun during large flares and at 1 AU it is an important source of nuclei with energies below 300 MeV. The nuclei are almost entirely protons ($\sim 98\%$), with only a few percent of α-particles and a trace of heavier nuclei [17], although the composition of SCR particles varies dramatically with time and energy from flare to flare and even within a flare. Measured values for He/H nuclei ratio are in range 0.001 to 0.04 [17–19] with the mean value ≈ 0.02. Average SCR proton fluxes with energies above 10 MeV reach from 10^5 up to 10^{11} protons cm^{-2} s^{-1} for one flare [13], while the average flux from normally active Sun is ~ 100 protons cm^{-2} s^{-1} (Tab. 1.1). A few large solar flares produce most of SCR particles emitted during 11 year solar cycle and only a small number of particles can be observed during low solar activity periods.

SCR particle flux drops rapidly with increasing energy and for relatively narrow energy intervals roughly behaves as

$$\frac{\mathrm{d}J}{\mathrm{d}E} = \text{const. } E^{-\gamma} \,, \tag{1.3}$$

where γ is typically between 2 and 4 for protons with energies between 20 MeV and 80 MeV with average value 2.9 [20]. Higher γ values and thereby steaper energy spectrum is usually

suitable for higher energies (Fig. 1.1).

For broader energy intervals, a better fit of differential SCR flux is obtained using exponential rigidity shape [21]. The differencial flux per unit rigidity is

$$\frac{\mathrm{d}J}{\mathrm{d}R} = \text{const. } \exp\left\{-\frac{R}{R_0}\right\} \ . \tag{1.4}$$

Rigidity R is the momentum of particle per unit charge, pc/ze, and it is typically given in units of megavolts, MV. To get units in MV from energy in MeV, one uses

$$R^2 = \frac{E^2 + 2EE_0}{z^2} \ , \tag{1.5}$$

where z is charge of particle in units of e and E_0 its rest energy in MeV (for a proton $z = 1$ and $E_0 = 938.256$ MeV). The spectral parameter R_0 for solar protons with energies in range ~ 5 to 200 MeV usually ranges from 20 to 150 MV [e.g 18]. An exponencial in rigidity with $R_0 \approx 100$ MV has been found to be a good fit to the spectra of solar protons averaged over $\sim 10^4$ to 10^7 yr [22].

1.2 Meteorites

A *meteoroid* is a natural object of up to ≈ 100 m in diameter that is orbiting in the space. A *meteor* is the visual phenomenon associated with the passage of a meteoroid through the Earth's atmosphere. A *meteorite* is a recovered fragment of a meteoroid that has survived transit through the Earth's atmosphere. Meteorites are named for the geographic localities in which they fall or are found.

1.2.1 History of meteorites

To make use of a meteorite in studies of the Solar system its origin and history has to be resolved (Fig. 1.2). Meteoroids are created as fragments emitted from parent bodies (mostly asteroids in asteroid belt at $2-4$ AU) in catastrophic collisions with another bodies. During their subsequent flight in space they are continuously exposed to the CR and to the cosmic dust and can also take part in another collisions with smaller bodies.

The interactions with cosmic dust cause only small surface changes, a so called space erosion. A collision with a small body leads to warm up and eventually form and size alteration of the meteoroid. Objects that have undergone such changes have complex exposure histories. A collision with large body stops the meteoroid.

When a meteoroid enters the Earth's atmosphere it has a speed up to 30 km s^{-1}. Atmospheric friction at such high speed causes melting and ablation of outer shells of the meteoroid whereas the inner part still has the low temperature. The great temperature contrast may lead to break-up of the meteoroid into many pieces which then fall to a larger area rather than to one place.

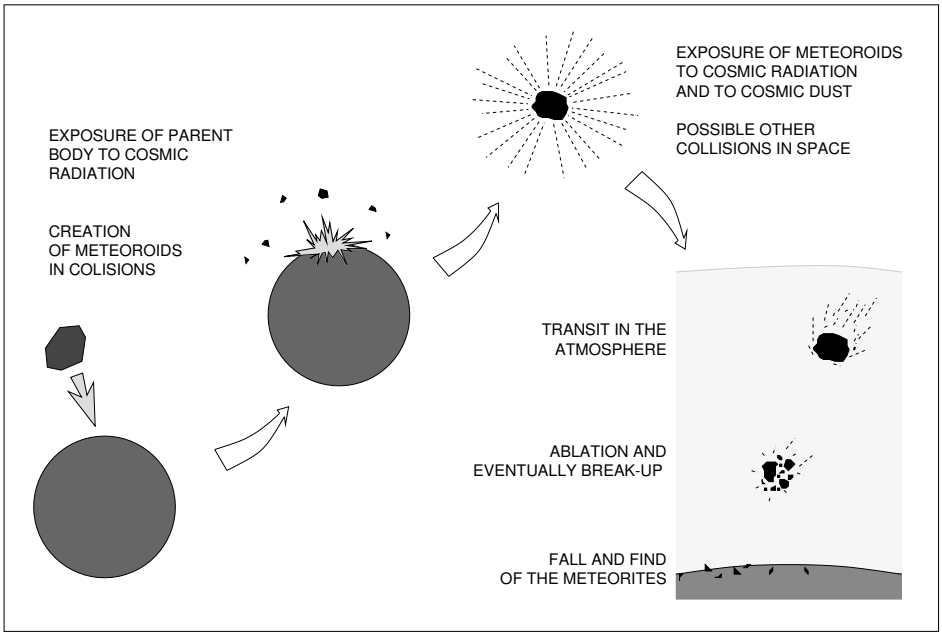

Figure 1.2: Simple illustration of the creation, exposure history and fall of the meteorites on the Earth.

1.2.2 Classification of meteorites

Meteorites are classified in three main groups according to the amount of metal iron they contain to stony, stony-iron and iron meteorites. These three groups are further divided into subgroups according to various mineralogic and petrologic criteria.

The *Stony meteorites* are composed mostly of silicate minerals, although many also contain small metal grains. They are divided into two broad categories: chondrites and achondrites. The chondrites represent the original material of the Solar system and have suffered little if any chemical change since its formation. They contain small up to few milimeter sized grains called chondrules. The ordinary chondrites, representing 90% of all chondrites, are subdivided according to the amount of iron and metal in their composition to H-chondrites (high iron), L-chondrites (low iron) and LL-chondrites (low iron, low metal). Besides ordinary chondrites there are another two chondrite classes: carbonaceous chondrites with higher carbon content and enstatite chondrites with higher enstatite content.

The achondrites are differentiated meteorites that have gone through a radical transformation. They are product of partial melting accompanied by changes in chemical composition followed by crystallization. They are very similar to the basalts of magmatic origin that can be found on the Earth.

The *Iron meteorites* are differenciated metall-rich meteorites consisting almost entirely of nickel-iron metal alloys (90%) with small amounts of other elements like cobalt, sulfur, phosphorus and carbon. They are classified according to their abundance of gallium and germanium.

Table 1.2: Relative abundances of main meteorite types.

Meteorite type	Relative abundance
Stony meteorites – Chondrites	77.1%
Stony meteorites – Achondrites	4.4%
Iron meteorites	16.5%
Stony-iron meteorites	1.7%
Others	0.3%

The *Stony-iron meteorites* have nearly equal proportions of metals and silicates. They are classified according to their abundance ratio Fe/(Fe+Mg).

The relative abundances of main meteorite types are shown in Tab. 1.2. Detailed classification criteria of the meteorites can be found for example in [23].

1.3 Interactions of cosmic ray particles with matter

The energy, charge, and mass of an energetic particle and the mineralogy or chemistry of the target mainly determine which interaction processes are important and which cosmogenic (cosmic-ray-produced) products are formed. Energetic nuclear CR particles mainly interact with matter by ionization, elastic and inelastic scattering on target nuclei and by nuclear reactions.

All charged particles continuously lose energy by exciting or ionizing atoms as they pass through matter. Damage produced by radiation can accumulate in matter and can be detected as termoluminescence. While heavy CR particles are usually stopped by ionisation before any nuclear collision, protons and α-particles can induce nuclear reactions before stopping.

A nuclear reaction between an incident particle and the target nucleus involves the formation of new, secondary particles and of a residual nucleus which is usually different from the initial one. Nuclides whose nuclei arise in these reactions are called *cosmogenic nuclides*.

1.3.1 Solar system matter

All the matter in Solar system, such as cosmic dust, meteoroids, and lunar and planetary surface materials, is continuously irradiated by CR. An energetic particle, when entering the irradiated body, induces nuclear reactions on target nuclei and in this interactions the next generation of particles is produced. Many of these secondary particles (protons, neutrons, $\pi^{\pm 0}$, ...) have enough energy to induce nuclear reactions themselves. Below a depth of ~ 1000 g cm^{-2} there are few cosmic ray particles (mainly muons) because most of them have been removed by nuclear reactions or stopped by ionization energy losses.

Among all particles neutrons play a special role. Because of their lack of electric charge

Table 1.3: Cosmogenic nuclides frequently measured in extraterrestrial matter.

Nuclide	Half-life	Main production mechanisms
^{3}H	12.323 y	spallation on O, Mg, Si
^{3}He	stable	spallation on O, Mg, Si
^{10}Be	1.6×10^{6} y	spallation on O, Mg, Si
^{14}C	5 730 y	spallation on O, Mg, Si
^{21}Ne	stable	spallation on Mg, Al, Si
^{22}Ne	stable	spallation on Mg, Al, Si
^{22}Na	2.602 y	spallation on Mg, Al, Si
^{26}Al	7.4×10^{5} y	spallation on Al, Si
^{36}Cl	3.01×10^{5} y	spallation on Ca, Fe; $^{35}\mathrm{Cl}(n,\gamma)^{36}\mathrm{Cl}$
^{37}Ar	35 d	spallation on Ca, Fe
^{39}Ar	269 r	spallation on K, Ca, Fe
^{40}K	1.28×10^{9} y	spallation on Fe
^{41}Ca	1.03×10^{5} y	spallation on Fe, Ni; $^{40}\mathrm{Ca}(n,\gamma)^{41}\mathrm{Ca}$
^{46}Sc	83.79 d	spallation on Fe, Ti
^{48}V	15.97 d	spallation on Fe, Ti
^{53}Mn	3.74×10^{6} y	spallation on Fe
^{54}Mn	312.3 d	spallation on Fe
^{59}Ni	7.6×10^{4} y	$^{58}\mathrm{Ni}(n,\gamma)^{59}\mathrm{Ni}$
^{60}Co	5.27 y	spallation on Ni; $^{59}\mathrm{Co}(n,\gamma)^{60}\mathrm{Co}$
^{80}Kr	stable	$^{79}\mathrm{Br}(n,\gamma)^{80}\mathrm{Br}(\beta^{-})^{80}\mathrm{Kr}$
^{82}Kr	stable	$^{81}\mathrm{Br}(n,\gamma)^{82}\mathrm{Br}(\beta^{-})^{82}\mathrm{Kr}$
^{129}I	1.57×10^{7} y	$^{129}\mathrm{Te}(n,\gamma)^{129}\mathrm{Te}(\beta^{-})^{129}\mathrm{I}$
^{131}Xe	stable	$^{130}\mathrm{Ba}(n,\gamma)^{131}\mathrm{Ba}(2\beta^{-})^{131}\mathrm{Xe}$
^{150}Sm	stable	$^{149}\mathrm{Sm}(n,\gamma)^{150}\mathrm{Sm}$
^{152}Sm	stable	$^{151}\mathrm{Eu}(n,\gamma)^{152}\mathrm{Eu}(\mathrm{EC})^{152}\mathrm{Sm}$
^{152}Gd	1.08×10^{14} y	$^{151}\mathrm{Eu}(n,\gamma)^{152}\mathrm{Eu}(\beta^{-})^{152}\mathrm{Gd}$
^{156}Gd	stable	$^{155}\mathrm{Gd}(n,\gamma)^{156}\mathrm{Gd}$
^{158}Gd	stable	$^{157}\mathrm{Gd}(n,\gamma)^{158}\mathrm{Gd}$

they don't interact with Coulomb barier of nuclei and therefore can much easier escape from the nucleus or induce nuclear reactions. Due to their high multiplicity neutrons outnumber all other nuclear particles in CR after only a few tens of g cm^{-2} and they become the most important projectyles for CN production.

When matter is exposed to CR, a wide variety of cosmogenic stable and radioactive nuclides is produced. The frequently studied CN are produced from the common elements in extraterrestrial matter (Tab. 1.3). The activity of a cosmogenic nuclide starts near zero for freshly exposed sample and will aproach its production rate (assumed to be constant) after the sample has been exposed to CR for several half-lives.

Two types of nuclear reactions are important for CN production in matter, *spallation reactions* and *neutron capture reactions*. Under spallation reactions all inelastic nuclear reactions with projectyle energies above 1 MeV are considered[1]. In each case the production rate of certain CN depends on the particle energy spectra at the particular depth inside the irradiated object and on the excitation functions (cross section as a function of energy) for

[1]This terminology is used in cosmic ray physics.

Table 1.4: Frequently studied cosmogenic nuclides produced in the Earth's atmosphere [1].

Nuclide	Half-life	Main production mechanisms
^{3}H	12.323 y	spallation on O, N
^{3}He	stable	spallation on O, N
^{7}Be	53.29 d	spallation on O, N
^{10}Be	1.6×10^{6} y	spallation on O, N
^{14}C	5 730 y	$^{14}\mathrm{N}(n,p)^{14}\mathrm{C}$
^{26}Al	7.4×10^{5} y	spallation on Ar
^{36}Cl	3.01×10^{5} y	spallation on Ar; $^{36}\mathrm{Ar}(n,p)^{36}\mathrm{Cl}$

all reactions contributing to the production of the nuclide.

1.3.2 Terrestrial matter

There are two important facts affecting the interactions of CR on Earth, the presence of the geomagnetic field and the presence of the atmosphere[2].

The *Earth's magnetic field* has nearly a dipole character with axis close to the rotation axis of Earth (the geomagnetic field axis is wandering with time). Its presence causes the deflection of particles heading Earth, whose rigidity is less than cutoff rigidity for the angle of flight of the particle at the particular coordinates. This means that the energy spectrum of primary cosmic ray particles interacting with Earth at any particular geomagnetic latitude will lack particles with energies below cutoff corresponding to that latitude. Vertical cutoff rigidities range from 0 GV on the poles to 14.5 GV on the equator [24], which according to (1.5) corresponds to minimal energy of protons 0 GeV and 13.6 GeV respectively.

The *Earth's atmosphere* makes a barrier for CR to interact directly with the surface. It consists of 75% nitrogen, 23% oxygen and 2% other gases[3]. The air density is highest on the sea level and decreases with increasing altitude to practicaly zero at ≈ 100 km. Its great thickness (≈ 1033 g cm^{-2}) causes most of the total energy of primary CR to be absorbed there so that only $\sim 3\%$ of it is left on the sea level (mostly muons and neutrons).

Energetic distribution of SCR particles (Tab. 1.1) and the presence of geomagnetic field cause that SCR particles induce nuclear reactions only in the upper layers of the atmosphere in the polar regions and mainly during large solar flares. Therefore, their contribution to the interactions leading to nuclear transformations can be neglected.

Because the Earth's atmosphere contains mainly light nuclei, there are practically only light fragments produced in it. Frequently studied cosmogenic isotopes produced in the atmosphere are listed in Tab. 1.4. The CN measured and studied in the extraterrestrial matter (Tab. 1.3) are also measured and studied in surface rocks. But more sensitive methods

[2]In fact, there are more objects in the Solar system with its own magnetic field and/or atmosphere, but as there have been only meteorites and lunar samples studied up to now, which both have neither the magnetic field nor the atmosphere, we do not consider their presence for extraterrestrial matter.

[3]Values are in weight percent.

are needed to measure much smaller terrestrial concentrations of cosmogenic isotopes.

1.3.3 Transport and archives of cosmogenic nuclides on the Earth

When comparing to radiation effects on the extraterrestrial samples, the effects on terrestrial materials are small, yet not completely suppressed. Earth's outer shells are in continuous movement and their atoms take part in various geochemical, geophysical and biological cycles running between atmosphere, biosphere, hydrosphere and litosphere. During these processes the irradiated matter is dispersed and mixed with an unirradiated causing decrease of the CN concentrations and reducing the observability of the effects. Only two types of the final products of the CR interactions remain measurable:

- *radioactive nuclei*, which remain recognizable for certain period of time and
- *atoms of noble gases*, which cannot bind themselves to dust particles or to compounds and so do not take part in mixing processes; most of their amount on the Earth can be found in the atmosphere.

Cosmogenic radionuclides (CRN) production in the atmosphere depends besides the geomagnetic latitude also on altitude. Production rates are highest at high altitudes and decrease exponentially to the sea level. Because of differences in atmospheric processes in troposphere and stratosphere the altitude plays an important role in the transport of CN in the atmosphere. Many CRN bind themselves to aerosols (e.g. ^{7}Be, ^{10}Be, ^{26}Al). These are removed from troposphere within a few weeks by rainfalls. The residence of the aerosols in the stratosphere is much longer, up to a few years. Because of the stratospheric mixing the CRN produced in different geomagnetic latitudes are mixed. As the majority of the production takes place in the stratosphere, the CRN concentration after the fall is practicaly the same for all latitudes.

From the transport point of view, ^{14}C has a special position among all cosmogenic isotopes. In the atmosphere it can be found mainly in form of $^{14}CO_2$ and its abundance depends to a large extent on biological processes, in which it is exchanged between individual parts of the geosphere and distributed to all living organisms. This fact has designated the ^{14}C for use for the determination of the age of the biological material. Its main reservoir on Earth is the ocean.

The main archives of other cosmogenic isotopes produced in the atmosphere are ice cores in polar regions, deep sea sediments and loesses. Even though the concentrations of isotopes in the archives are very small, sensible detection methods and technologies, like accelerator mass spectrometry (AMS), make it possible to measure such small values. The analysis of the results then enables us to study the time variations of factors directly or indirectly influencing production, transport and deposition of CN in the past. That is for example to study the time variations of Solar activity, geomagnetic field intensity and climate evolution in a time scale

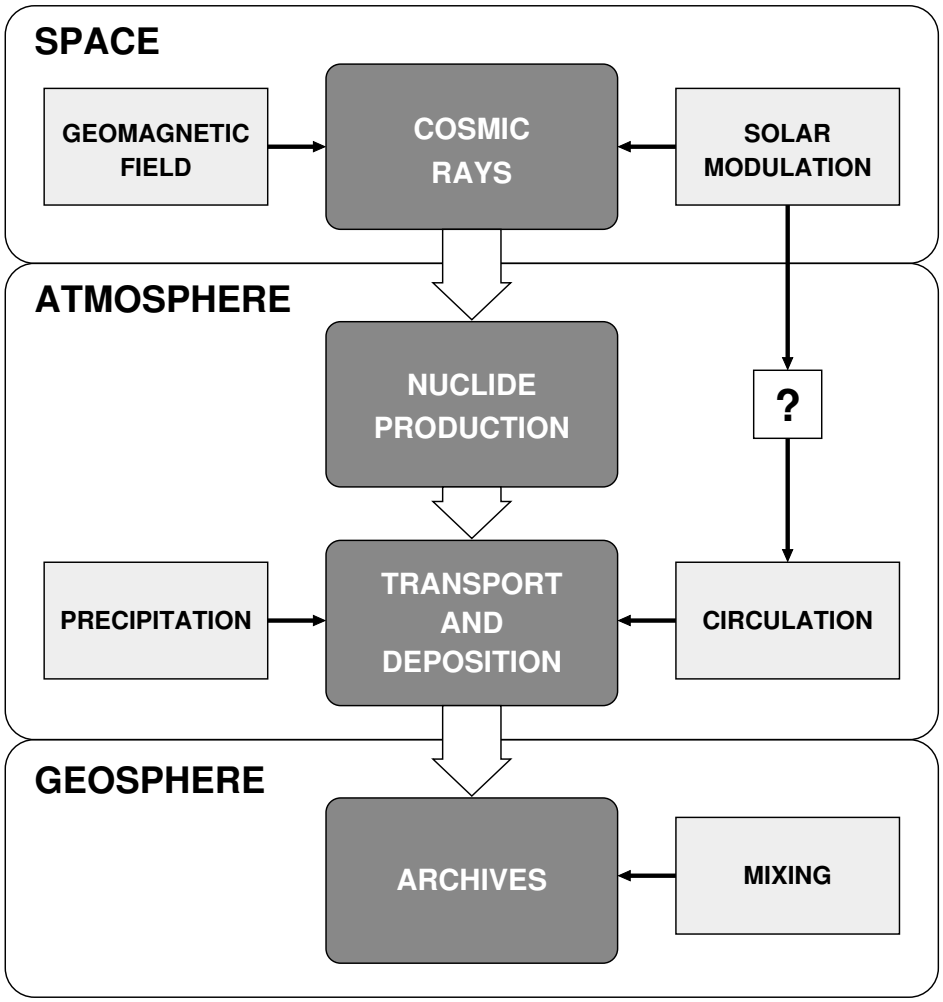

Figure 1.3: Simple description of processes directly or indirectly affecting production, transport and deposition of cosmogenic nuclides in the Earth's atmosphere. The question mark indicates the unclear influence of Sun on the atmospheric processes.

$\sim 10^3 - 10^7$ years [e.g. 25–27]. Simple description of main processes influencing production, transport and deposition of CN produced in the atmosphere is shown in Fig. 1.3.

Another contribution to the CN concentrations on Earth is the interplanetary matter, which has been irradiated before entering the Earth's atmosphere. Influx of meteoroids, interplanetary dust and other interplanetary bodies, that also include the CR itself, to the Earth reaches the total amount of $\sim 10^8$ kg per year [28].

1.4 Production rate of cosmogenic nuclides

Experimentally measured depth dependent concentrations of a radioactive and stable CN are usually given in form of production rate. This represents a number of nuclei produced per unit of time and unit of mass. The corresponding unit is $g^{-1}\,s^{-1}$.

Various units are used for production rate. In terrestrial surface rocks it is $g^{-1}\ yr^{-1}$, in

meteorites it is dpm/kg (disintegrations per minute and kilogram). Production rate of stable rare gases is given in units $\mathrm{cm^3\ STP\ g^{-1}\ Ma^{-1}}$, meaning the amount of gas in $\mathrm{cm^3}$ in standard properties per gram and million years. The relations between individual units and $\mathrm{g^{-1}\ s^{-1}}$ are

$$\begin{aligned} 1\ \mathrm{g^{-1}\,s^{-1}} &= 3.1536 \times 10^7\ \mathrm{g^{-1}\,yr^{-1}} \\ &= 60000\ \mathrm{dpm/kg} \\ &= 1.1738\ \ 10^{-6}\,\mathrm{cm^3\,STP\ g^{-1}\,Ma^{-1}} \end{aligned}$$

For the atmosphere the depth dependent production rates are integrated over the thickness of the atmosphere and total (integral) production rates are obtained in units $\mathrm{cm^{-2}\ s^{-1}}$.

The production rate P_j of cosmogenic nuclide j at depth d inside an irradiated object with radius R in one gram of target material is calculated as

$$P_j(d,R) = \sum_i N_i \sum_k \int_0^\infty \sigma_{ijk}(E_k)\ J_k(E_k,d,R)\ \mathrm{d}E_k\ , \tag{1.6}$$

where N_i is a number of atoms of target element i per gram of target material, σ_{ijk} is a cross section for the production of nuclide j from target element i by particles of type k with energy E_k and J_k is a differential flux density of particles of type k at depth d inside the irradiated object with radius R.

From (1.6) it is now evident what information is needed for a complete description of production rate depth profiles of cosmogenic nuclides in considered irradiated objects. This is the bulk chemical composition of the object, the geometry dependent differential flux densities of particles, and the excitation functions for all considered reactions.

While the chemical composition can be measured directly, there is no possibility to measure the depth dependent particle flux densities. These can be calculated modelling the real irradiation properties of the object. The most problematic part are the nuclear cross sections.

1.5 Calculation of particle transport in matter

Transport of particles in matter and cascade evolution is described by Boltzmann equation. It cannot be solved analytically without applying some approximations [29] leading to *parametric* solutions [e.g. 4, 30] for which still parameters have to be determined experimentally.

Advance in computer technologies in recent years has made it possible to run high CPU load calculations needed for physically complete *stochastic* solution of Boltzmann equation. Such calculations are based on Monte Carlo simulation of particle production and transport. In Monte Carlo simulation particle passage through matter is tracked using only basic physical rules and quantities. So if energy spectrum of primary radiation is known together with cross sections needed and elemental composition of target material, following the transport of large number of primary particles randomly chosen from primary spectrum leads to calculation of desired parameters (e.g. particle production or fluxes, energy deposition).

Considering only a hadron cascade, particle interactions with matter are calculated using basic models of nuclear reactions depending on energy of particle. At high energies particle enters the nucleus and interacts with its constituents separately inducing production of new particles which further interact with particles within nucleus building up the *intranuclear cascade*. Some of these energetic particles escape from the nucleus and interact with other nuclei so developing the *internuclear cascade*.

Intranuclear cascade leaves nucleus in highly excited state which can lead to further emission of particles or fragments from the nucleus (*preequilibrium decay*). Energy that is not emitted from nucleus in this phase is redistributed among nucleons and nucleus is getting into equilibrium state. Subsequent deexcitation of nucleus, so called *evaporation process*, is described by the compound nucleus decay model.

Various realizations of these models can be found in several Monte Carlo codes. The most often used are the LAHET Code System [31], HERMES [32] and GEANT [33, 34].

1.6 Cross sections

The probability of a particular interaction of a particle with another particle or with a nucleus is expressed as cross section of the interaction. Its dependence on initial particle energy is usually referred to as excitation function. For a complete description of the production rate of a particular cosmogenic nuclide in the material of an irradiated object the excitation functions for all reactions leading to its production have to be known. However, these are not always available.

1.6.1 Proton induced reactions

Cross sections for the production of residual nuclei in proton induced nuclear reactions used for calculations of CR interactions with matter are fairly well known as they have been extensively measured [e.g. 35–39]. Published experimental cross section data are included into nuclear reaction data library EXFOR [40].

All reactions of interest for proton induced cosmogenic nuclides production are spallation reactions with threshold energies in range $10 - 100$ MeV. Measurements of cross sections for these reactions are performed at accelerators where targets of pure material are irradiated with monoenergetic proton beam at different energies. Targets have usually form of a thin foil (therefore the name thin target experiments) so that energy loss of protons while passing the target can be neglected. When thick targes are used, corrections for cascade evolution and production by secondary particles have to be considered. After the irradiation, the concentrations of residual nuclei are measured (by gamma spectrometry, AMS and conventional rare gas mass spectrometry) and subsequently cross sections for their production at the particular energy are determined.

If no experimental data for certain reaction exist one has to rely on calculated excitation function. There are several computer codes that can be used for such calculation (LAHET [31], HETC/KFA2 [32], ALICE-IPPE [41, 42], and other). These codes apply various theoretical models of nuclear reactions for different energy ranges. Intercomparison between these codes and available experimental data [11] demonstrated that intermediate energy (up to 5 GeV) activation yields can be predicted at best with uncertainities of about a factor of two. Frequently, average deviations are much larger and individual reaction-wise deviations may go up to three orders of magnitude.

Therefore, theoretical proton excitation functions are mainly used for filling the gaps in experimental data or for interpolation purposes. In such cases the calculated excitation functions are adjusted to fit the experimental cross sections.

1.6.2 Neutron induced reactions

Cross sections for neutron induced production of residual nuclides can be divided according to energy to low energy neutron cross sections (up to $\approx$ 15 MeV) and middle and higher energy neutron cross sections.

For low energies, there are experimental data for many reactions (see EXFOR data library [40]) because monoenergetic neutron sources for this energy region exist. Measured data sets originating from numerous nuclear fusion and nuclear fission experiments have been expanded to continuous energy regions by evaluations and are stored in evaluated neutron data libraries (ENDF [43], JEF [44], JENDL [45]).

For energies above 20 MeV no experimental cross section data exist for most of reactions. This is due to principal complications connected with middle- and high-energy monoenergetic neutron sources construction and design. Because of its zero electric charge neutron cannot be directly accelerated to a particular energy and its trajectories are not bent by magnetic field. For measurements in this energy region, quasi-monoenergetic neutron sources are used, which are usually based on (p, n) reactions, for example $^{7}\mathrm{Li}(p, n)^{7}\mathrm{Be}$. Spectrum of neutrons produced in these reactions contains besides peak right below primary proton energy also a broad continuum region starting below peak and reaching to low energies. This continuum originates mainly from concurent reaction modes (e.g. three body break-up). When targets are irradiated with such neutron beams, an evaluation method has to be used to get desired cross section value at particular energy [e.g 46, 47].

For neutron cross section calculations usually the same computer codes can be used as for protons. For middle- and high-energy region calculated excitation functions cannot be compared with experimental data but the discrepancies are probably similar to those for protons or higher [see e.g. 46].

For cosmochemical applications neutron spallation cross sections are often set equal to that for corresponding proton reactions, i.e. for example cross sections for a (p, pn) reaction

are used for a $(n, 2n)$ reaction. This is reasonable for high energy region where differences in proton and neutron interactions disappear. For middle energies this assumption no longer holds as can be seen from comparison of calculated and measured production rates in extraterrestrial matter [46] and also from comparison with the few existing experimental cross sections [48, 49].

Setting neutron cross sections to that for protons can still be useful when no experimental data exist and theoretical excitation functions are rather unrealistic. Some authors [e.g. 3, 50, 51] modified such neutron cross sections to get better agreement with experimental production rate data.

1.6.3 The mean GCR particle flux

The mean (or effective) primary GCR particle flux represents average GCR particle flux over the last few million years. Its value is determined by comparing the calculated production rates for some long lived nuclides (^{10}Be, ^{26}Al, ^{36}Cl, ^{53}Mn) normalized to the total primary GCR proton flux 1 cm^{-2} s-1 with its measured concentrations in an extraterrestrial object (meteorite or lunar samples). By adjusting the former to the later one obtains the desired mean total flux and subsequently the mean solar modulation.

As the calculated production rates depend strongly on cross sections used, the determined value of total GCR flux will also be cross sections dependent.

Because of the lack of measured neutron cross sections several scientific groups have evaluated more or less consistent sets of neutron excitation functions. The groups of Robert C. Reedy (Los Alamos, USA) and Rolf Michel (Hannover, Germany) have both applied their cross sections to the CN production rate calculations to obtain the mean GCR particle flux value and subsequently the time averaged value of solar modulation parameter.

Cross sections for proton reactions by Reedy et al. are based on existing experimental data. For neutron reactions the few existing measured data are included but usually these are based on measured cross sections for corresponding proton reaction and are eventually modified to get better agreement with experimental production rate data. Description and references to the cross sections for the particular reactions can be found for example in [7].

Using these cross sections the calculated production rates were adjusted to the measured CN concentrations in meteorite Knyahinya and Apollo 15 lunar samples and for the total GCR particle flux the values 4.8 cm^{-2} s^{-1} [52] and 4.56 cm^{-2} s^{-1} [53] were obtained for meteoroid and Earth's orbits respectively.

Proton cross sections of Michel et al. were measured for many target-product combinations in several thin- and thick- target experiments [e.g 35, 36]. Their neutron cross sections evaluation is based on a least-squares adjustment to get better agreement with experimental production rate data[4] [e.g. 46]. The evaluation includes many thick target neutron irradiation

[4] See chapter 5.

experiments with well-described primary neutron flux.

Using these cross sections the total GCR proton flux values obtained for meteoroid and Earth's orbits were 4.06 $cm^{-2}\,s^{-1}$ [8] and 4.54 $cm^{-2}\,s^{-1}$ [54] respectively.

2 Statement of the problem

This work is primarily intended to help us understand the neutron interactions with matter with emphasize given to cross sections for neutron induced nuclear reactions. We atempt to study three main topics.

Studying the interactions of low-energy neutrons in ordinary chondrites, the Moon, and extraterrestrial objects in general we attempt to investigate

- The dependence of the differential neutron fluxes on the size of the meteoroide and on the depth below the surface.
- The effects of bulk chemical composition on neutron fluxes inside meteoroids of various sizes.
- The production dependence of ^{36}Cl, ^{41}Ca, ^{60}Co, ^{59}Ni, and ^{129}I on depth inside meteoroids of various sizes.
- The effects of bulk chemical composition on (n, γ) production of ^{36}Cl, ^{41}Ca, ^{60}Co, ^{59}Ni, and ^{129}I in ordinary chondrites.
- Intercomparison of production rates calculated using excitation functions for (n, γ) reactions from different neutron evaluated data files.
- Determination of the mean GCR particle flux at Earth's and meteoroid orbits.
- Comparison of calculated production rates to the available experimental data.

Studying the influence of cross sections for spallation production of residual nuclides induced by protons and neutrons we atempt to investigate the differences arising when using the cross sections from the group of Reedy and those from the group of Michel. The comparison is done for

- The ^{7}Be and ^{10}Be production rate in the Earth's atmosphere.
- The ^{10}Be, ^{14}C, ^{21}Ne, ^{26}Al, and ^{36}Cl production rate in terrestrial surface rocks.

Neutron irradiation experiments performed within the HINDAS project need the calculation of neutron transport inside the target for the proper interpretation of the production rate results. The procedure of unfolding of excitation functions for particular *target–product* combination requires a well described neutron fields inside each individual target. Here we attempt to

- Test the semi-empirical model to calculate the quasi-monoenergetic neutron spectra.
- Test the feasibility of the Monte Carlo code system LCS to the calculation of the quasi-monoenergetic neutron spectra.
- Calculate the quasi-monoenergetic neutron spectrum in the beam for all irradiations for which the measured spectrum is not available.
- Perform the neutron transport calculation inside the targets for 22 considered irradiation experiments.
- Analyze the development of neutron field inside the target.
- Determine the accuracy of the transport calculation by comparison of calculated and measured neutron spectra after passing through the target.

3 Neutron capture production of cosmogenic nuclides in chondrites

In interactions of GCR particles with meteoroids many secondary particles are produced. However, high thermal neutron fluxes can only be reached inside large meteoroids. Depending on the concentrations of target elements, production rates of neutron capture produced isotopes like ^{36}Cl and ^{60}Co can only be measured in chondrites with pre-atmospheric radius greater than $\approx$ 30 cm. For such specimen only little data exist. The situation is better for the Moon, where the n-capture data of ^{41}Ca, ^{60}Co and the fission data of ^{235}U measured in various lunar samples are available [9, 55, 56].

Recently, systematic Monte Carlo calculations of the spallogenic production of cosmogenic nuclides have been presented for the meteoroids of various sizes and a 2π geometry [7, 46, 52–54]. For thermal neutron capture production of CN no such systematics is available. Thermal neutron fluxes and neutron capture effects have previously been studied in stony meteorites and in the lunar surface using semi-empirical [5, 57, 58] and Monte Carlo models [59].

Presented here is a purely physical model for neutron capture production of cosmogenic nuclides induced by GCR particle interactions in meteoroids which uses only one free parameter – the mean GCR particle flux in the meteoroid orbits. The model is based on Monte Carlo simulation of neutron production and transport inside meteoroids and evaluated excitation functions for individual (n,γ) reactions. We focus here on the n-capture production of cosmogenic radionuclides ^{36}Cl, ^{41}Ca, ^{60}Co, ^{59}Ni, and ^{129}I (Tab. 1.3) in stony meteoroids with radii from 10 cm to a 2π irradiation.

3.1 Calculational model

In the case of neutron capture production there is only one reaction to consider for each produced nuclide and the formula (1.6) reduces to

$$P(d,R) = N \int_0^\infty \sigma(E_n)\; J_n(E_n,d,R)\; \mathrm{d}E_n \;, \tag{3.1}$$

where J_n is the differential flux density of neutrons with energy E_n at depth d inside a meteoroid with radius R and σ is the excitation function for the particular (n,γ) reaction.

In this work transport of primary cosmic ray particles and nuclear cascade evolution in matter, as well as transport of secondary particles in matter, are calculated using the LAHET Code System [31].

3.1.1 The LAHET Code System

The LAHET Code System (LCS) [31] developed at Los Alamos National Laboratory is a system of general-purpose Monte Carlo codes that treat the relevant physical processes of particle production and transport. Fig. 3.1 shows schematic description of the linkage of the included codes and the data flow between them. Coupling between the codes is realized by data files in which local results from one code are stored to be subsequently treated further by another code. The combination of particular codes allows one to treat most common problems of particle interactions.

Whereas the actual particle transport is calculated by the LAHET and HMCNP codes, the PHT and MRGNTP codes are used for data file conversion and merging for consequent HMCNP calculations. The HTAPE code extracts requested information from data files and outputs it in readable form.

The LAHET (Los Alamos High Energy Transport) code treats all interactions by protons, pions, muons and light nuclei (^{2}H, ^{3}H, ^{3}He, α) completely and interactions of neutrons only above a cutoff energy, typically 20 MeV. Any neutron appearing from a reaction with energy below the cutoff energy has its kinematic parameters recorded onto a neutron file (NEUTP) for subsequent transport by HMCNP code.

LAHET transports particles using intranuclear cascade, Fermi break-up and evaporation models. Optionally the preequilibrium model can be used as an intermediate stage between the intranuclear cascade and the evaporation phase of a nuclear reaction.

The MCNP (Monte Carlo N-Particle) code [60] is an independent Monte Carlo based code that can be used for neutron, photon, electron or coupled neutron/photon/electron transport. Its version in LCS (HMCNP) has been modified to accept NEUTP file with low energy neutron or/and gamma histories as an input source to complete the particle transport down to thermal energies. While LAHET models nuclear interactions using parameters designed for all nuclei (global parameters), MCNP uses an evaluated ENDF/B-based cross section libraries for each neutron reactions [43]. This allows neutron production rates of certain nuclides to be calculated directly with MCNP, especialy for neutron capture reactions because thy are dominated by low energy neutrons.

LCS uses random numbers and basic nuclear data to model the interactions of particles with matter. The energy and direction of the incident particle that starts each cascade are selected from a specified source distribution using random number generator. The location where this incident particle interacts with a nucleus is then randomly selected considering both ionization energy losses along its path and the nature of reactions it can make with

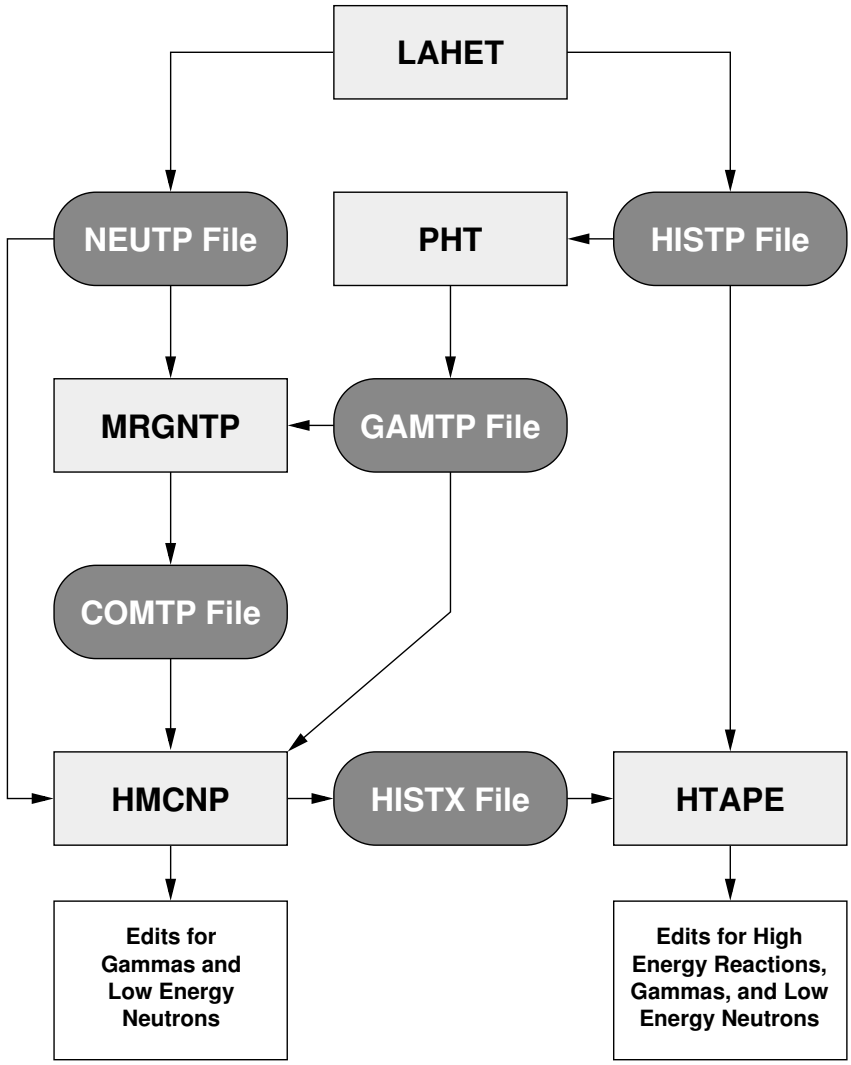

Figure 3.1: Schematic description of linkage of the codes included in the LCS and the data flow between them [31].

various target nuclei. The intranuclear cascade induced by the particle within the nucleus is then simulated. Further the preequilibrium calculation is used to de-excite the nucleus which is subsequently completely cooled using the evaporation model. Then the emitted secondary particles are followed. The particles in the internuclear cascade are recorded to get their fluxes in the specified region of the target. A sufficient number of incident particles is needed to get good statistics for the calculated particle fluxes.

To get particle fluxes for production rate calculations using (1.6) from the LCS calculation, input files have to be provided containing parameters specifying physical models to be used for transport, the description of the composition and geometry of the irradiated object, and the definition of the source of the radiation. Besides the composition of the object, the description of its geometry has to reflect also the desired positional resolution of the output information. As an example, the LAHET, HMCNP and HTAPE input files are shown in appendix A.

Table 3.1: Bulk chemical composition (in weight percent) of meteorite classes used in calculations and their bulk densities (in g cm^{-3}) [61, 62].

Element	H-chondrite	L-chondrite	LL-chondrite	CI-chondrite	Lunar regolith
H	–	–	–	2.0	–
C	0.11	0.09	0.12	3.2	–
O	35.7	37.7	40.0	46.0	41.1
Na	0.64	0.7	0.7	0.49	0.228
Mg	14.0	14.9	15.3	9.7	6.84
Al	1.13	1.22	1.19	0.86	6.91
Si	16.9	18.5	18.9	10.5	21.9
P	0.108	0.095	0.085	0.102	–
S	2.0	2.2	2.3	5.9	–
K	0.078	0.0825	0.079	0.058	0.229
Ca	1.25	1.31	1.3	0.92	7.25
Ti	0.06	0.063	0.062	0.042	–
Cr	0.366	0.388	0.374	0.265	–
Mn	0.232	0.257	0.262	0.19	–
Fe	27.5	21.5	18.5	18.2	12.3
Co	0.081	0.059	0.049	0.0508	–
Ni	1.6	1.2	1.02	1.07	–
Sm	–	–	–	–	0.0014
Gd	–	–	–	–	0.0019
Density	3.7	3.5	3.5	2.25	1.7

3.1.2 Neutron spectra

In this work an irradiated meteoroid is modelled as sphere of uniform bulk chemical composition corresponding to its class. Bulk chemical compositions and bulk densities of investigated meteorite classes used in calculations are listed in Tab. 3.1.

To study the shielding effects we model meteoroids of various sizes. To achieve the depth resolution of particle spectra and subsequently the depth dependence of nuclide production rates the sphere is divided to concentric subshells. The smaller the thickness of the shell, the more detailed investigation of the depth dependence is possible (depth resolution of production rates). On the other side, in shells with smaller volume less particle interactions occure, which consequently leads to higher statistical errors. Therefore, the thickness of the shells chosen for particular meteoroid size is always a compromise between these two factors.

Our calculations were made for meteoroid radii 10, 20, 25, 30, 35, 40, 50, 65, 85, 100, 120, 150, 200, 300 and 500 cm plus a 2π so the whole range of meteoroid sizes was covered. We used 1 cm thick shells for radii below 100 cm, 2 cm for radii 100–200 cm and 4 cm for radii above 200 cm.

Starting from the parameterization of the primary GCR proton spectrum given by the equation (1.2) for solar modulation parameter $\Phi = 650$ MeV we calculated neutron spectra in each shell for each meteoroid size. For radius 500 cm and the 2π irradiation geometry we calculated only the spectra down to a depth of 300 cm. The number of simulated cascades

was chosen to result in statistical uncertainties of particle fluxes of $\sim 5\%$ at small depths increasing to $\sim 10\%$ near the center of the meteoroid.

For GCR particle calculations our model explicitly takes into account only proton- and neutron-induced reactions. α-particles are considered only by an approximation, because cross sections needed for an accurate modeling are not available. Interactions of heavier nuclei are neglected.

We assume that an incoming ^{4}He nucleus breaks into four nucleons in its first inelastic collision, each having 25% of its energy. Because the primary α-particle spectrum is roughly identical to that of protons when energy is taken per nucleon [14], the four nucleons have approximately the same energy distribution as the GCR protons. Neglecting further the differences in multiplicities and the spectral distributions of emitted particles between protons and neutrons, α-particles can simply be included into calculations by applying an appropriate scaling factor.

If we come out from GCR particle abundances as given in section 1.1.1 we can calculate this factor by dividing number of all nucleons in proton and α parts of primary GCR flux by number of protons

$$\frac{N_p + 4N_\alpha}{N_p} \doteq 1.55 \; . \tag{3.2}$$

This approximation neglects the fact that the stopping power of α-particles is $\approx 4\times$ higher than that of protons, even for particles with the same energy per nucleon. In comparison to protons this leads to higher attenuation of ^{4}He nuclei and different shapes of the spectra inside the irradiated object. For all products discussed in this work, these facts have only a minor influence on the production rates.

3.1.3 Cross sections

There are several data banks containing evaluated excitation functions for many reaction types. Most commonly used are ENDF/B (Evaluated Nuclear Data File Version B - Brookhaven) [43], JEF (Joint Evaluated File) [44] and JENDL (Japanese Evaluated Nuclear Data Library) [45]. These cover energies from 10^{-5} eV to ≈ 20 MeV. For the evaluation, different procedures were used in each of these libraries. Therefore, there are differences in the data between the libraries in many cases.

The excitation functions for the (n, γ) reaction on the majority of stable isotopes are available within the evaluated nuclear files. For the calculation of the n-capture production of cosmogenic nuclides in terrestrial and extraterrestrial matter usually the ENDF/B-VI is used [e.g. 6, 7, 9, 59]. One of the reasons for that is that this library is coupled to the MCNP code which allows for direct nuclide production rate values on output of the transport calculation. Recently also the JEF-2.2 data were used for the n-capture production rate calculations on some isotopes [63].

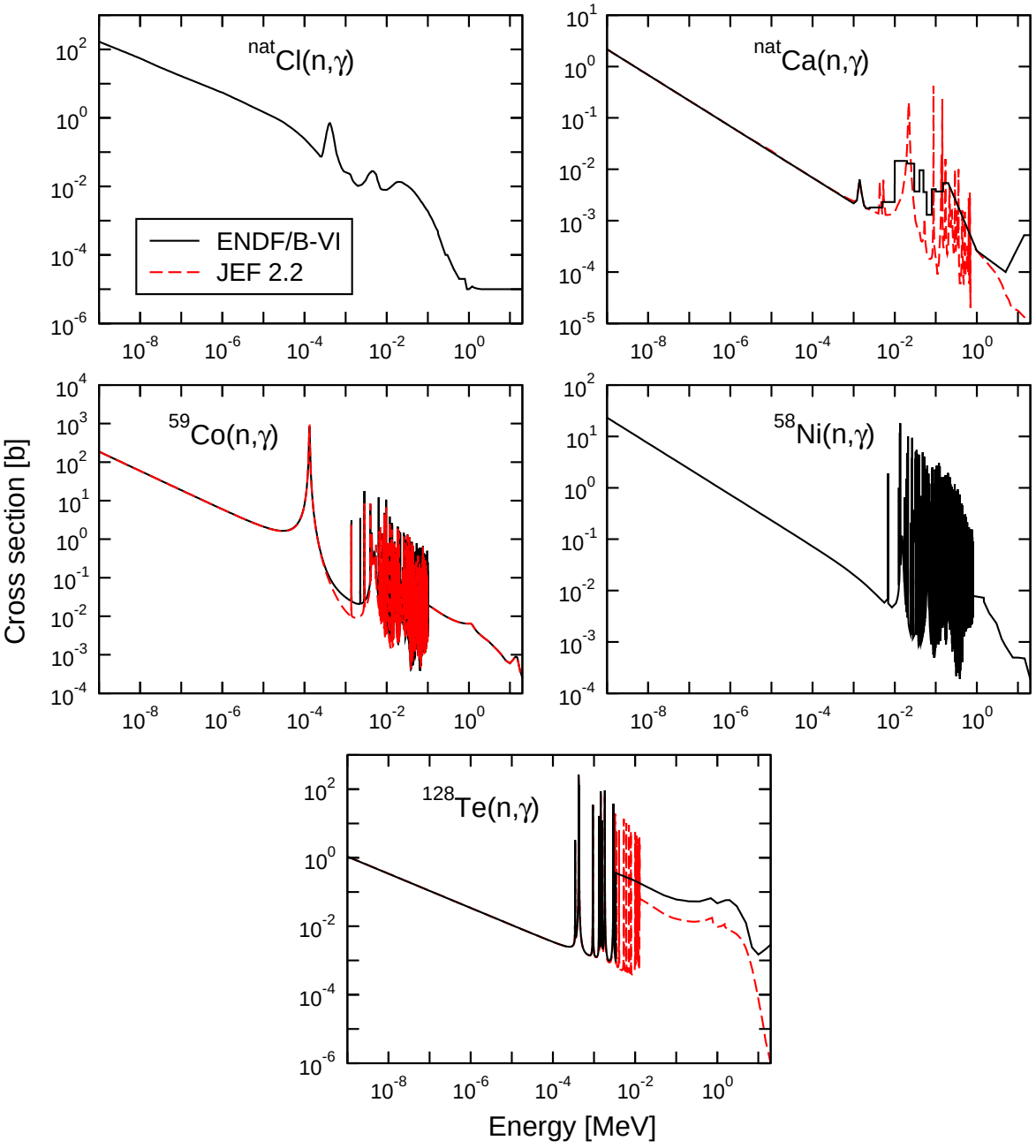

Figure 3.2: Excitation functions for neutron capture reaction on isotopes ^{nat}Cl, ^{nat}Ca, ^{59}Co, ^{58}Ni, and ^{128}Te from neutron data files ENDF/B-VI [43] and JEF-2.2 [44]. For ^{nat}Cl and ^{58}Ni these are identical in both libraries.

The excitation functions of (n, γ) reaction for the production of nuclides considered in this work from ENDF/B-VI and JEF-2.2 files are shown in Fig. 3.2. As there are no excitation functions for neutron capture on ^{35}Cl and ^{40}Ca in any of these two files, the excitation functions for the capture on natural isotopic composition of these elements were used.

For ^{nat}Cl and ^{58}Ni the excitation functions are identical in both libraries. For ^{nat}Ca the resonance region is recognized better in the JEF-2.2 excitation function. Due to the steep

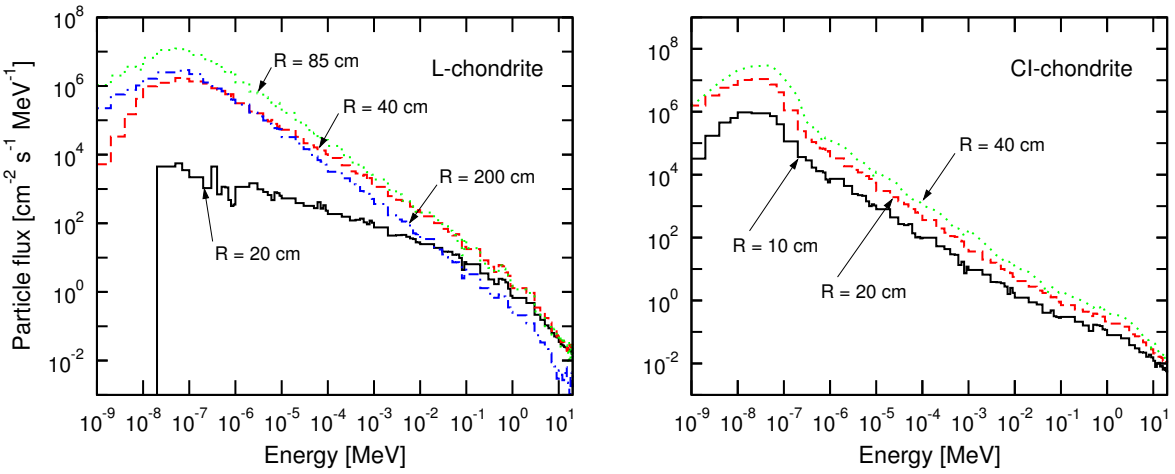

Figure 3.3: Differential neutron spectra in the center of a spherical L-chondrite with radius 20, 40 85, and 200 cm and CI-chondrite with radius 10, 20, and 40 cm. Data are normalized to a total incident flux of primary protons $J_0(E > 10 \text{ MeV}) = 1 \text{ cm}^{-2} \text{ s}^{-1}$.

shape, the differences above ≈ 1 MeV do not play an important role for the ^{41}Ca production in meteoroids. Resonances are different also for ^{60}Co but the differences are small. For ^{128}Te there is a wider resonance region recognized in JEF-2.2 excitation function and there is also a considerable difference in the cross section values right above the resonance region.

3.2 Results and discussion

3.2.1 Neutron spectra

According to Masarik and Reedy [7], the differences in spectra above 1 MeV, which are due to different compositions corresponding to the different chondrite classes, are marginal. As it can be seen from the shape of the excitation functions (Fig. 3.2), the primary role in the n-capture production of the cosmogenic nuclides plays the low energy part of the neutron spectra. Therefore, we have investigated in detail the energy dependence of neutron fluxes below 20 MeV.

The neutron spectra calculated in the center of L-chondrite with radius 20, 40, 85, and 200 cm and in the center of CI-chondrite with radius 10, 20, and 40 cm are shown in Fig. 3.3. In the center of L-chondrite with radius 20 cm the neutron fluxes are quite small in comparison to that for larger radii and there are no neutrons with energies below $\approx 10^{-8}$ MeV. In this case, the differential neutron fluxes decrease monotonously with increasing energy. In the other three spectra in L-chondrites the Maxwellian maximum can be seen at energy around 8×10^{-8} MeV. Above this energy there is an approximately exponential decrease in differential neutron flux with energy.

The thermal energy part of the neutron field increases up to radius of about 85 cm and then differential fluxes start to lower at all energies due to a significant attenuation of primary

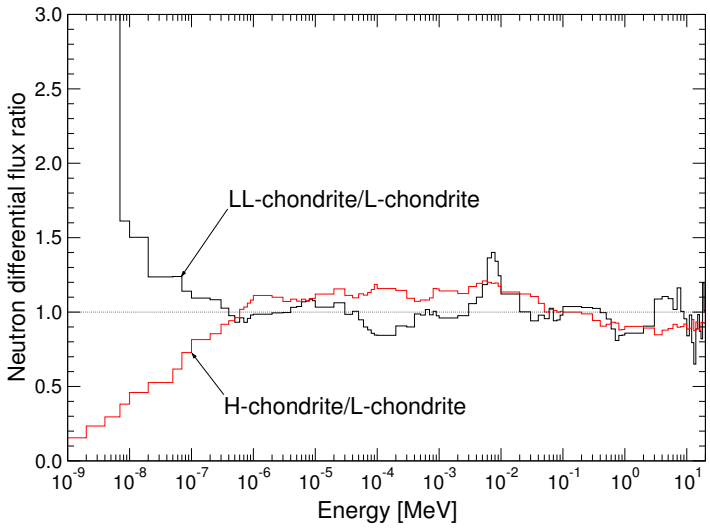

Figure 3.4: Neutron differential fluxes as a function of energy in the center of a sphere with radius 85 cm with a bulk chemical composition of H-chondrites and LL-chondrites relative to that in L-chondrites.

particles. The differences in the spectra for radii below 85 cm are minimal at energies above 1 MeV.

The differential neutron fluxes for LL- and H-chondrite classes are very similar to those for L-chondrite. The different bulk chemical composition of the chondrite classes, that has minimal effect on spectra for energies above 1 MeV, become significant for thermal energies. The main differences can be seen at energies below 0.5 eV (Fig. 3.4). The neutron fluxes at these energies are much lower in the case of H-chondrites than for L-chondrites. This is due to lower oxygen content (2% less) and higher iron content (6% more) in H-chondrites than in L-chondrites. Oxygen is one of the lightest elements in the chemical composition of ordinary chondrites and the differences of order of a few per cent in the abundance can change the neutron moderation and so the neutron fluxes at thermal energies. In addition, the relatively high thermal neutron absorption cross section of iron causes even lower thermal neutron fluxes. For LL-chondrites the higher oxygen content (2.3% more) and lower iron content (3% less) results in significantly higher fluxes below 0.5 eV than for L-chondrites.

The situation is different in CI-chondrites. Hydrogen, as the lightest element, is the best neutron moderator and therefore its presence in the of CI-chondrites plays the crucial role for the neutron transport. This role becomes evident already in the center of the R=10 cm meteoroid, where the maximum at thermal energies can clearly be seen (Fig. 3.3). Above the maximum, which is sharper than that calculated for ordinary chondrites, there is a steep decrease of the flux followed by a slower exponential decrease. For greater radii the shape of the spectra holds but it is shifted to higher flux values.

Compared to the spectra for ordinary chondrites, the values for thermal neutrons for CI-chondrite of radius 40 cm are at the same level as for L-chondrite of radius 85 cm, but

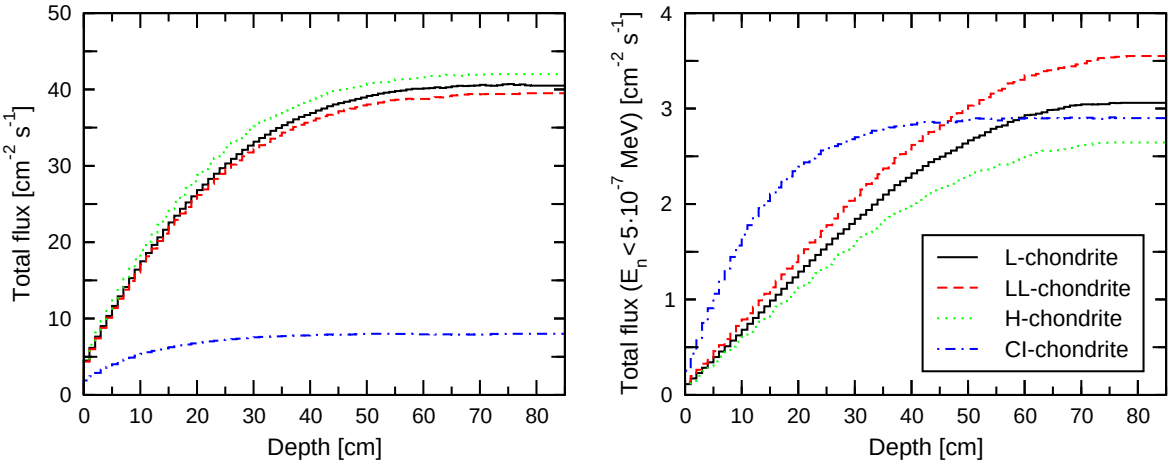

Figure 3.5: Total neutron flux integrated over the whole energy interval (left) and over energies below 0.5 eV (right) as a function of depth in a meteoroid with radius 85 cm for bulk chemical composition of L-, LL-, H-, and CI-chondrite. Data are normalized to a total incident flux of primary protons $J_0(E > 10 \text{ MeV}) = 1 \text{ cm}^{-2} \text{ s}^{-1}$.

for higher energies the fluxes are much lower. This fact is reflected in the depth dependence of the total neutron flux of various chondrite classes (Fig. 3.5 left). The integral flux in CI-chondrite near surface is 2 times lower than in the ordinary chondrites and the difference increases with depth to a factor of 8 in the center area.

Depending on the shape of the particular excitation function, the most important for n-capture reactions are usually the neutron fluxes at thermal and epithermal energies. Comparing only the total flux for energies below 0.5 eV, the hydrogen presence becomes clearly visible (Fig. 3.5 right). It causes a steep increase of thermal neutron fluxes at small depths below the surface of the meteoroid, followed by a broad maximum and for larger radii by a slow exponential decrease.

3.2.2 Capture rates of cosmogenic radionuclides in L-chondrites

The calculated production rate depth profiles of n-capture produced ^{36}Cl, ^{41}Ca, ^{60}Co, ^{59}Ni, and ^{129}I for meteoroids of L-chondrite composition and radii 10, 20, 25, 30, 35, 40, 50, 65, 85, 100, 120, 150, 200, 300 and 500 cm are shown in Fig. 3.6. All production rates are calculated for total primary particle flux of 1 proton cm^{-2} s^{-1}. In the case of ^{36}Cl and ^{59}Ni the cross section is the same for both ENDF/B-VI and JEF-2.2. For ^{41}Ca and ^{129}I we took the JEF excitation functions in which wider resonance region is resolved. For ^{60}Co there are only small differences in the resonance region of excitation functions and their effect on the depth profiles is very small.

For all considered nuclides the presented depth profiles are very similar and show the same characteristic features. Profiles in meteoroids with radius below $\approx$ 85 cm are increasing from the surface to the center. For these radii the capture rates are also increasing monotonously with the size of the meteoroid. The values for the smallest radii are too small to be seen

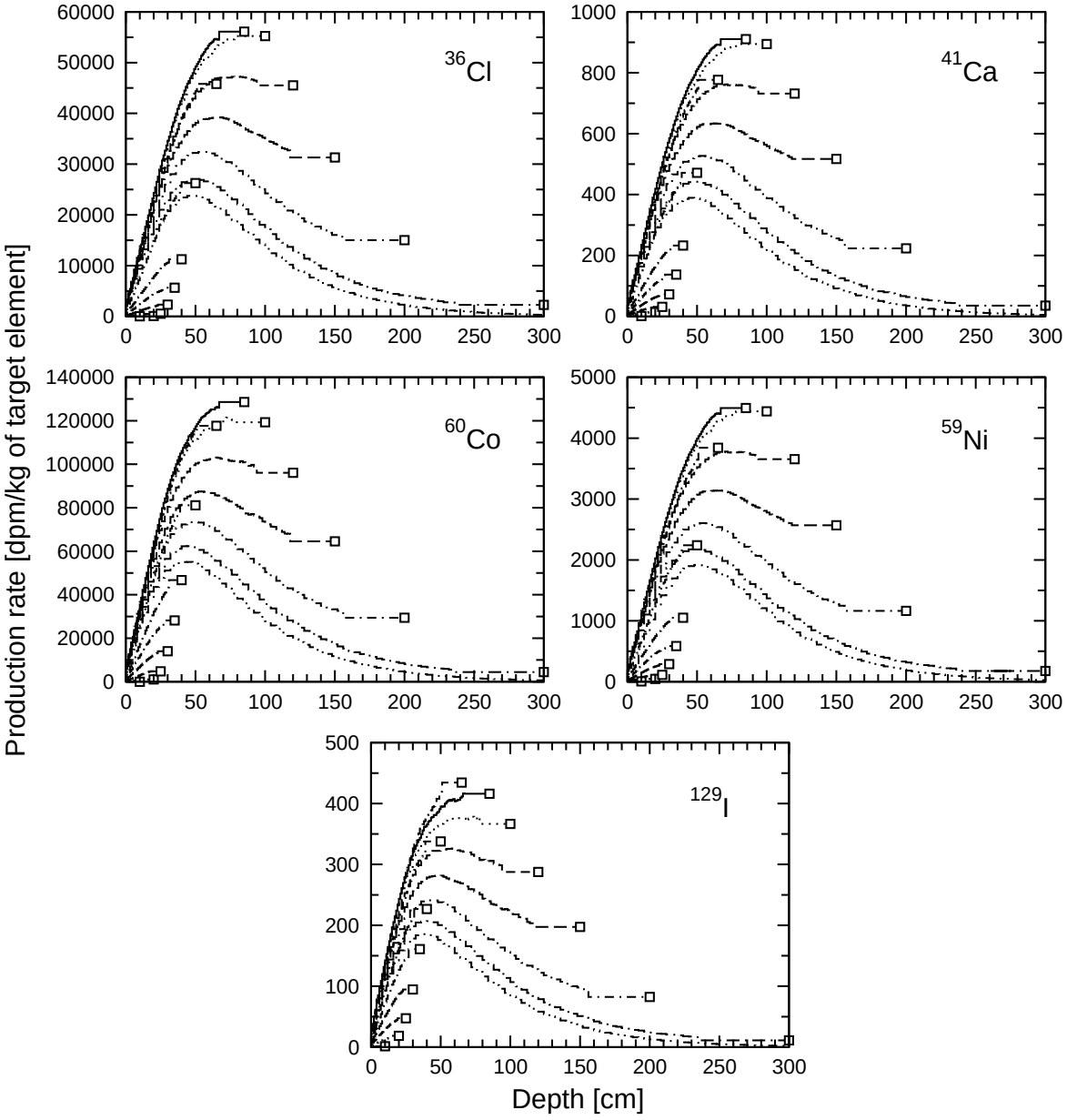

Figure 3.6: Neutron capture production rate depth profiles of cosmogenic isotopes ^{36}Cl, ^{41}Ca, ^{60}Co, ^{59}Ni, and ^{129} in meteoroids with radii 10, 20, 25, 30, 35, 40, 50, 65, 85, 100, 120, 150, 200, 300, and 500 cm and the bulk chemical composition corresponding to L-chondrite. Data are normalized to a total incident flux of primary protons $J_0(E > 10 \text{ MeV}) = 1 \text{ cm}^{-2} \text{ s}^{-1}$.

in given scales. The differences between the production in the center of 10 cm and 85 cm meteoroid range from two orders of magnitude for ^{129}I to almost five orders of magnitude for ^{36}Cl. For larger meteoroids the production starts to decrease after reaching a maximum at depth around 50 cm. The absolute values are also starting to decrease with increasing meteoroid size.

For all nuclides except for ^{129}I, the maximum production rate value is reached in the center

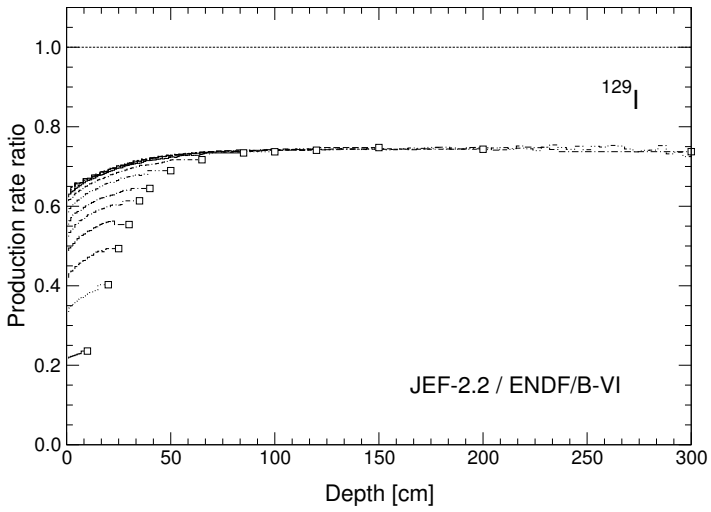

Figure 3.7: Production rate depth profiles of cosmogenic nuclide ^{129}I in L-chondrites with radii from 10 to 500 cm calculated using excitation function from JEF-2.2 file relative to those calculated using ENDF/B-VI file.

of the meteoroid with radius 85 cm. For ^{129}I the maximum production rate is calculated in the center of 65 cm large meteoroid. This is due to the fact, that the shape of the excitation function for this isotope shows very high cross section values at energies above the resolved resonance region (up to a few MeV) (Fig. 3.2). The values are more than order of magnitude higher than the cross sections below the resonance region. Therefore, also the neutron fluxes at higher energies become important for the n-capture production.

From identical excitation functions for the production of ^{36}Cl and ^{59}Ni for both considered neutron data files it is obvious that the depth profiles calculated using these cross sections are also identical. The differences in the mean depth profiles for ^{41}Ca and ^{60}Co calculated using JEF-2.2 and ENDF/B-VI are $\approx 0.4\%$ which is far below the uncertainty of the calculated neutron fluxes.

The situation is different for ^{129}I. Its production rates calculated using excitation function from JEF-2.2 relative to those calculated using the cross sections from ENDF/B-VI are shown in Fig. 3.7. The capture rate calculated using JEF-2.2 for radii above 70 cm is 27% lower at depths above ≈ 60 cm and the difference increases to 36% near surface. In smaller meteoroids the difference depends on the depth and similarly as for small depths in larger meteoroids it increases in surface direction. Here the difference is size dependent and for a radius of 25 cm it reaches more than 50%. The changing differences at small depths are caused by the fact that there are too few (or none) thermal neutrons and so the importance of the high energy part of excitation function that differs in both libraries is changing. As in such small meteoroids the n-capture production can be neglected in comparison to the spallation production these differences need not be considered.

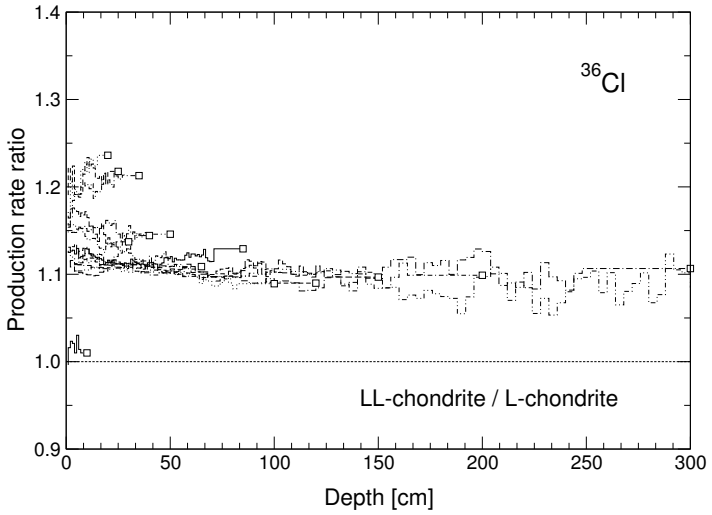

Figure 3.8: Production rates of ^{36}Cl in LL-chondrites as a function of depth in cm relative to those in L-chondrites for meteoroid radii from 10 to 500 cm.

3.2.3 Capture rates in LL-, H-, and CI-chondrites

The differences in neutron fluxes for LL- and H-chondrites, when compared to those for L-chondrites (Fig. 3.4), imply also the differences in the neutron capture production of cosmogenic nuclides in these chondritic classes. In Fig. 3.8 production rate depth profiles of ^{36}Cl in LL-chondrites of various radii are shown relative to those in L-chondrite. Because of higher oxygen content and lower iron content in the composition, the production is higher in LL-chondrites. For radii above 50 cm the production of ^{36}Cl is approximately 10% higher than in L-chondrites at all depths. This means that the shape of the depth profiles for L- and LL-chondrites is identical. The differences for smaller meteoroids change between 0% and 30%. This is caused by the different development of neutron fluxes but also by the fact that the neutron spectra in these meteoroids have very few thermal neutrons and therefore small changes in thermal neutron fluxes which are due to the statistical fluctuations cause big changes in nuclide production. As the absolute capture production rate values are small in small meteoroids when compared to spallation production, we do not discuss it further. The relative capture rates look very similar for other investigated isotopes. The mean ratios in meteoroids with radii above 50 cm are 1.1 for ^{36}Cl, 1.08 for ^{41}Ca, 1.01 for ^{60}Co, 1.09 for ^{59}Ni, and 0.95 for ^{129}I.

The ^{36}Cl production rate depth profiles in H-chondrites relative to those in L-chondrites are shown in Fig. 3.9. On the left the ratios were calculated at the same depth in cm so the practically linear decrease at depth above 10 cm for radii above 50 cm is a direct implication of different bulk densities of the chondrite classes. When the densities are taken into account by rescaling the depths to the units of g cm^{-2}, the decrease disappears (Fig. 3.9 right). Again, the relative capture rate depth profiles have similar shapes for other isotopes.

Due to lower oxygen and higher iron abundance in H-chondrites than in L-chondrites, the

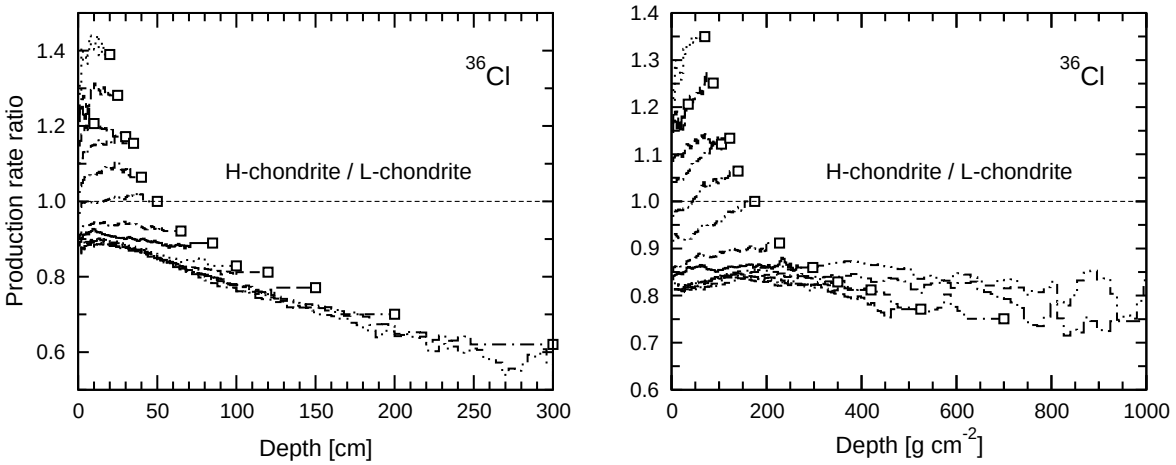

Figure 3.9: Production rates of ^{36}Cl in H-chondrites as a function of depth in cm (left) and g cm^{-2} (right) relative to those in L-chondrites for meteoroid radii from 10 to 500 cm.

mean values of the ratio for radii above 50 cm are opposite to those for LL-chondrites for all considered isotopes (when the depth dependence in g cm^{-2} is considered). The values are 0.82 for ^{36}Cl, 0.85 for ^{41}Ca, 0.93 for ^{60}Co, 0.84 for ^{59}Ni, and 1.2 for ^{129}I.

Following the characteristics of the differential neutron fluxes in CI-chondrites, the production rate depth profiles of cosmogenic isotopes in this type of chondrites also show significant differences to other considered chondrite classes. The ^{36}Cl depth profiles in CI-chondrites of radii from 10 cm to 500 cm are shown in Fig. 3.10. Also in this case the presented production rates are normalized to the total primary particle flux of 1 proton cm^{-2} s^{-1}. As mentioned above, high hydrogen content causes faster thermalization of neutrons. Therefore, unlike ordinary chondrites, there are considerable production rates already in the center of CI-chondrite with radius of 20 cm. When the bulk densities are taken into account and the production rates are drawn as a function of depth in units of g cm^{-2}, the differences are even larger.

After a steep increase to the maximum at $\approx$ 65 cm the production rates in CI-chondrites slowly decrease. For larger meteoroids the maximum shifts to smaller depths, reaching the depth of about 30 cm for the meteoroid with radius 500 cm.

We also investigated the effects of "neutron poisons" such as Sm and Gd in the composition of ordinary chondrites. Typical abundances of these elements in the bulk chemical composition of all chondrite classes are of order of 0.1 ppm [62]. The results showed that the effects on the neutron capture caused by the presence of these elements are much smaller than the statistical uncertainties of the model calculations.

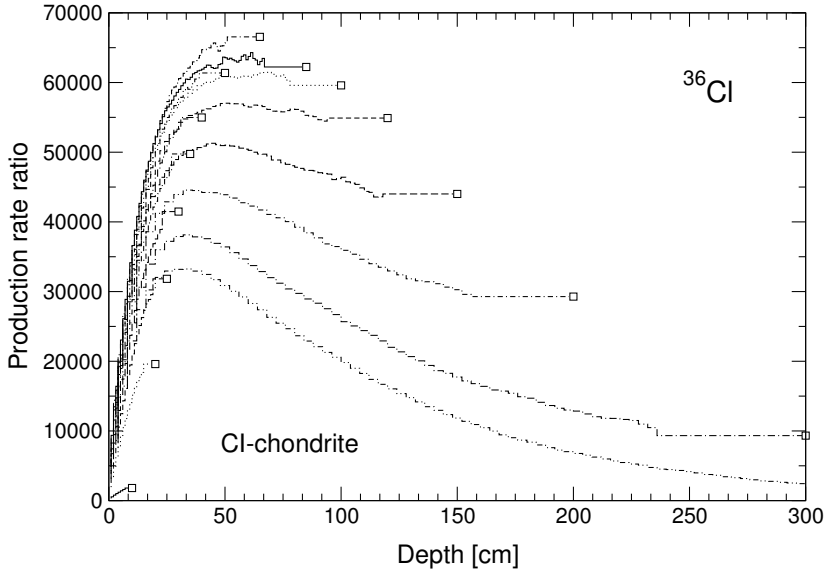

Figure 3.10: Production rate depth profiles of ^{36}Cl in CI-chondrites for meteoroid radii from 10 to 500 cm. Data are normalized to a total incident flux of primary protons $J_0(E > 10 \text{ MeV}) = 1 \text{ cm}^{-2} \text{ s}^{-1}$.

3.2.4 The mean GCR particle flux

To make the model complete, the value of the mean primary GCR particle flux J_0 with energies above 10 MeV has to be determined. Its value corresponds to the value of the mean solar modulation parameter Φ. For each value of Φ the particular J_0 for primary protons can be calculated by integrating the equation (1.2) over energies above 10 MeV. The α-particles are then taken into account by multiplying the value by the α-scaling factor 1.55.

We investigated the dependence of the production rates on the solar modulation parameter Φ by calculating production rates in the center of L-chondrite with radius 85 cm for Φ from 100 MeV to 1000 MeV. The results were multiplied by the corresponding J_0 value and plotted as a function of it (Fig. 3.11). The correlation between capture rates and J_0 is not linear because for larger J_0 values (i.e., smaller Φ values) there is mainly an increase of low energy primary particles (Fig. 1.1) that have lower multiplicities for secondary particles and consequently lower production rates. However, for certain subintervals this dependence can be with good accuracy considered linear. Therefore, it is sufficient to calculate the production rates for one particular value of solar modulation parameter Φ and $J_0(E > 10 \text{ MeV}) = 1 \text{ cm}^{-2}$ s^{-1} and then scale the results to an appropriate solar modulation by simply multiplying the production rates by the suitable J_0.

Reedy and Masarik [52] and Leya et al. [46] both presented the models for the calculation of the spallation production of cosmogenic nuclides in meteoroids. They determined the J_0 value of the mean primary nucleon flux density at the meteoroid orbits to be 4.8 and 4.06 cm^{-2} s^{-1} respectively by comparing the calculated depth profiles to the radionuclide activities measured in the Knyahinya meteorite.

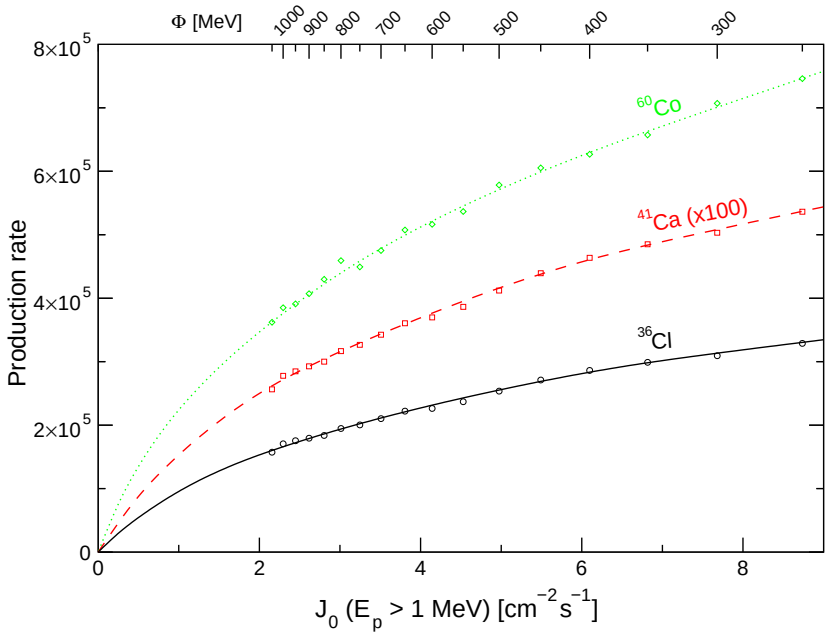

Figure 3.11: Dependence of n-capture GCR production rates of ^{36}Cl, ^{41}Ca (multiplied by 100), and ^{60}Co in the center of L-chondrite with radius 85 cm on the mean GCR particle flux for $E > 10$ MeV shown with corresponding solar modulation parameter. The data are fitted with non-linear function. Production rates are in units dpm per kilogram of target element.

Experimental concentrations of the n-capture produced cosmogenic isotopes in chondrites with determined depths of the samples below the surface are not available. It is caused by the fact, that the size of meteoroids that can survive the ablation in the atmosphere in one piece is too small to enable making up of sufficient thermal neutrons fluxes. Because of that, the production of cosmogenic nuclides in small meteoroids is usually dominated by spallation. As large meteoroids explode before they reach the Earth's surface, the original position of the individual samples inside the meteoroid cannot be determined by direct measurement. Therefore, we used the ^{41}Ca depth profile measured in Apollo 15 drill core [9] for the determination of the mean primary particle flux.

Due to the heliocentric gradient of the GCR flux [64, 65] the J_0 value at Earth's orbit should be 3–6% lower than that at meteoroid orbits. From spallation products measured in lunar samples the J_0 at Earth's orbit was determined to be 4.56 and 4.54 cm^{-2} s^{-1} by Reedy and Masarik [53] and Leya et al. [54] respectively. The later considered together with the value they determined for meteoroid orbit of 4.06 cm^{-2} s^{-1} [46] is not consistent with the direction of heliocentric gradient. This is probably due to the particle spectra they used for production rate calculations.

In our calculations, the Moon was modeled as a sphere with radius 1738 km divided into shells with thickness 5 cm. The bulk density and bulk chemical composition of the lunar regolith used are listed in Table 3.1. Fig. 3.12 shows the calculated neutron spectrum at

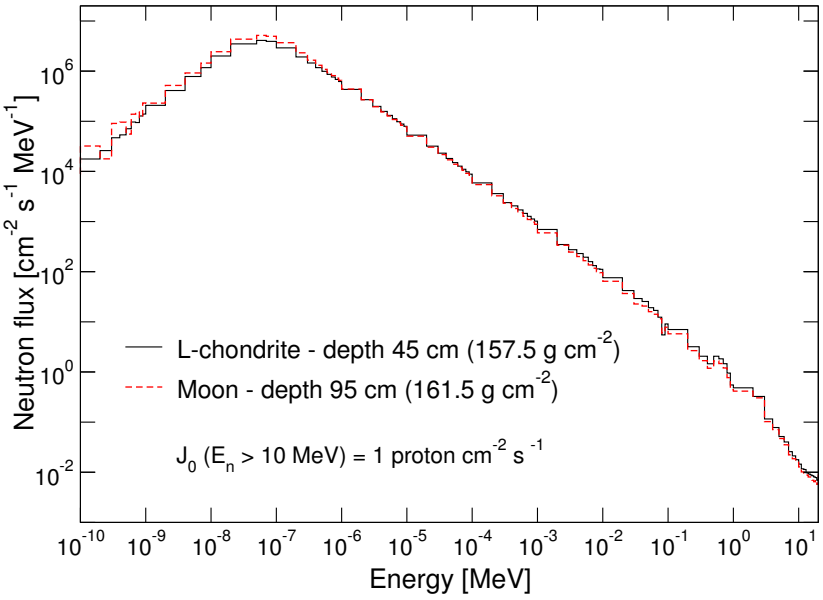

Figure 3.12: Neutron differential flux densities at the depth 95 cm in the Moon and at the depth 45 cm inside the L-chondrite of the same size. Considering bulk density, both depths correspond approximately to the same amnount of material. Data are normalized to a total incident flux of primary protons $J_0(E > 10 \text{ MeV}) = 1 \text{ cm}^{-2} \text{ s}^{-1}$.

depth 95 cm below the surface of the Moon together with the spectrum calculated for the L-chondrite of the same size at depth 45 cm (which corresponds to the same amount of material). While at energies above ≈ 1 eV there are slightly more neutrons in L-chondrite, at thermal energies the lunar neutron fluxes are significantly higher reaching at the energy of the Maxwellian maximum a difference of 20%. This is partly due to the difference in the abundance of light elements like oxygen, but mainly due to the big difference in the amount of iron in the composition. More iron means more secondary neutrons with energies above 1 eV and at the same time, because of its relatively high thermal absorption cross section of 2.562 barns, less thermal neutrons. The differences in thermal neutron fluxes would be much bigger (about a factor of 2), if there weren't such high abundances of strong neutron absorbers samarium and gadolinium in the lunar regolith (with thermal absorption cross sections 5615 and 48780 barns respectively).

The differences in the neutron spectra between the Moon and the L-chondrite directly imply differences in the depth profiles of n-capture produced cosmogenic isotopes. Comparison for ^{41}Ca is shown in Fig. 3.13 with depth given in cm as well as in g cm^{-2}. The depth profiles reach their maxima at about 95 and 45 cm for the Moon and the L-chondrite respectively with the production rate in the Moon being 11% higher.

Fitting this calculated lunar ^{41}Ca depth profile to the measured activities from Apollo 15 deep drill core [9] we obtained the value of the mean GCR particle flux over the last 300 ka

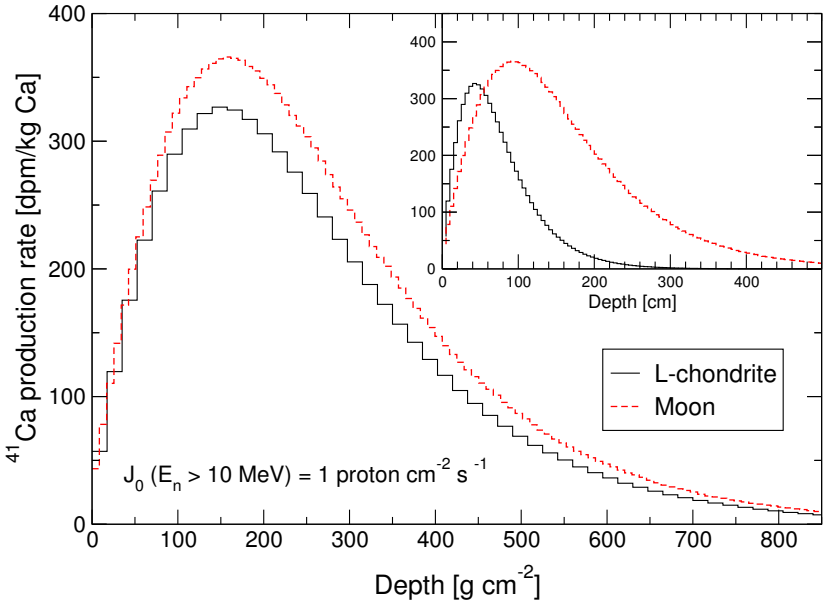

Figure 3.13: Calculated neutron capture depth profile for ^{41}Ca in the Moon compared to that in L-chondrite of the same size. Production rate is shown as a function of depth in units cm as well as g cm^{-2}. Data are normalized to a total incident flux of primary protons $J_0(E > 10 \text{ MeV}) = 1 \text{ cm}^{-2} \text{ s}^{-1}$.

$(\approx 3 \times T_{\frac{1}{2}}(^{41}\text{Ca}),\ T_{\frac{1}{2}}(^{41}\text{Ca}) = 106 \text{ ka})$

$$J_0(E > 10 \text{ MeV},\ \text{Earth's orbit}) = 2.85 \text{ cm}^{-2}\text{s}^{-1} \tag{3.3}$$

This value is 1.6 times lower than the above mentioned values from other authors. We do not know the reason for this difference.

The final calculated ^{41}Ca depth profile for the above J_0 value compared to the experimental data is shown in Fig. 3.14. There is a good agreement with measured activities. The higher measured value near surface is probably due to the SCR proton production via reactions $^{41}\text{K}(p,n)$, $^{42}\text{Ca}(p,pn)$, and $\text{Ti}(p,X)$ which is significant at shallow depths (up to 5–8 g cm^{-2}) and probably wasn't completely separated from the n-capture produced ^{41}Ca during the measurements [9]. For depths over 160 g cm^{-2} the calculated production rates are higher than measured ones. When the depths of all measured samples are increased by ≈ 17 g cm^{-2} (10 cm) the agreement is much better. This indicates that a shift of the depths could happen during and subsequent to sampling.

Using the determined J_0 value we can also successfully describe the ^{60}Co neutron capture production in the lunar surface (Fig. 3.15). No such discrepancies as for ^{41}Ca can be seen when comparing the calculated depth profile to the measured ^{60}Co data from the Apollo 15 long core [55].

Considering the distance of meteoroid orbits from the Sun, the mean GCR particle flux over the last 300 ka is from 2.94 to 3.03 cm^{-2} s^{-1}. We calculated the J_0 as an aritmetic mean

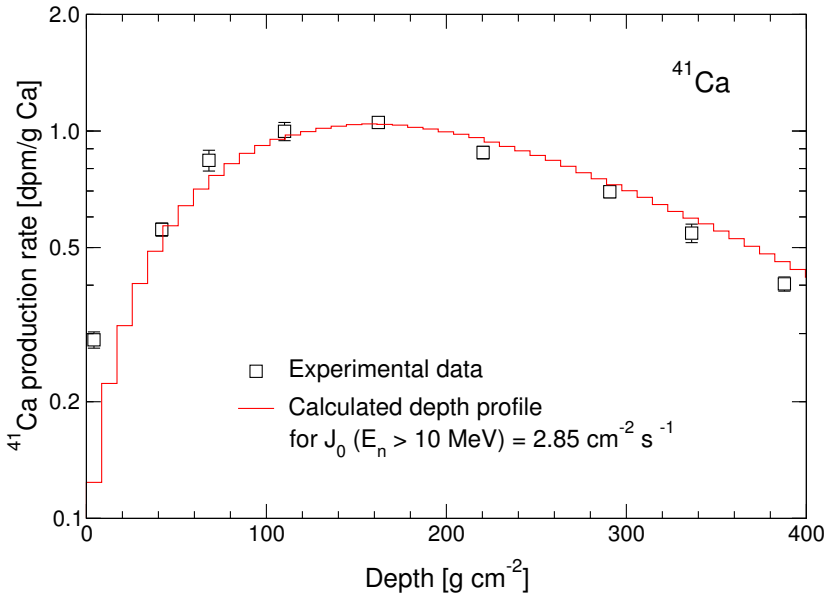

Figure 3.14: Neutron capture produced activities of ^{41}Ca measured in the Apollo 15 drill core [9] together with the depth profile calculated using our model and adjusted to the experimental data by setting the value of J_0 to 2.85 cm^{-2} s^{-1}.

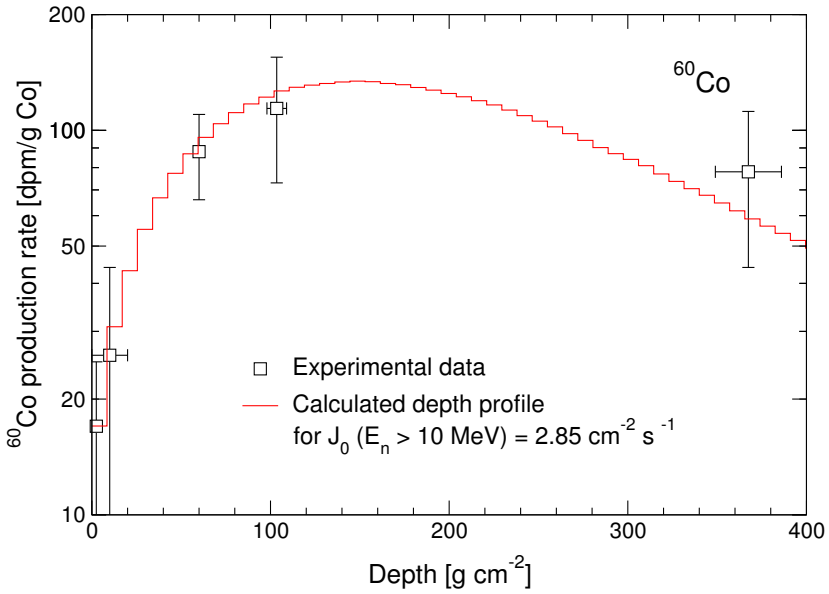

Figure 3.15: Neutron capture produced activities of ^{60}Co measured in the Apollo 15 long core [55] together with the depth profile calculated using our model for $J_0(E > 10$ MeV$) = 2.85$ cm^{-2} s^{-1}.

of this two values

$$J_0(E > 10 \text{ MeV, meteoroid orbits}) = 2.99 \text{ cm}^{-2}\text{s}^{-1} \,. \tag{3.4}$$

Nishiizumi et al. [9] used the LCS to calculate neutron spectra in the same way as we did, with the same bulk chemical composition used. Unlike us, they succeeded to describe the

measured ^{41}Ca activities using the J_0 value 4.56 cm^{-2} s^{-1}. Still the shape of the calculated depth profile is identical with ours (Fig. 3.14). Our investigation of this discrepancy leaded to a conclusion, that this was due to an erroneous version of MCNP they used. While calculating the same neutron spectra as ours, this versions integration of capture rates resulted in lower values for all investigated nuclides. Keeping that in mind, the wonderful agreement of their J_0 values for both spallation and n-capture production rates is startling. For the n-capture production of ^{60}Co the comparison of our calculations with the experimental data [55] is also identical to that of Nishiizumi et al. [9].

Recently, Leya et al. [66] also needed two different J_0 values for the description of spallation and n-capture production of cosmogenic nuclides in the lunar surface. By comparing the calculated depth profiles to the measured ^{41}Ca activities [9] they obtained values 2.64 and 2.36 cm^{-2} s^{-1} for Earth and meteoroid orbits respectively, which are slightly lower than our values. As the cross sections used were the same, the difference could only be caused by different neutron spectra. They used the spectra calculated using codes within the HERMES code system [32] for the solar modulation parameter 490 MeV which they admit are not well suited for such calculation [54]. We believe that this is also due to the fact that they did not consider the abundance of Sm and Gd in the composition of the lunar regolith used in the transport calculation. When these elements are left out, the ^{41}Ca production rate is about 25% higher.

3.2.5 Comparison to other models and experimental data

Both previously mentioned models of Eberhardt et al. [5] and Spergel et al. [57] consider only one class of chondrites, the L-chondrites, assuming that the effects of different bulk composition on thermal neutron fluxes and capture production are negligible. As we showed, for some nuclides these effects can make measurable differences in production rates.

Our calculated maximum production rate values for ^{60}Co and ^{59}Ni are 385 dpm/g Co and 13.5 dpm/g Ni respectively. These are practically identical to those from Eberhardt et al. [5] who obtained values 385 dpm/g Co and 14 dpm/g Ni. While the ^{60}Co capture rate from Spergel et al. [57] of 375 dpm/g Co is also in good agreement with our value, their maximum value for ^{59}Ni of 21 dpm/g Ni is about 50% higher. For ^{36}Cl our calculated 168 dpm/g Cl is significantly lower than the values 220 and 280 dpm/g Cl from Eberhardt et al. [5] and Spergel et al. [57] respectively.

As mentioned above, depth profiles for n-capture produced isotopes in chondrites are not available. Still the cosmogenic nuclide activities were measured in samples from some meteorites.

Activities of ^{60}Co were measured in 12 samples from the Jilin H-chondrite in range 60–229 dpm/kg for an average Co abundance of 792 ppm [67]. Considering its two-stage irradiation history [68] the comparison to the depth profiles from Eberhardt et al. [5] implied

pre-atmospheric radius of 85 cm. Using our calculated ^{60}Co depth profiles for H-chondrite composition we can successfully describe the Jilin data when considering radius 60–100 cm. The same limits on radius are obtained when comparing the calculated ^{41}Ca depth profiles with the experimental data 200–2000 dpm/kg Ca [69].

Bogard et al. [70] measured the ^{36}Cl and ^{41}Ca activities in several samples from the Chico L-chondrite. According to our model, the ^{41}Ca data imply the constrains on the pre-atmospheric radius 55–300 cm. On the other hand, the ^{36}Cl activities of 160–260 dpm/g Cl are higher than our highest calculated production rate. This can be due to the fact that the cross sections for the (n, γ) reaction on $^{\mathrm{nat}}$Cl were used in place of the unavailable cross sections for the reaction on ^{35}Cl.

4 Neutron cross sections and terrestrial nuclide production

Several thick-target experiments were performed in order to simulate the interactions of GCR protons with stony and iron meteoroids in space. Four artificial stony meteoroids and one iron meteoroid were irradiated isotropically by 600 MeV and 1.6 GeV protons at CERN and at the Laboratoire National Saturne/Saclay [46, 71–73]. A method was developed that allows unfolding of neutron excitation functions from measured production rates of produced nuclides. This method is based on an assumption, that the interactions of protons with target material can be described accurately. Therefore, the more recent of these irradiations were proceeded by a number of thin- and thick-target experiments in which the cross sections for proton induced reactions were measured. From these measurements a consistent set of proton excitation functions is available for about 550 target–product combinations relevant for cosmochemical applications [35, 36].

Using these measured proton and evaluated neutron cross sections the production of cosmogenic nuclides in the artificial meteoroids was described successfully within experimental errors [46]. Afterwards, the new cross sections were used for Monte Carlo simulation of nuclide production in real meteoroids [8] and lunar surface [54]. As mentioned in section 1.6.3 for most neutron induced reactions the cross sections significantly differ from those used in previous works of other authors [7, 52, 53], which consequently leaded to different estimates of the mean GCR particle flux.

Various models for the particle production and transport and the production of cosmogenic nuclides in the Earth's atmosphere were developed [1, 4, 6, 30, 51]. For the best model is currently considered the model of Masarik and Reedy [6]. Here we apply the new set of cross sections to their model. Production rates of cosmogenic radionuclides were calculated using the formula (1.6). In the following, the input particle spectra and cross sections used in the comparison are described in detail.

4.1 Proton and neutron fluxes

Masarik and Reedy [6] calculated the transport of all charged particles and neutrons with energies above 20 MeV using the GEANT code [33]. Transport of neutrons with $E < 20$ MeV

Table 4.1: Bulk chemical compositions (in weight percent) of the Earth's surface and atmosphere used in calculations.

Element	Soil	Atmosphere
H	0.2	–
N	–	75.5
O	47.3	23.2
Na	2.5	–
Mg	4.0	–
Al	6.0	–
Si	29.0	–
Ar	–	1.3
Ca	5.0	–
Fe	6.0	–

was simulated using MCNP. In their earlier work Masarik and Reedy [51] used LAHET code [31] instead of GEANT to simulate the high energy particle interactions in the atmosphere. The transition from LAHET to GEANT was dictated by the built-in physics of these codes. LAHET is applicable only for particles with energies below 10 GeV. Because of the deflection of low energy particles by the geomagnetic field, the importance of particles with energies above 10 GeV is crucial. GEANT was written for use in high energy particle physics and is better suited to simulate the high energy cosmic ray interactions in the atmosphere.

They modelled the solid Earth as a sphere with radius 6378 km and surface density of 2 g cm^{-3} and average elemental composition given in Tab. 4.1. The Earth's atmosphere was modelled as a spherical shell with an inner radius 6378 km and thickness of 100 km. The atmospheric shell was divided into 34 concentric subshells with thickness 30 g cm^{-2}. The average elemental composition of the atmosphere is also given in Tab. 4.1. The atmospheric density was approximated by $\rho(h) = 1.27 \times 10^{-3}\ \mathrm{e}^{-0.1091\,h}$ g cm^{-3} for $h < 9.73$ km and $\rho(h) = 2.03 \times 10^{-3}\ \mathrm{e}^{-0.1573\,h}$ g cm^{-3} for $h > 9.73$ km, where h is the altitude above the sea level in km.

Geomagnetic field was included in calculations by considering 9 latitudinal bins corresponding to steps of 10 degrees in geomagnetic latitude with vertical cutoff rigidities increasing from 0 GV on the poles to 14.5 GV on the equator.

To investigate the variations of solar activity and geomagnetic field intensity Masarik and Beer [6] simulated particle transport for values of solar modulation parameter Φ in range $0 - 1000$ MeV and for the Earth's magnetic field from 0 to 2 times its present intensity. To make the comparison for different values of the mean GCR particle flux we used their spectra for $\Phi = 550$ MeV and $\Phi = 650$ MeV corresponding to J_0 values of 4.65and 3.9 protons cm^{-2} s^{-1} respectively[1]. The calculated energy differential proton and neutron fluxes near poles and near the equator at various depths in the atmosphere for $\Phi = 550$ MeV and present intensity of geomagnetic field is shown in Fig. 4.1.

[1]See the discussion in section 1.6.3.

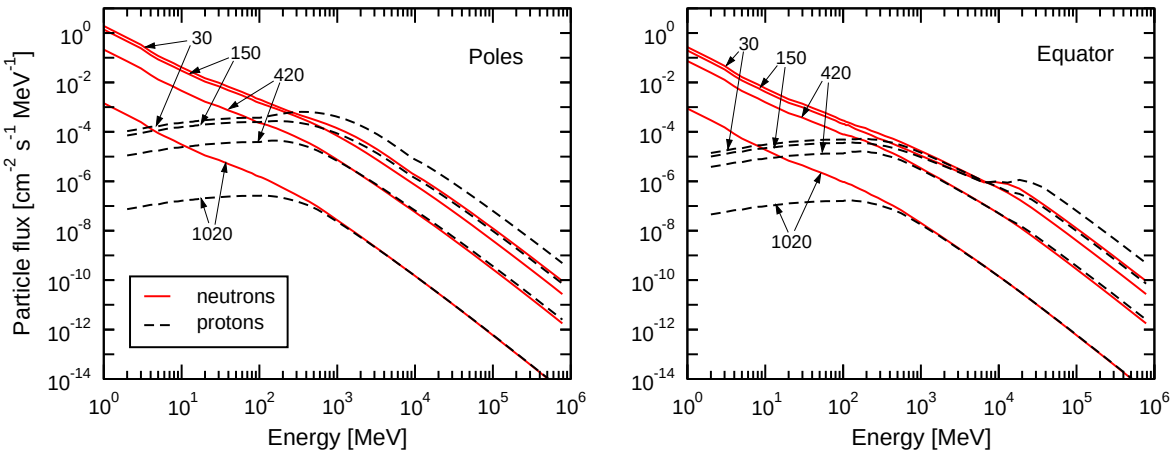

Figure 4.1: Differential proton and neutron fluxes near poles and near the equator at depths 30, 150, 420, and 1020 g cm^{-2} in the Earth's atmosphere for $\Phi = 550$ MeV and present geomagnetic field intensity [6].

To calculate the production rates of cosmogenic nuclides in the surface rocks the proton and neutron fluxes at given depth were transported further in a 4 cm thick shell with typical litospheric bulk composition and density. Masarik and Beer [6] calculated only differential proton and neutron fluxes in the surface layer for zero geomagnetic field intensity which is equivalent to the properties near poles. They also calculated the fluxes only for solar modulation $\Phi = 550$ MeV.

4.2 Cross sections

In works [6, 51] the cosmogenic nuclide production rates were calculated using the cross sections collected and evaluated by R. C. Reedy. The cross sections measured and evaluated by the group of R. Michel were developed with aim of extraterrestrial applications and were not used for the nuclide production rate calculations in the Earth's atmosphere and surface material before.

In the atmosphere, nitrogen is the main target element. On the other hand, its content in meteorites is very low [61, 62]. Therefore, the reactions on nitrogen were not investigated in detail during the irradiation experiments and there is only a limited number of cross sections for the reactions on nitrogen available from the group of Michel. From nuclides whose production in the atmosphere is usually studied there are only excitation functions for the production of ^{7}Be and ^{10}Be. Those for ^{10}Be from oxygen and nitrogen are shown in Fig. 4.2 together with the cross sections from Reedy used in [6]. It can be seen that while the cross sections for proton induced reactions are practically identical, there are significant differences for neutron induced reactions. Also shown in Fig. 4.2 are the cross sections for the production of ^{14}C from oxygen and ^{36}Cl from calcium. Also here the differences for neutron induced reactions are apparent. Generally speaking, there are differences mainly in medium

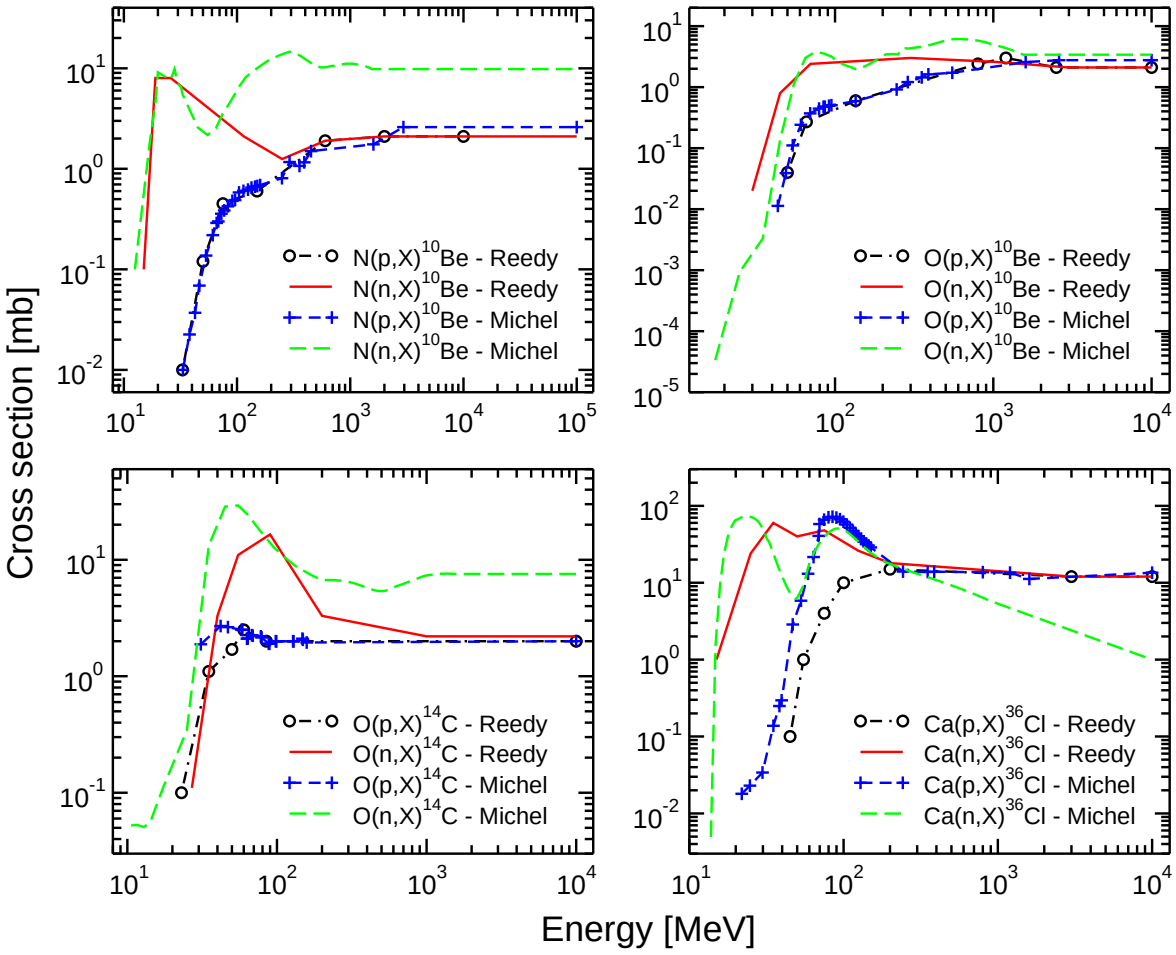

Figure 4.2: Cross sections for the production of ^{10}Be from oxygen and nitrogen, ^{14}C from oxygen and ^{36}Cl from calcium by both protons and neutrons from the group of R. Michel compared to those from R. C. Reedy.

energy region but for several reactions there are also significant differences between cross sections of Michet and Reedy at high energies.

Reedy always constructed the neutron excitation functions so that at high energies the cross section should be the same as for equivalent proton reaction (the only exception are the excitation functions for reactions Si$(n, X)^{14}$C and Si$(p, X)^{14}$C, Fig. B.7). This assumption is based on the fact that at high energies the Coulomb interaction of protons with target nuclei is negligible and so the interaction of protons and neutrons is equivalent.

On the other hand, there are many excitation functions of Michel that have different cross section value for protons and neutrons at high energies. For cross sections used in this work the maximum difference is a factor of 4 in favour of neutron induced reactions. The differences were not explained yet, but recent measurements of the group of Sisterson [47] show similar differences.

Cross sections for all reactions considered in the comparison can be found in appendix B.

Table 4.2: Atmospheric production rates of cosmogenic ^{7}Be and ^{10}Be calculated for solar modulation parameters $\Phi = 550$ and 650 MeV using $J_0 = 4.56$ and 3.9 cm^{-2} s^{-1} compared to values determined by other authors.

Reference	Φ [MeV]	Globally averaged production rate [atoms cm^{-2} s^{-1}]	
		^{7}Be	^{10}Be
Lal & Peters [1]	630	0.081	0.045
O'Brien et al. [30]	580	0.0631	0.0285
Masarik & Reedy [51]	550	0.0129	0.0201
Masarik & Beer [6]	550	0.0354	0.0184
Our calculations	**650**	**0.0434**	**0.0264**
	550	0.0532	0.0321

4.3 Results and discussion

4.3.1 Atmospheric production of ^{7}Be and ^{10}Be

For each depth in the atmosphere and each latitudinal bin the production rate of cosmogenic nuclides ^{7}Be and ^{10}Be was calculated. Because of atmospheric mixing, these production rates are not directly comparable to the nuclide concentrations observed in the archives. Therefore the integration over the whole atmospheric thickness followed by the weighted average over all latitudes was made. Final obtained values were compared to those from [6] based on the same particle fluxes as well as to other values obtained from more or less different models. Model used in [51] used the LCS for the simulation of particle transport and except for the reaction N$(n, X)^{10}$Be the cross sections used were the same as in [6]. Models used in [1] and [30] are based on completely different methods and do not use nuclear cross sections as input data. Final obtained values for all these models are listed in Table 4.2.

As the selection of cross sections determines the mean GCR particle flux and the solar modulation to be used, we calculated the production rates using the proton and neutron spectra for $\Phi = 650$ MeV. As mentioned in section 1.6.3, this corresponds to $J_0(E > 10 \text{ MeV}) = 4.06$ cm^{-2} s^{-1} at meteoroid orbits [8]. According to heliocentric gradient of GCR flux, the J_0 value at Earth's orbit is 3–6% lower than that at meteoroid orbits [64, 65]. However, Leya et al. [54] determined J_0 at Earth's orbit to be 4.54 cm^{-2} s^{-1} which is 12% higher than that for meteoroids. This is probably due to the particle spectra used for the calculation of 2π irradiation of the Moon which they admit are not well suited for such calculation[2]. Therefore, we started from the J_0 they determined for meteoroid orbits [8] and decreased it by 4.5% obtaining the mean GCR particle flux at Earth's orbit of 3.9 cm^{-2} s^{-1}. In the following, this value was used for all calculations of cosmogenic nuclide production rates in the Earth's atmosphere and terrestrial surface rocks with the cross sections from the group of Michel.

The results are directly comparable to the results from [6, 51]. For the comparison we

[2]See the discussion in section 3.2.4.

also calculated the production rates for $\Phi = 550$ MeV and $J_0 = 4.56$ cm^{-2} s^{-1} obtained in [7] but these results are not physically meaningful.

The value obtained for ^{7}Be is 23% higher than the value from [6] and factor of 2.4 higher than the value from [51]. Similarly, our value for ^{10}Be is 43% and 31% higher than the values in these works respectively. Thus it is obvious that the two combinations "*cross sections* – J_0" of the group of Reedy and the group of Michel that give very similar production rate results for meteorites are not equivalent for the atmosphere. However, the uncertainties in cross sections for [6, 51] as well as for our cross sections are quite high. In both cases they are estimated to be for proton induced reactions within a few per cent. For neutron induced reactions the errors of cross sections from Reedy are within 30–50% (at worst a factor of 2). For the reasons discussed in previous section, the highest errors among the neutron cross sections from Michel have the excitation functions for the reactions on nitrogen (50–100%). Considering this fact, our production rates agree with those from [6, 51].

The production rates from [1] and [30] are even higher than our values. Our calculated production rate of ^{7}Be is only 7% lower than the value obtained in [30]. For ^{10}Be the difference is 31%. The values from [1] for both isotopes are about a factor of 2 higher than our values.

Comparison of theoretical values to the measured nuclide concentrations in various enviromental systems is not straightforward. While the calculations represent the global mean values, the experimental data reflect to some extent the local effects. Considering these effects would require to include models for the nuclide deposition which depends on the air circulation in the atmosphere, precipitation, various chemical reactions and many other processes occuring in the atmosphere and archives.

Wide range of measured ^{10}Be concentrations in various archives confirms presence of such effects. The lowest value of 0.016 atoms cm^{-2} s^{-1} was measured in the Dye 3 ice core [74], the highest value was measured in precipitation, 0.038 atoms cm^{-2} s^{-1} [75]. The closest value to our was measured in the sediment cores, 0.026 atoms cm^{-2} s^{-1} [76].

4.3.2 Cosmogenic nuclide production in surface rocks

The (un)available particle spectra in the surface layer determined the boundaries for our calculation. We compared the production rates of ^{10}Be, ^{14}C, ^{21}Ne and ^{26}Al in SiO_2 (quartz) and ^{36}Cl in CaO (calcite) calculated with the spectra for $\Phi = 550$ MeV near geomagnetic poles using the cross sections of Michel and $J_0 = 3.9$ cm^{-2} s^{-1} to those calculated using the cross sections of Reedy and $J_0 = 4.56$ cm^{-2} s^{-1}. This particular target–product combinations were selected in order to compare the results to the calculations of Masarik and Reedy [51] who used Reedy's cross sections but different particle fluxes and also to the measured production rates. All values are listed in Table 4.3.

Except for ^{10}Be production rate from quartz and ^{36}Cl production rate from calcite, production rates calculated using the cross sections of Michel are higher than those calculated

Table 4.3: Production rate of cosmogenic nuclides ^{10}Be, ^{14}C, ^{21}Ne and ^{26}Al from SiO_2 and ^{36}Cl from CaO in the surface layer at the sea level (atmospheric depth 1033 g cm^{-2}) near geomagnetic poles calculated for solar modulation parameter $\Phi = 550$ MeV using the mean GCR particle flux of 4.56 protons cm^{-2} s^{-1} with Reedy's cross sections (denoted here as P_{R}) and 3.9 cm^{-2} s^{-1} with Michel's cross sections (denoted here as P_{M}). These are compared to values determined in [51] and to experimental data from various authors.

Nuclide	Target	Production rate [atoms yr^{-1} (g of target)$^{-1}$]			
		$\boldsymbol{P_{\mathrm{M}}}$	P_{R}	Masarik & Reedy [51]	measured
^{10}Be	SiO_2	**4.40**	4.58	5.97	6.0 [77, 78], 6.4 [79]
^{14}C	SiO_2	**21.0**	18.4	18.6	20 [80]
^{21}Ne	SiO_2	**22.2**	15.3	18.4	21 [81]
^{26}Al	SiO_2	**33.2**	30.2	36.1	36.8 [77, 78], 41.7 [79]
^{36}Cl	CaO	**35.6**	37.7	46.2	54 [82], 52 [83]

using Reedy's cross sections. Lower value for ^{10}Be is due to the fact that for silicon the cross sections of Reedy are significantly higher at energies from threshold up to $\approx$ 400 MeV. In this region also Reedy's cross sections from oxygen are comparable to Michel's and therefore the higher J_0 value implies higher contribution to the final production rate. Lower value for ^{36}Cl is caused by the steep decrease of neutron cross sections from Michel for energies above 300 MeV.

It is important to note that for a proper calculation using Michel's cross sections and $J_0 = 3.9$ cm^{-2} s^{-1} the differential particle fluxes calculated for primary proton spectrum for $\Phi = 650$ MeV would be needed. As this primary spectrum would be harder (with higher mean proton energy) it would result in higher proton and neutron fluxes at the sea level and consequently higher production rates. We estimate this contribution to be $\sim 5\%$.

Another factor that would increase the production rate is considering reactions with incident muons. Muon fluxes at the sea level become significant and their importance increases even more when going to larger depths. Because of the lack of the data for reactions with muons we did not calculate this contribution. However, it was estimated to be relatively low $\sim 10\%$ [84].

Considering the uncertainties of cross sections, all calculated production rates agree well with experimental data.

5 Neutron transport for activation experiments

Contrary to their importance for various applications, the availability of neutron cross sections for the production of residual nuclides above 30 MeV is marginal. A solution of this problem is to perform irradiation experiments with quasi-monoenergetic neutrons produced by the $^{7}\mathrm{Li}(p,n)^{7}\mathrm{Be}$ reaction.

Within the HINDAS project, activation experiments were performed in order to determine excitation functions for the production of residual radionuclides from a variety of target elements up to 175 MeV.

The research group at the ZSR/Hanover, Germany is involved in such experiments. The unfolding method for evaluation of neutron cross sections from production rate measurements was developed here and tested on the production of cosmogenic nuclides in meteorites and lunar samples [e.g. 8, 46, 85]. For the evaluation, an accurate description of the neutron field inside the targets is necessary.

In this chapter, the Monte Carlo calculations of neutron transport for the neutron activation experiments are presented. First, the unfolding method itself is explained followed by the description of the irradiation experiments. Afterwards, the semi-empirical model for the quasi-monoenergetic neutron spectrum construction is described. Finally, the transported neutron spectra are presented and discussed together with the preliminary results of evaluated cross sections.

5.1 Evaluation of neutron cross sections

Because of zero electric charge neutrons cannot be directly accelerated to desired energies. For energies above ≈ 14 MeV well studied (p,n)-reactions are used for neutron production. However, this only results in quasi-monoenergetic neutron spectra. These are described using differential flux density of particles [$\mathrm{cm}^{-2}\ \mathrm{s}^{-1}\ \mathrm{MeV}^{-1}$]

$$\varphi_E = \frac{\mathrm{d}\varphi(E)}{\mathrm{d}E}\ , \tag{5.1}$$

where $\mathrm{d}\varphi(E)$ is the flux density of all particles with energy in interval $(E; E+\mathrm{d}E)$. One can then calculate the spectrum averaged cross section value for particular nuclear reaction given

by the excitation function $\sigma(E)$ as

$$\overline{\sigma} = \frac{\int_{E_\mathrm{T}}^{\infty} \sigma(E)\,\varphi_E\,\mathrm{d}E}{\int_{E_\mathrm{T}}^{\infty} \varphi_E\,\mathrm{d}E} = \frac{R}{\int_{E_\mathrm{T}}^{\infty} \varphi_E\,\mathrm{d}E}\,, \tag{5.2}$$

where E_T is the threshold energy of the reaction. Here R [s^{-1}] stands for response integral of the reaction. Its connection with the nuclide production becomes clear when considering simple case of irradiation using particles with spectral flux density φ_E. The number of produced nuclei N then changes as

$$\frac{\mathrm{d}N}{\mathrm{d}t} = N_T \int_{E_\mathrm{T}}^{\infty} \sigma(E)\,\varphi_E\,\mathrm{d}E - \lambda\,N = N_T\,R - \lambda\,N\,, \tag{5.3}$$

where N_T is a number of atoms of target element T per gramm of target and λ is decay constant for produced nuclide. So R can be calculated directly from measured activity of the produced nuclide.

The response integral contains the information about the spectrum averaged cross section of the reaction over the energy interval $(E_\mathrm{T}; \infty)$. However, in the quasi-monoenergetic spectrum 30–50% of neutrons lie within the high-energy peak right below the proton energy, so the weight of cross section values in this energy region saved in the response integral is higher than for the low-energy part. Irradiations with neutron spectra produced at different proton energies allow deconvolution of cross section values for particular energies.

For here presented neutron activation experiments the least-squares-adjustment is used for deconvolution of excitation functions from the response integrals. In the following $\mathbf{R}_\mathrm{exp} = (R_{\mathrm{exp}\,1}, \ldots, R_{\mathrm{exp}\,N})$ represents vector of response integrals for the particular reaction product obtained from N irradiations and

$$\mathbf{\Phi} = \begin{pmatrix} \phi_{E\,11} & \cdots & \phi_{E\,1M} \\ \vdots & \ddots & \vdots \\ \phi_{E\,N1} & \cdots & \phi_{E\,NM} \end{pmatrix} \text{ where } \quad \phi_{E\,nm} = \int_{E_{m-1}}^{E_m} \varphi_{E\,nm}\,\mathrm{d}E \tag{5.4}$$

is the matrix of N neutron flux densities in M energy bins.

Experimental uncertainities of $\mathbf{R}_\mathrm{exp}$ are taken into account in the form of the covariance matrix $\mathbf{K}_{R\mathrm{exp}}$ whose elements for L measurements of $R_{\mathrm{exp}\,i}$ and $R_{\mathrm{exp}\,j}$ are given as

$$K_{ij} = \frac{1}{L(L-1)} \sum_{k=1}^{L} (R_{ik} - \overline{R_i})(R_{jk} - \overline{R_j})\,. \tag{5.5}$$

Diagonal elements of the matrix (where $i = j$) represent the variances of particular $R_{\mathrm{exp}\,i}$ values. The nondiagonal elements represent the interrelation between two of the values which can be due to the same experimental equipment and/or settings. For independent measurements all nondiagonal elements are zero.

The goal of the unfolding is to find such cross section vector $\boldsymbol{\sigma} = (\sigma_1, \ldots, \sigma_M)$ that the difference of the new calculated responses $\mathbf{R} = (R_1, \ldots, R_N)$ and the $\mathbf{R}_{\mathrm{exp}}$ be minimal

$$\chi^2 = (\mathbf{R} - \mathbf{R}_{\mathrm{exp}})^{\mathrm{T}}\, \mathbf{K}_{Rexp}^{-1}\, (\mathbf{R} - \mathbf{R}_{\mathrm{exp}}) = \min \quad \text{with} \quad \mathbf{R} = \boldsymbol{\Phi}\, \boldsymbol{\sigma}\ . \tag{5.6}$$

As the number of energy points M is higher than the number of measured responses N, an additional information is needed for a clear solution. This is accomplished by including the so called *guess*-function $\boldsymbol{\sigma'} = (\sigma'_1, \ldots, \sigma'_M)$ together with its covariance matrix $\mathbf{K}_\sigma$ that contains the *a-priori*-information of the excitation function searched for, usually being a combination of model calculations and existing experimental data. Considering this information, the χ^2 expression (5.6) then changes to

$$\chi^2 = (\mathbf{R} - \mathbf{R}_{\mathrm{exp}})^{\mathrm{T}}\, \mathbf{K}_{R\mathrm{exp}}^{-1}\, (\mathbf{R} - \mathbf{R}_{\mathrm{exp}}) + (\boldsymbol{\sigma} - \boldsymbol{\sigma'})^{\mathrm{T}}\, \mathbf{K}_\sigma^{-1}\, (\boldsymbol{\sigma} - \boldsymbol{\sigma'}) = \min\ . \tag{5.7}$$

This minimalization problem leads to explicit solution for $\boldsymbol{\sigma}$ [86]

$$\boldsymbol{\sigma} = \boldsymbol{\sigma'} - \mathbf{K}_\sigma\, \boldsymbol{\Phi}^{\mathrm{T}}\, \left(\mathbf{K}_{R\mathrm{exp}} + \boldsymbol{\Phi}\, \mathbf{K}_\sigma\, \boldsymbol{\Phi}^{\mathrm{T}}\right)^{-1}\, (\mathbf{R'} - \mathbf{R}_{\mathrm{exp}})\ , \tag{5.8}$$

where $\mathbf{R'} = \boldsymbol{\Phi}\, \boldsymbol{\sigma'}$.

This method allows to consider all available information of experiments with medium energy neutrons. The unfolding can be repeated and the results can be improved as soon as new information from new experiments is available. The feasibility of this method for the analysis of the thick target data has successfully been demonstrated [46, 87, 88].

5.2 Neutron activation experiments

Within the HINDAS project, neutron activation experiments were performed at TSL/Uppsala (The Svedberg Laboratory), Sweden and UCL/Louvain-la-Neuve (Université Catholique de Louvain), Belgium in order to determine excitation functions for the production of residual radionuclides from a variety of target elements up to 175 MeV. Most of these elements are interesting in cosmophysics as main targets for nuclide production in terrestrial and extraterrestrial matter (O, Al, Si, Fe, Ni, Te). Besides that, there are elements relevant for ADTW and ADEA (Pb, U) and medicine (C).

Irradiations are performed in stacked-foil-technique – all targets are irradiated together in a stack. Because of different moderation properties of the elements these are arranged with decreasing mass number along the beam direction. Copper foils are inserted at the beginning and at the end of the stack, as well as between each two pure element foils to allow for neutron flux monitoring in the stack.

Concentrations of radionuclides are determined using γ-spectrometry measurements performed right after the irradiations at TSL and UCL (for radionuclides with halflives up to about 5 hours like ^{11}C, ^{60}Cu or ^{198}Pb) and at ZSR (radionuclides with halflives up to few

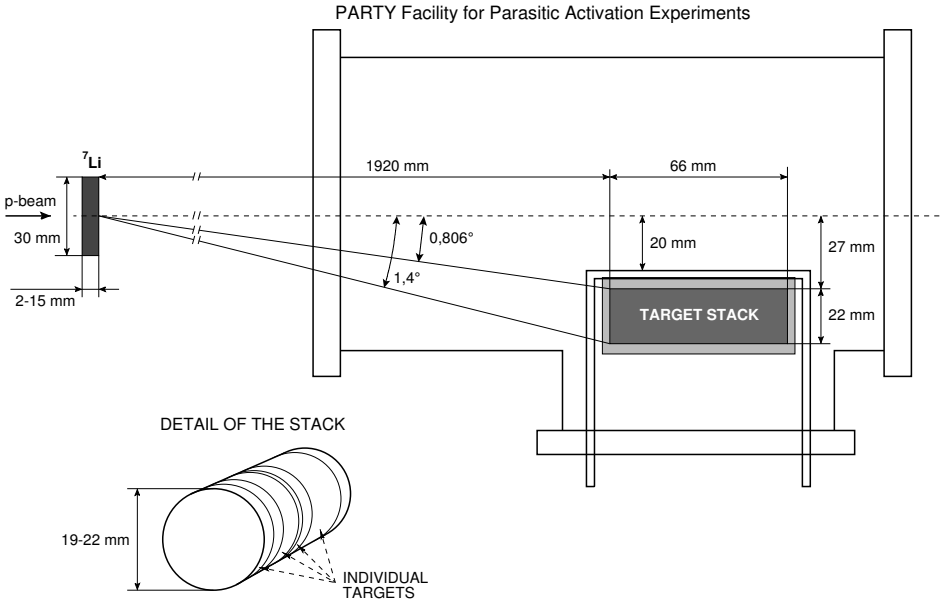

Figure 5.1: Schematic drawing of the irradiation chamber of the PARTY facility at TSL/Uppsala and its target stack (plot not to scale).

years like ^{7}Be, ^{22}Na, ^{60}Co or most of Pb and Bi isotopes) using HPGe and Ge(Li) detectors. Measurements for long-lived and stable nuclides (e.g. ^{21}Ne, ^{3}He) are performed using AMS at ETH/Zürich.

5.2.1 Irradiations at TSL/Uppsala

At TSL, the PARTY facility was set up at the neutron beam line close to the lithium target to allow for activation experiments with neutrons parasitically (PARasiTicallY) to other neutron experiments taking place 6–10 m further along the beam line [88, 89]. The parasitic mode of experiments was made possible by installing the irradiation chamber about 30 mm off beam axis (Fig. 5.1) leaving simultaneous experiments undisturbed. In the PARTY facility cylindrical target stacks (diameter 22 mm, lenght 66 mm) can be irradiated. The stacks can be loaded and unloaded by a pneumatic system during accelerator operation.

The neutrons are produced via the reaction $^{7}\mathrm{Li}(p,n)$ by irradiation of 2–15 mm enriched (99.984%) ^{7}Li targets with 25–180 MeV protons. Neutron flux densities of $\sim 0.5 \times 10^{5}$ cm^{-2} s^{-1} µA^{-1} (mm Li)$^{-1}$ are obtained in the high-energy peak of the neutron spectrum. Proton currents of 10 µA are available up to $E_p = 100$ MeV and about a factor of ten lower for energies between 100 and 180 MeV.

The fluence of neutrons passing the stack is monitored using $^{238}\mathrm{U}(n,f)$ and $^{209}\mathrm{Bi}(n,f)$ reactions as standards [90]. A pair of monitors with ^{238}U and/or ^{209}Bi targets is placed upstream and downstream the stack. Each monitor consists of a fissile target and a thin film breakdown counter (TFBC) used for fission fragment detection.

The monitors operate in a time-of-flight (TOF) mode. However, the short flight path

Table 5.1: Basic information about the irradiations performed at TSL/Uppsala. The neutrons were produced by protons of energy $E_p \pm \Delta E_p$ on a d thick Li target, E_n is mean energy of neutrons in peak.

Irradiation	uppn09	uppn0b	uppn0e	uppn0f	uppn0h	uppn0k	uppn0l	uppn0m
Date	03/97	05/97	01/98	06/98	09/98	09/98	10/98	05/99
E_p [MeV]	97.5	162.7	98.5	98.6	49.19	69.19	96.8	136.7
ΔE_p [MeV]	0.3	1.0	0.3	0.3	0.1	0.2	0.3	1.0
E_n [MeV]	94.5	159.3	96.1	96.2	46.2	66.4	94.4	133.0
d(Li) [mm]	8	15	4	4	4	4	4	15
Irradiation	uppn0n	uppn0o	uppn0p	uppn0q	uppn0r	uppn0s	uppn0t	uppn0u
Date	11/99	12/99	05/00	10/00	02/01	06/01	09/01	02/02
E_p [MeV]	97.9	76.4	178.8	148.4	68.1	137.4	177.3	98.1
ΔE_p [MeV]	1.0	0.2	0.8	0.6	0.2	1.0	1.0	0.3
E_n [MeV]	95.6	73.8	175.5	144.8	65.5	133.8	174.0	95.7
d(Li) [mm]	4	4	15	15	4	15	15	4

(about 2 m) and unfavorable time structure of the beam does not allow an explicit neutron spectrum recognition. At present the quantitative characterization of the neutron field in the irradiation facility is limited to the measurement of high-energy peak neutron fluence [91].

In this work, transport calculations for 16 TSL activation experiments were performed. The individual TSL irradiations were given names starting with *uppn0* followed by a digit or letter increasing with the date when the irradiation was performed. So, for example, the irradiation in May 1999 with proton energy $E_p = 137.7 \pm 1.0$ MeV was assigned the name *uppn0m*. The names together with other basic information about all TSL irradiations evaluated in these work are listed in Tab. 5.1. More detailed description can be found in Appendix C.

5.2.2 Irradiations at UCL/Louvain-la-Neuve

The UCL facility enables the production of quasi-monoenergetic neutron beams [92]. Metallic lithium with natural isotopic composition is used for neutron production. Possible proton currents are up to 10 µA, resulting in flux densities in the high-energy peak of neutron spectrum of about 10^5 cm^{-2} s^{-1} at 5 m distance from the target.

The stack with irradiation foils (25 mm diameter) is positioned at distances from the target of about 5 m and is unlike TSL PARTY facility installed on the beam axis. As FWHM of the beam at that position is higher than stack diameter (about 55 mm), during test irradiations considerable inhomogenities in beam profile were observed in other simultaneous experiments occuring further along the beam line. Therefore, larger foils (100 × 100 mm) have been installed in later irradiations to ensure equal absorption across the whole beam profile (Fig. 5.2).

At the position of the stack the neutron fluence in high-energy peak is determined with

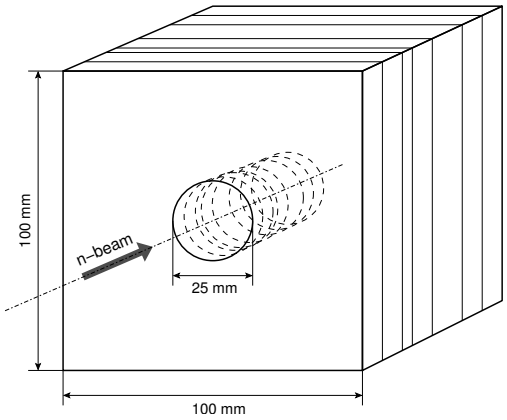

Figure 5.2: Sketch of the target stack for the UCL/Lovain-la-Neuve irradiations.

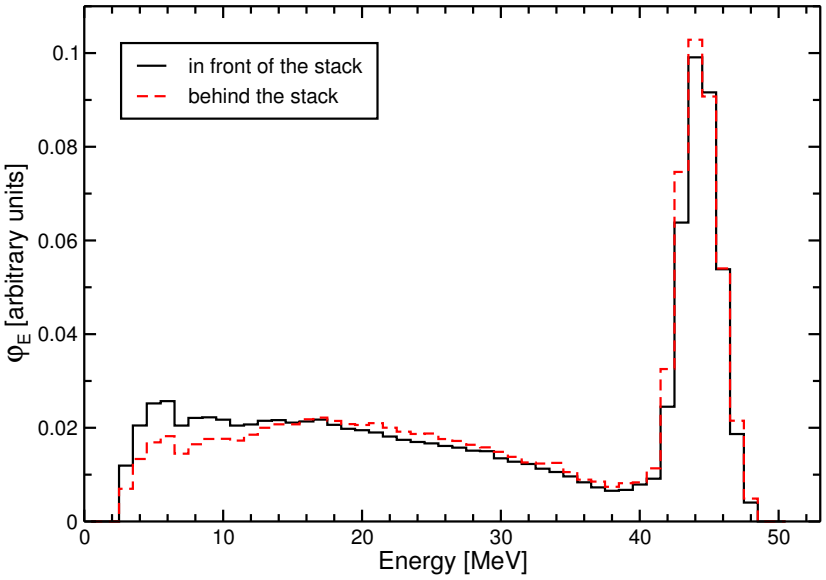

Figure 5.3: Relative spectral neutron fluence entering and leaving the stack for 04/98 UCL/Lovain-la-Neuve irradiation with nominal neutron energy 45 MeV. Both spectra are normalized to the same area.

proton recoil telescope (PRT) [93, 94]. The energy distributions of neutrons entering and leaving the stack are determined by TOF spectrometry at distances of about 11 m from the target without and with the stack in its irradiation position. For neutron peak energies below 50 MeV a liquid scintillation detector (NE213) and for higher energies a ^{238}U fission ionisation chamber were used as spectrometers [95].

Starting 1997, six irradiations with nominal neutron energies 33 MeV, 45 MeV and 60 MeV were performed at UCL in collaboration with PTB/Braunschweig, Germany (Physikalisch-Technische Bundesanstalt). As an example, Fig. 5.3 shows the measured energy distributions for the 45 MeV run without and with the stack. Since the two spectra were normalised to the same area, the differences in shape caused by the energy dependent fluence attenuation, can be clearly observed.

Table 5.2: Basic information about the UCL/Lovain-la-Neuve irradiations. The neutrons were produced by protons of energy E_p on a 5 mm thick Li target, E_n is mean energy of neutrons in peak.

Irradiation	louv02	louv03	louv04	louv05	louv06	louv07
Date	10/97	04/98	11/98	12/00	05/01	11/01
E_p [MeV]	36.4	48.5	62.9	48.5	62.9	36.4
E_n [MeV]	32.9	45.4	60.1	45.3	60.0	32.8
d(Li) [mm]	5	5	5	5	5	5

In analogy to TSL irradiations, the UCL irradiations were given names starting with *louv0* followed by a digit or a letter (e.g. *louv04* for the irradiation performed in November 1998 with proton energy $E_p = 62.9$ MeV). Information about UCL activation experiments can be found in Tab. 5.2, and in Appendix C.

5.3 Construction of quasi-monoenergetic neutron spectrum for TSL irradiations

While for the neutron transport calculations inside the stack the primary quasi-monoenergetic neutron spectrum has to be known, it cannot always be measured. This is the case for all TSL irradiations. In this work we use a semi-empirical method for the neutron spectrum construction which was used in [88]. This method is described below and the results are compared with the results obtained using the Monte Carlo simulation of the neutron production.

Neutron spectrum from ^{7}Li(p,n) reaction has two components – mono-energetic high-energy-peak component with energy right below the proton energy and the continuum at lower energies (Fig. 5.3).

5.3.1 Peak component from reaction ^{7}Li$(p,n)^7$Be

Monoenergetic neutrons are produced in the ^{7}Li$(p,n)^7$Be reaction leaving Be nucleus in the ground, first excited or second excited state

$$\begin{aligned} {}^7\mathrm{Li} + p &\longrightarrow {}^7\mathrm{Be} + n \qquad (Q = -1.646 \text{ MeV}) \\ &\longrightarrow {}^7\mathrm{Be}^* + n \qquad (Q = -2.075 \text{ MeV}) \\ &\longrightarrow {}^7\mathrm{Be}^{**} + n \qquad (Q = -6.216 \text{ MeV}) \end{aligned} \tag{5.9}$$

that is, monoenergetic neutrons of three different energies are produced. For considered incident proton energies E_p, in nonrelativistic mechanics one can calculate the energy E_n of neutrons emitted at angle ϑ given the Q-value of the reaction as

$$\begin{aligned} &E_n = \alpha + \beta + \sqrt{\alpha^2 + 2\alpha\beta} \quad \text{with} \\ &\alpha = \frac{2 m_p m_n E_p \cos^2\vartheta}{(m_n + m_{^7\mathrm{Be}})^2}\,, \quad \beta = \frac{m_{^7\mathrm{Be}} Q + E_p (m_{^7\mathrm{Be}} - m_p)}{m_n + m_{^7\mathrm{Be}}}\,, \end{aligned} \tag{5.10}$$

where m_p, m_n and $m_{^7\mathrm{Be}}$ are masses of proton, neutron and ^{7}Be nucleus respectively [e.g 96].

Only the monoenergetic components of the reaction to the ground state and first excited state of the residual ^{7}Be nucleus contribute together to the peak. According to [97, 98], the ratio of both contributions in the peak is $n_1/n_0 = 0.3$ for proton energies up to 50 MeV. For higher energies no data exist. However, the influence of the value of this ratio is very small. Taking into account only the reaction to the ground state would shift the mean peak energy of neutrons only ≈ 0.1 MeV higher. Increasing the ratio to 1.0 shifts the mean energy about the same value lower.

The spectrum component from the reaction to the second excited state occurs at energies approximately 6 MeV below the peak energy window and as such can make an addition to the continuum component. As its contribution cannot be determined from experimental neutron spectra it is not considered in further calculations.

Considering gaussian energy distribution of protons in the incident beam with uncertainty ΔE, their energy losses in the lithium target E_{loss} and using (5.10), the spectral flux density of the peak neutrons $\varphi_{n_{\mathrm{Peak}}}(E)$ is calculated as

$$\varphi_{n_{\mathrm{Peak}}}(E) \propto \int_{E_p - E_{\mathrm{loss}}}^{E_p} \mathrm{d}E_i \int_{E_i - 5\,\Delta E}^{E_i + 5\,\Delta E} e^{-\frac{(E_i - E')^2}{2\,\Delta E^2}}\, \delta(E - E_n(E'))\, \mathrm{d}E' \,. \tag{5.11}$$

The proton energy losses are calculated for each E_p – ΔE – Li target thickness combination according to Andersen-Ziegler parametrization of Bethe-Bloch formula [99].

In the calculation the energy straggling of protons in the Li target was not considered. This process causes enlarging of the proton energy uncertainity which reaches at the end of the target 20–50% depending on the proton beam energy and the thickness of the target.

From the comparison of calculated and measured neutron peaks (Fig. 5.4) it can be seen that in all cases the calculated peaks are slightly narrower and shifted to higher enegies. This is in agreement with the approximations mentioned above. The discrepancy is only very small and there is a good overall agreement.

5.3.2 Continuum component

The following model has been succesfully used to describe continuum component of $^7\mathrm{Li}(p,n)$ reaction in works of various authors [88, 100–103].

The continuum component of quasi-monoenergetic neutron spectrum consists of neutrons produced in channels of $^7\mathrm{Li}(p,n)$ reaction concurent to (5.9) reaction. These are the pree-quilibrium reactions and the evaporation reactions. For light target nuclei ($A \lesssim 12$) the later are replaced by Fermi break-up reactions.

To retain simplicity of the model, two three body break-up reactions are considered

$$^7\mathrm{Li} + p \longrightarrow {}^8\mathrm{Be}^* \longrightarrow {}^4\mathrm{He} + {}^3\mathrm{He} + n \qquad (Q = -3.23\ \mathrm{MeV}) \tag{5.12}$$

$$\longrightarrow {}^6\mathrm{Li} + p + n \qquad (Q = -7.25\ \mathrm{MeV}) \tag{5.13}$$

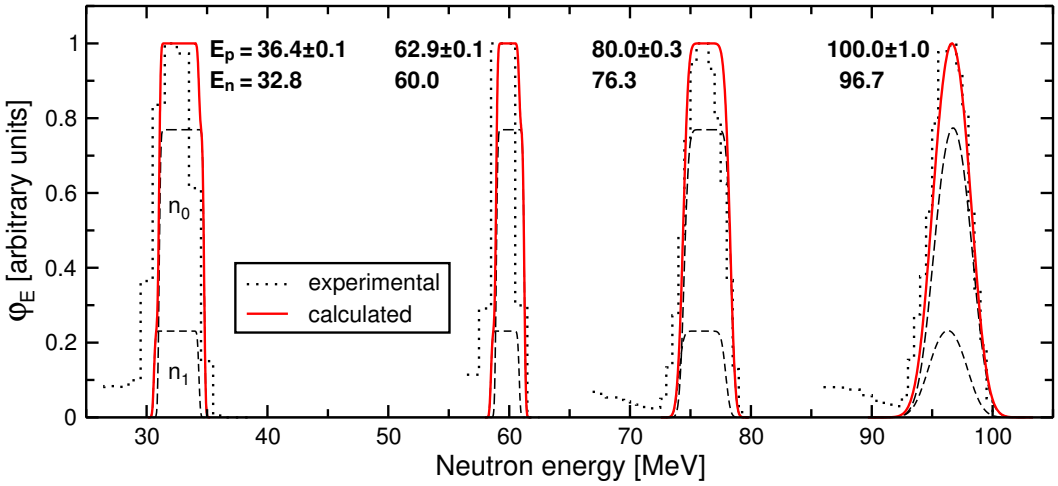

Figure 5.4: Calculated neutron peak spectral flux densities according to (5.11) for *louv02* and *louv04* irradiations with 5 mm Li targets (two peaks on the left) and for two irradiations with 10 mm targets from [100] considering reaction (5.9) to the ground state (n_0) and the first excited state (n_1) of ^{7}Be nucleus. Given are the proton energies E_p and the mean peak neutron energies E_n. Spectra are scaled so that the maximum value is 1.0.

Given the energy of incident proton beam E_p, it was shown [88] that the energy distribution of neutrons emitted at angle ϑ produced in such reactions can be good described using a phase space function [104]

$$\varrho_n(E) \propto \sqrt{E_n \left(\frac{m_2 + m_3}{m_n + m_2 + m_3} E_t^c - E_n + 2a \cos\vartheta \sqrt{E_n} - a^2 \right)} \quad \text{with}$$
$$E_t^c = Q + \frac{m_{^7\mathrm{Li}}}{m_p + m_{^7\mathrm{Li}}} E_p \,, \quad a = \frac{\sqrt{m_n m_p E_p}}{m_p + m_{^7\mathrm{Li}}} \,, \tag{5.14}$$

where m_p, m_n and $m_{^7\mathrm{Li}}$ are masses of proton, neutron and ^{7}Li nucleus respectively and m_2 and m_3 are the masses of the two other fragments from (5.12) or (5.13) reaction.

The final shape of the continuum can be calculated summing the contributions from both reactions. Assuming their equal contribution, the final calculated continuum is shown on Fig. 5.5. The difference between the final continuum and continuum of only (5.12) is less than 5% for energies up to ≈15 MeV below the peak energy window. Right below the peak this difference increases to 40% but decreases with increasing incident proton energy. For E_p values above 100 MeV it is less than 20%.

According to [105], the probability of three body break-up is proportional to the square of total kinetic energy of fragments at the moment of break-up which subsequently leads to higher probabilities for reactions with higher Q-values. Therefore the contribution of (5.12) should be higher in the final continuum than that of (5.13). Taking this into account further reduces the difference between the (5.12) reaction and the sum of both reactions and therefore only this reaction is considered in continuum component calculations.

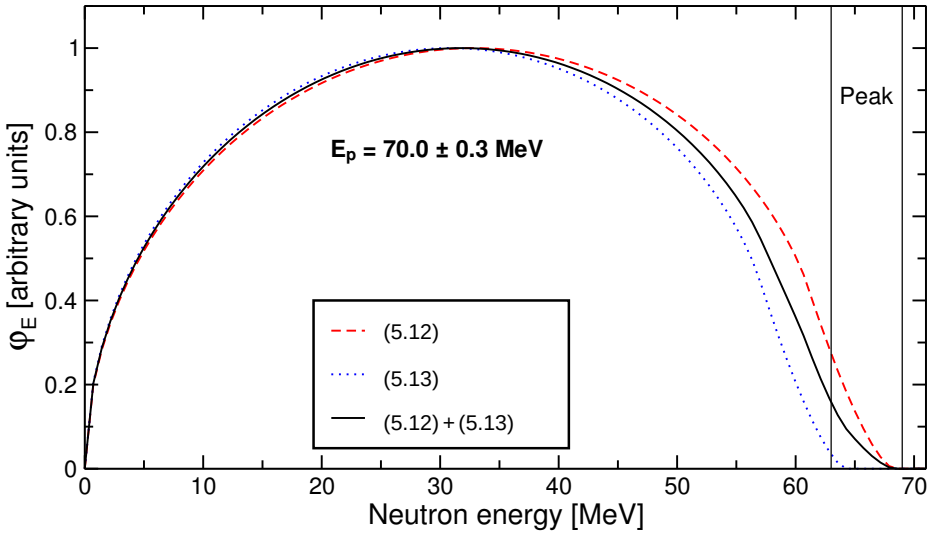

Figure 5.5: Calculated spectral flux density of the continuum component according to (5.14) for incident proton energy $E_p = 70.0 \pm 0.3$ MeV. Spectra are scaled so that the maximum value is 1.0.

5.3.3 The whole neutron spectrum

Calculated monoenergetic and continuum parts are merged into the single quasi-monoenergetic neutron spectrum based on a comparison with peak and continuum flux densities from measured neutron spectra. For this purpose 17 experimental neutron spectra were used from works [100–102] together with spectra from 6 UCL irradiations (Tab. 5.2).

Fig. 5.6 shows ratio of flux density in the peak to the flux density in the whole neutron spectrum above 20 MeV $\phi_{\mathrm{Peak}}/\phi(E_n \geq 20\ \mathrm{MeV})$ for measured spectra. The lower energy limit of 20 MeV makes it possible to consider also spectra for which flux density data below this energy are not available. For incident proton energies above 50 MeV the ratio has the value of 0.44. This value was determined averaging the data within the box. Below $E_p = 50$ MeV a major part of the continuum components is below the 20 MeV limit and the ratio sharply increases.

Using the mean ratio value, the calculation of the whole quasi-monoenergetic spectra for all available measured spectra was made to test the model. The comparison for eight proton energies is shown on Fig. 5.7. The calculated spectra for $E_p = 58$, 62.9 and 70 MeV are in good agreement with the measured ones. This agreement holds for all proton energies from 50 MeV to $\approx$ 90 MeV.

Below 50 MeV we have used ratio value corresponding to the particular measured spectrum to make comparison. As can be seen for $E_p = 48.5$ MeV (ratio 0.59), the continuum of the measured spectrum unlike the theoretical one slowly grows when going to lower energies. This is probably due to increased contribution from reaction channels with higher Q-values for lower proton energies.

On the contrary, the continua for E_p above 90 MeV are leaned towards higher energies.

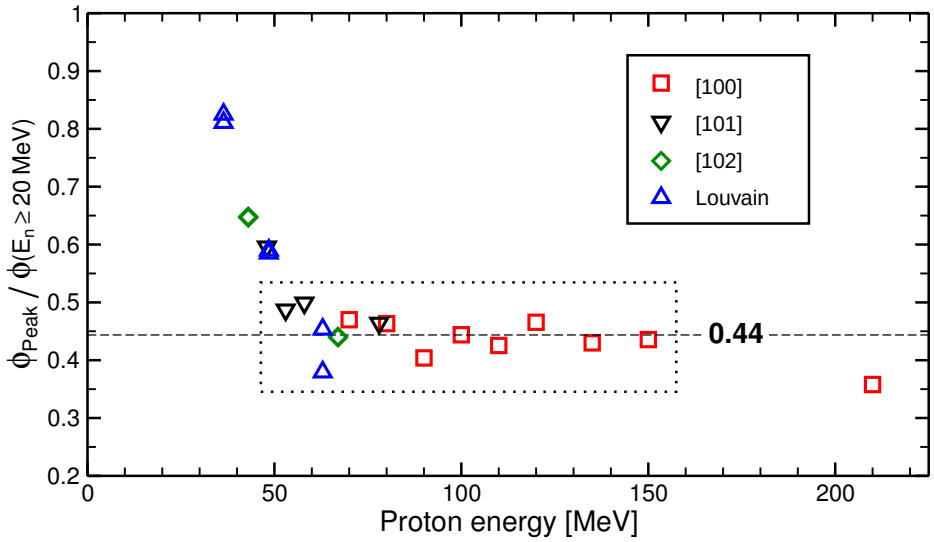

Figure 5.6: Ratio of flux density in the peak to the flux density in the entire neutron spectrum above 20 MeV for measured quasi-monoenergetic spectra. The mean ratio value was determined averaging data within the box.

The reason for that is the increasing importance of preequilibrium reaction channels which result in high-energy neutrons being emitted at forward directions. Most of TSL irradiations have proton energies in this region and therefore a simple adjustment method was used to fit calculated continua to the experimental ones. This consists in multiplying the phase space function (5.14) by an increasing linear function

$$\varphi_{n_{\mathrm{Cont}}}(E_n) \propto \varrho_n(E)\,[1 - A(E_p)\,(E_{\max} - E_n)] \quad \text{with} \quad A(E_p) > 0\,, \tag{5.15}$$

where $E_{\max}$ is the maximum neutron energy in the continuum and A is a parameter determining the slope. For each incident proton energy (above 90 MeV) this parameter is determined separately to fit the measured spectrum. Adjusted spectra are shown on Fig. 5.6 together with non-adjusted for proton energies 100 MeV and 150 MeV with values of A equal to 7.5×10^{-3} and 5.3×10^{-3} respectively.

5.3.4 The LCS calculation of quasi-monoenergetic neutron spectrum

The LAHET code included in the LCS contains both Fermi break-up and preequilibrium nuclear reaction models, but it does not contain any reaction specific data[1]. Therefore, the peak parts of the neutron spectra should be described better by the semi-empirical model mentioned above and the continuum parts by the LCS calculations.

To verify this assumption we calculated the spectra of neutrons produced in ^{7}Li(p,n) reaction for incident proton energies 48.5 MeV, 62.9 MeV and 150 MeV. The irradiations were simulated as an interaction of monoenergetic "pencil" proton beam with the lithium

[1] See section 3.1.1 for the description of the LCS.

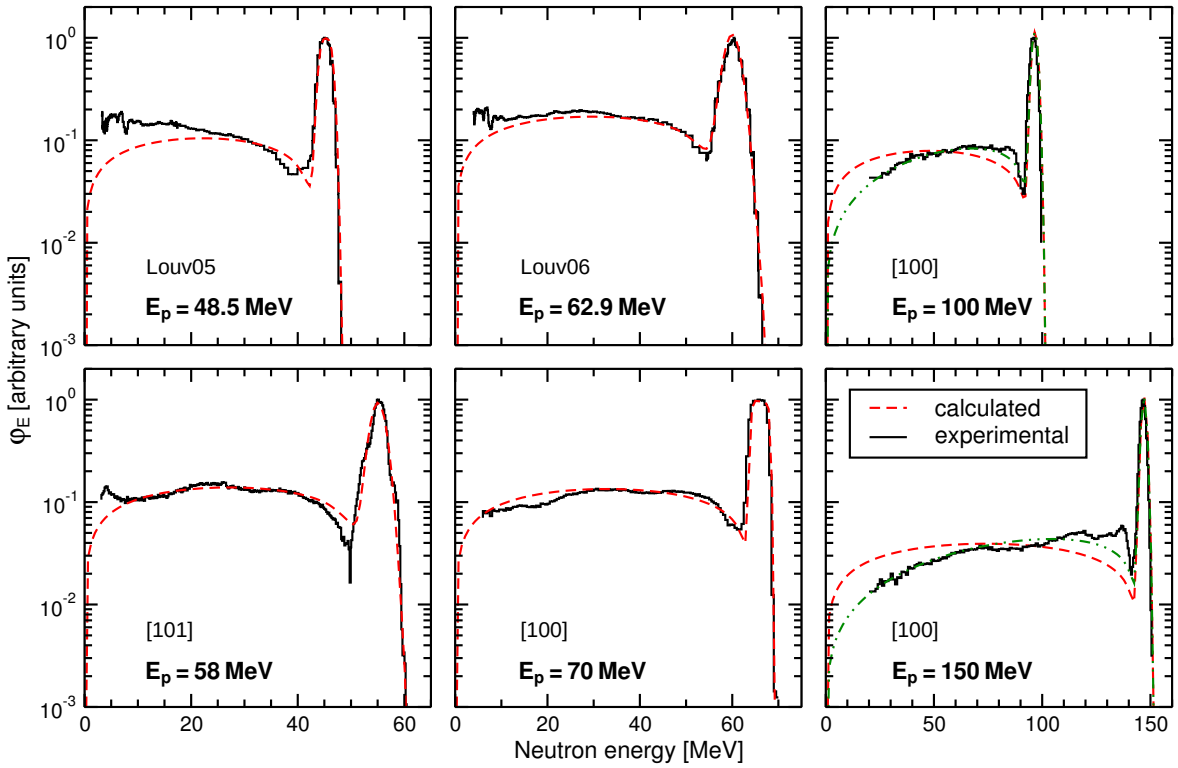

Figure 5.7: Comparison of calculated quasi-monoenergetic neutron spectra with the measured ones for six selected incident proton energies. For $E_p = 48.5$ MeV ratio value 0.59 was used, for all other energies value 0.44 was used. For energies 100 MeV and 150 MeV also the theoretical spectra adjusted according to (5.15) are shown (dash-dotted line).

target with thickness 5 mm for the two lower energies and 10 mm for the high energy. The output from the calculations was the neutron flux density at forward direction.

The LCS calculated spectra are unsatisfactory not only for the peak parts, where this behaviour was expected, but also for the continuum parts (Fig. 5.8). Compared to the measured spectra, the calculated continua show monotonous decrease with increasing energy in all three cases. The lower neutron fluxes for energies above $\approx$ 20 MeV are due to unsatisfactory description of pre-equilibrium neutron emission in LAHET, which was also observed in [106, 107]. Higher calculated neutron fluxes below 20 MeV are due to broader space angle considered in the calculation than in the real measurements. This calculation setup was chosen to improve the statistics.

These results show that agreement of calculations using semi-empirical model with measured spectra is much better than for LCS calculations for all energies.

5.4 The setup of the neutron transport calculations

When target material is irradiated with neutrons produced in Li target, various nuclear reactions take place on the target nuclei. In this reactions residual nuclides are produced,

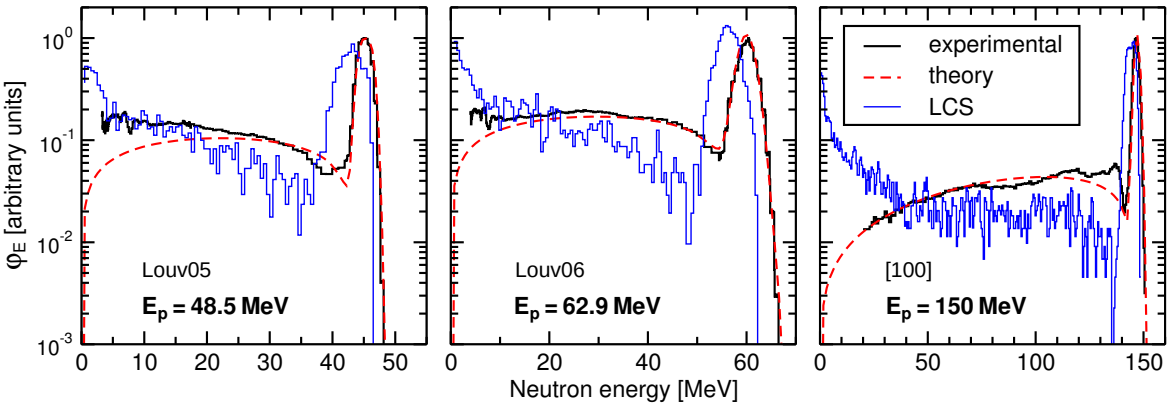

Figure 5.8: Comparison of LCS calculated and measured neutron spectra together with the ones calculated using semi-empirical model.

but also secondary particles like neutrons, protons or complex particles like α-particles. The primary neutron inducing such reaction is excluded from the primary neutron beam and consequently the neutron fluence at the position in the target is decreasing. The neutron flux is also modified in elastic and inelastic scattering of neutrons that leads to neutron moderation in the stack. Thes interactions of neutron beam with the target stack are calculated for each irradiation using Monte-Carlo codes included in the LCS[2].

For the complete setup of the calculations the selection of the incident neutron spectra, the geometrical description of the simulated irradiation and the selection of nuclear models used are necessary.

For the UCL irradiations always the measured neutron spectra in front of the stack were used as input. These were not available for the TSL irradiations so according to the comparison of semi-empirical and LCS calculated spectra (Fig. 5.8) we chose the former in all cases. For incident proton energies above 90 MeV the spectra were adjusted according to (5.15) with the parameter A found from the measured spectrum with the closest proton energy available. The values of parameter A used for particular irradiations can be found in Tab. C.2.

The geometry in the calculations was set up according to Fig. 5.1 and 5.2 for the TSL and UCL irradiations respectively. For UCL, this means that the irradiation of square-shaped foils with thicknesses corresponding to individual experiments was simulated, whereby the neutron fluxes were only calculated in the small circle-shaped pieces in the middle of each foil. The isotopic composition and bulk densities used were those given by the manufacturers of the particular foils.

In the experiments, for small circular foils of some (expensive) materials other materials have been used as the complementary square parts with thickness corresponding to the same neutron absorption as for the cilcular foil. This has also resulted in different total lenghts of central (round) and outer (square) parts of the stack. In the simulation the stack was

[2]See section 3.1.1 for the description of the LCS.

modelled to consist of foils made entirely of the particular material with constant thickness. The neutron beam was simulated to have common axis with the stack and with neutrons uniformly distributed over a circle with diameter 5 cm.

For the TSL irradiations, the stack model in the simulations corresponds to the real stack. It consisted of circular foils held in the aluminium shuttle with wall thickness of 4 mm and total lenght of 70 mm. The foils were placed right at the beginning of the shuttle.

In the irradiations, the shuttle was not positioned at the beam axis so it was irradiated by neutrons emitted from the Li target at the mean angle $\approx 1^\circ$ to the beam axis (Fig. 5.1). This was simplified in the calculations. The primary neutron spectrum emitted from the Li target at 1° was calculated and then used as an energy distribution of the parallel beam with diameter greater than the diameter of the shuttle.

In the calculations, both the TSL and UCL stacks were surrounded with vacuum and the contribution to transport from surrounding materials and devices like beam tubes, construction or detectors was not taken into account.

For the transport calculations, LAHET was set up to use the intranuclear cascade model followed by the preequilibrium model and the nuclear evaporation. For light nuclei ($A \geq 13$ and $14 \geq A \geq 20$ with excitation energy below 44 MeV) the Fermi break-up model was used instead of evaporation. For elastic scattering the data included in LAHET (file ELSTIN) were used.

With LAHET, only neutrons with energies $E_n > 20$ MeV were transported. All neutrons below this energy were recorded for subsequent transport using the MCNP. For all foils, the continuous-energy cross section libraries from ENDF/B-V included in the MCNP installation were used, when they were available. This was not the case for tellurium ($Z = 52$, $\bar{A} = 127.7$) for which the iodine ($Z = 53$, $A = 127$) libraries were used instead.

For each irradiation the neutron counts in 155 energy bins per one primary neutron was calculated in each foil. The energy bins had width 1 MeV below 130 MeV and 2 MeV above this energy up to 180 MeV. This energy range covers all the experiments considered. The number 155 was given by the limitations of the STAY'SL code used for the cross section unfolding for which the calculated neutron flux was an input.

Individual experiments were simulated with an irradiation of 7×10^6 neutrons. This resulted in uncernainties of the flux in each energy bin below 5%.

Examples of input files for the neutron transport calculations using LCS can be found in Appendix A.

5.5 Results and discussion

Energy dependence of the flux of neutrons passing through the target stack is modified due to the nuclear and subnuclear processes depending on the position of the foil in the stack. It also depends on the parameters that have an influence on these processes and are specific for

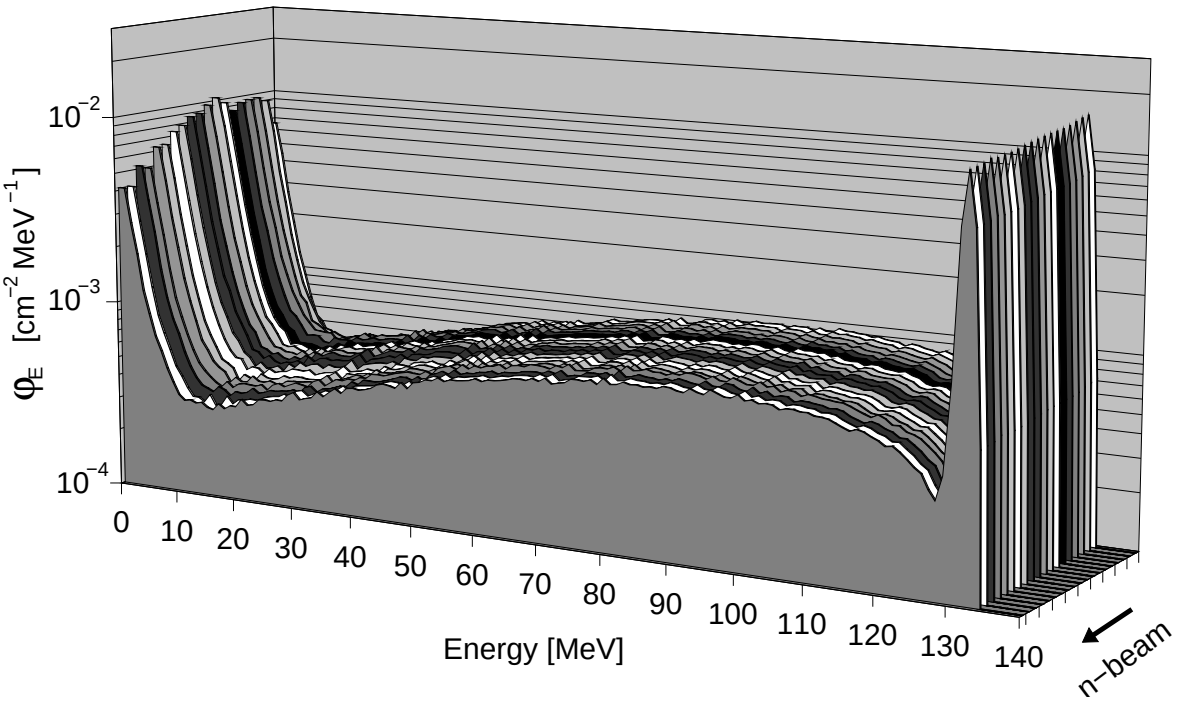

Figure 5.9: The calculated differential neutron flux densities in all foils of the TSL irradiation *uppn0m* normalised per 1 primary neutron.

the particular foil material.

The differential neutron flux densities in all foils calculated for the TSL irradiation *uppn0m* are shown on Fig. 5.9. The spectra look very similar for all irradiation experiments with differences mainly due to different input spectra. Here the simulation results only for the *uppn0m* irradiation are analyzed. Presenting the results also for all 21 remaining irradiations would not add any important information to the analysis.

In the following, the development of the spectral shape in particular energy ranges is discussed. Then the calculated neutron spectra behind the stack at the spectrometer position in the UCL irradiations are compared to the measured ones to verify the aptitude of the simulations. Subsequently, the discussion of uncertainties and their influence on the final cross sections is made. Finally, some preliminary results of the evaluated cross sections for the reactions $^{\mathrm{nat}}\mathrm{Pb}(n, 2pXn)^{203}\mathrm{Hg}$ and $^{\mathrm{nat}}\mathrm{Cu}(n, 2pXn)^{56}\mathrm{Co}$ are presented.

5.5.1 Primary and secondary neutrons

From Fig. 5.9 two main characteristics of the spectrum development can be seen. First is the appearence of high numbers of low-energy neutrons ($E_n < 10$ MeV) with a maximum occuring at a position ≈ 2 cm from the beginning of the stack. Second is the overall decrease of the neutron flux along the stack.

Both these characteristics can be seen more clearly on Fig. 5.10 (left). Here the profile of the neutron flux for the *uppn0m* irradiation integrated over the whole spectrum ϕ_{total} is shown

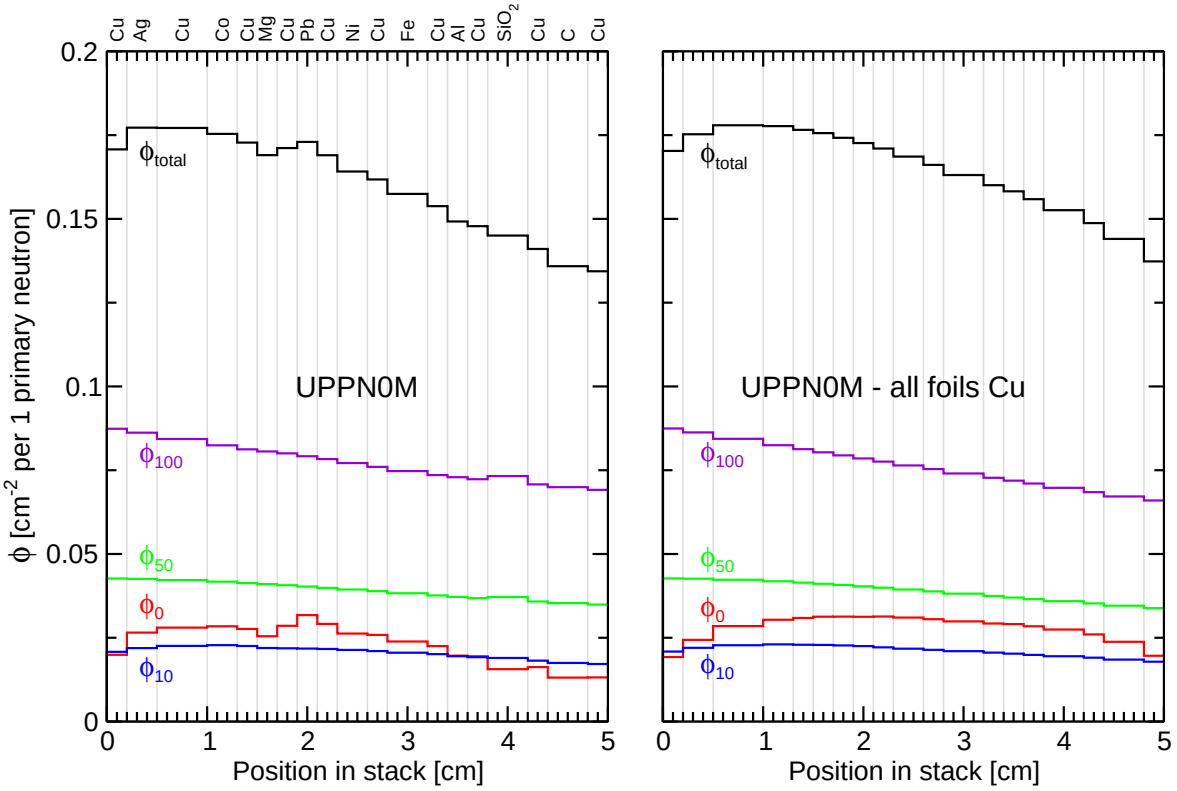

Figure 5.10: The calculated neutron flux integrated over the whole energy interval ϕ_{total} and four subintervals $\phi_0(E_n < 10$ MeV), $\phi_{10}(10 < E_n < 50$ MeV), $\phi_{50}(50 < E_n < 100$ MeV) and $\phi_{100}(E_n > 100$ MeV) as functions of the position in the stack for the real *uppn0m* irradiation (left) and for the irradiation of a virtual stack of the same lenght made entirely of copper.

together with those integrated over four energy subintervals. These are ϕ_0 ($E_n < 10$ MeV), ϕ_{10} ($10 < E_n < 50$ MeV), ϕ_{50} ($50 < E_n < 100$ MeV) and ϕ_{100} ($E_n > 100$ MeV).

High flux of neutrons with energies below 10 MeV (ϕ_0) that were absent in the primary spectrum can be assigned to the moderation of neutrons with higher energies in the stack material but mainly to the production of low-energy secondary neutrons in nuclear reactions that proceed through compound nucleus. In these reactions neutrons are emitted isotropically in the rest frame of the compound nucleus. This also explains high values of ϕ_0 occuring already in the first foil of the stack because neutrons produced in the next foils and in the surrounding material are also emitted in backward directions and eventually enter the first foil and contribute to the total flux in that foil.

As already mentioned, neutrons of all energies are moderated and can be absorbed while passing through the stack material. The absorption process and the production of secondary neutrons define the shapes of profiles in Fig. 5.10 (left) for all energy intervals.

Because of the cascade development, the production of secondary neutrons outbalances their absorption at the begining of the stack and the secondary neutron fluxes are increasing. At some position the equilibrium between production and absorption occures and then the

fluxes are decreasing down to the end of the stack. At the same time the absorption of primary neutrons monotonously decreases their fluxes along the stack. The final shape of the ϕ profile for the particular energy range is a combination of the primary and secondary neutron profiles for that range.

For energies above 100 MeV there are only a few secondary neutrons produced during transport with such high energies and they are negligible in comparison to the number of primary neutrons. The absorption plays primary role in this energy region which is reflected in 20.9% decrease of ϕ_{100} fluence. The situation is similar for energies $50 < E_n < 100$ MeV. Even if the production of secondary neutrons with energies in this interval is higher than in the above interval it is still far lower than the absorption and the ϕ_{50} has the total decrease of fluence of about 18.2%.

Apparently different are the shapes of the two low-energetic fluences ϕ_{10} and ϕ_0. In both cases the fluence first increases which is a result of rapid increase of fluences of low-energy neutrons. The relative increase of fluence ϕ_{10} is 9.5% and the maximum occurs at $\approx$ 1 cm from the beginning of the stack. For ϕ_0 the maximum occurs at $\approx$ 2 cm and the relative increase is 59.6%. This indicates that most secondary neutrons have energies below 10 MeV. These neutrons are continually absorbed and because most of them have nonforward directions they can also escape from the stack before reaching its end. At the position of the fluence maximum these two processes are in equilibrium with the production of secondary neutrons and outbalance it further in the stack so that both ϕ_{10} and ϕ_0 decrease. Total and local (the maximum to the end of the stack) decrease of the ϕ_{10} fluence is 17.4% and 24.7% respectively. For ϕ_0 these values are 33.9% of total decrease and 58.6% of local decrease.

As the ϕ_{total} fluence integrated over the whole energy interval represents the sum of the ϕ_0, ϕ_{10}, ϕ_{50} and ϕ_{100} fluences, it also combines in itself all their features: increase of 3.8% at the beginning of the stack with maximum at about 0.5 cm and then local decrease of 24.2%. From this it is apparent, that the primary effect of the presence of the stack in the neutron beam trajectory is the decrease of the total neutron fluence (in the case of *uppn0m* it is 21.3%).

The profiles calculated for the *uppn0m* irradiation with the stack composition corresponding to the irradiated one are not smooth (Fig. 5.10 left). Largest odds occure in ϕ_0 profile and can also be seen in ϕ_{total} after summing all fluences. We have investigated this feature of the profiles by replacing all foil materials with copper in the calculation. Fluence profiles for such stack are shown on Fig. 5.10 right. They are smooth, not disturbed by any odds and have the same basic shape as the profiles for the real *uppn0m* stack. Therefore, we can conclude that the deviations from the smooth shape in the case of the real stack are caused by differences in scattering, moderation, absorption and nuclear weights of individual foil materials.

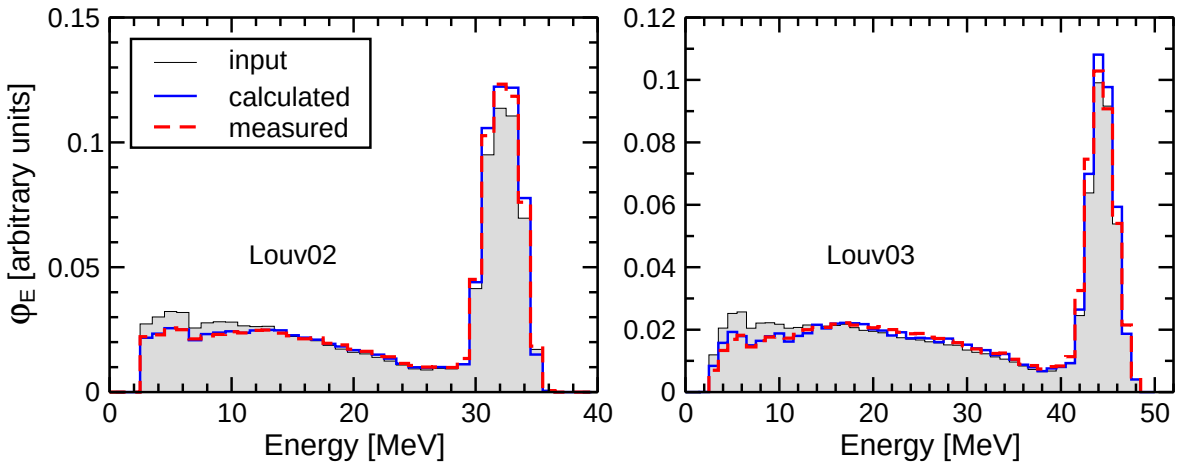

Figure 5.11: The comparison of the measured and calculated neutron spectra behind the stack for the *louv02* and *louv03* irradiations. To indicate the effects the stack has on the neutron spectra, also the primary input spectra are shown. All spectra are normalized to one.

5.5.2 Neutron spectra behind the stack

Besides the input spectra, for all Louvain irradiation experiments also the spectra of neutrons in the beam measured after the pass through the stack are available. This fact enabled us to verify the accuracy of the transport calculations.

The comparison of measured and calculated neutron spectra behind the stack for the *louv02* and *louv03* irradiations is shown on Fig. 5.11. In both cases, the spectra were calculated at the distance from the stack where the spectrometer was positioned (5.207 and 5.257 meters for *louv02* and *louv03* irradiations respectively) taking its active volume into account. The agreement is very good. The relative discrepancy of calculated and measured fluence in peak for the two presented irradiations is 0.3% for *louv02* (peak threshold 29 MeV) and 0.22% for *louv03* (peak threshold 40 MeV) respectively.

Fig. 5.11 also indicates the effects the presence of the stack has on the energy distribution of neutrons. In both cases the relative distribution changed in favour of high energies after the neutrons passed the stack. This is due to rapidly increasing neutron capture cross sections when going to low energies. Another reason for that is, as mentioned above, that the majority of low-energy neutrons have nonforward directions. For *louv02* and *louv03* irradiations only those neutrons are detected that have directions within the angle $\approx 0.28°$ to the beam axis.

5.5.3 Estimate of errors

There are several factors influencing the accuracy of the final calculated neutron spectra in each foil for each particular irradiation experiment.

First of all it's the accuracy of input parameters in the calculations. For the UCL irradiations these are the input neutron spectra measured by PTB using NE213 scintillation

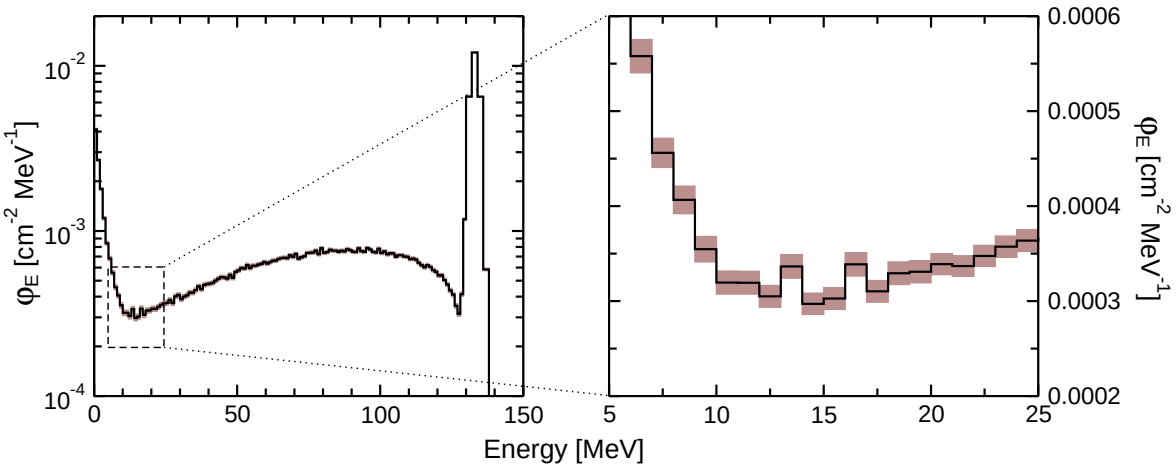

Figure 5.12: Neutron spectrum in the last but one foil (carbon) of the *uppn0m* irradiation with the statistical uncertainties of the Monte Carlo calculation also shown.

spectrometer with relative uncertainty ranging from 5.9% at 34 MeV to 7.4% at 61 MeV [95].

For the TSL irradiations this involves the accuracy of the theoretical neutron spectra calculated using the semi-empirical model. As this model is a combination of theoretical calculations with the parameters determined from experimental data, best way to estimate the uncertainty of the resulting spectra is the comparison with measured spectra. The height and width of the peak depend very much on a selected spectrometric method [e.g. 95]. Therefore, we compared only the continuum parts of the spectra. The relative root-mean-square deviation here was from 7% to 15% for spectra from [100, 101]. At lowest energies and at energies right below the peak the deviation is higher (10-20%). Middle part of the continua have the deviation about 5-10%.

Due to neglected energy straggling of protons in Li target as well as due to the nonexistence of experimental data for the ratio of contributions of the reaction (5.9) to the ground state and to the first excited state of ^{7}Be nucleus above 50 MeV, the energetic resolution of the peak energy becomes worse. We estimate the addition of 0.5 MeV to the energy error.

In addition to the uncertainties of the input data, the Monte Carlo transport calculation itself also contributes to the final uncertainties. The number of neutrons transported for each irradiation was selected so that the resuling statistical errors were less than 5% (Fig. 5.12).

In the final cross section evaluation the uncertainties of the neutron spectra are added to the uncertainties of the guess excitation function that has usually the largest error of all input parameters entering the unfolding procedure. Our calculated spectra are given with an error of 10% at all energies but the energies below 20 MeV and the 10 MeV wide region right below the peak threshold, where the error is 50%. The later enlarges for high incident proton energies ($E_p > 120$ MeV) to a 50 MeV wide region below the peak threshold.

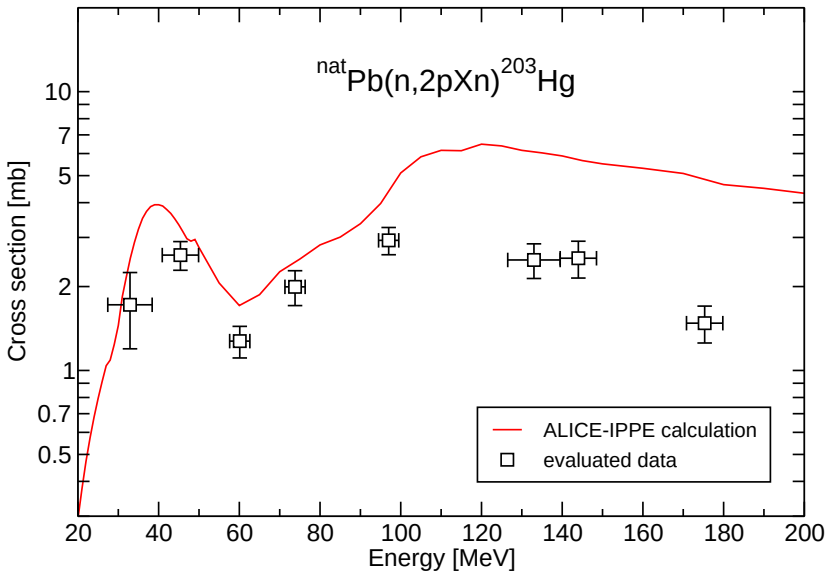

Figure 5.13: Unfolded cross sections for the reaction $^{\mathrm{nat}}\mathrm{Pb}(n,2pXn)^{203}\mathrm{Hg}$ compared to the theoretical excitation function calculated using the ALICE-IPPE code [109].

5.5.4 Preliminary evaluated cross section results

From activated target elements, excitation functions for a total of about 120 reactions will be obtained using the evaluation. For the target element lead these excitation functions cover the production of ^{95}Zr, ^{103}Ru, $^{196\mathrm{m+g}}$Au, ^{203}Hg, ^{199}Tl, ^{201}Tl, ^{202}Tl, $^{199\mathrm{m+g}}$Pb, ^{200}Pb, $^{201\mathrm{m+g}}$Pb, $^{202\mathrm{m}}$Pb,$^{203\mathrm{m+g}}$Pb, and $^{204\mathrm{m}}$Pb.

The determination of cross sections by unfolding turned out not to be feasible leading to unphysical shapes of excitation functions. This is due to the fact that the information about cross sections is not homogenously distributed on neutron energy axis but rather is concentrated at the peak neutron energies of the different experiments. Therefore the iterative approach of Kim et al. [108] was used which does not give entire excitation function but results in individual cross sections at the peak neutron energies of different experiments only. Fig. 5.13 shows evaluated cross sections for the reaction $^{\mathrm{nat}}\mathrm{Pb}(n,2pXn)^{203}\mathrm{Hg}$ [109]. These are compared to the theoretical guess excitation function calculated using the ALICE-IPPE code [41, 42]. It is apparent that the energy dependence of the new cross sections retains the shape of the original excitation function but the unfolding procedure shifted them to lower values.

Recently the problem was overcome by proper adjusting in the unfolding procedure the width of energies considered relevant for each irradiation. That means that the unfolding is performed iteratively starting with the experiment with the lowest proton energy and proceeding to higher ones. Then, in each unfolding step, all energies below the highest one are taken into account. This procedure results then in a complete excitation function up to the highest covered energy and gives the respective uncertainty of the cross sections for

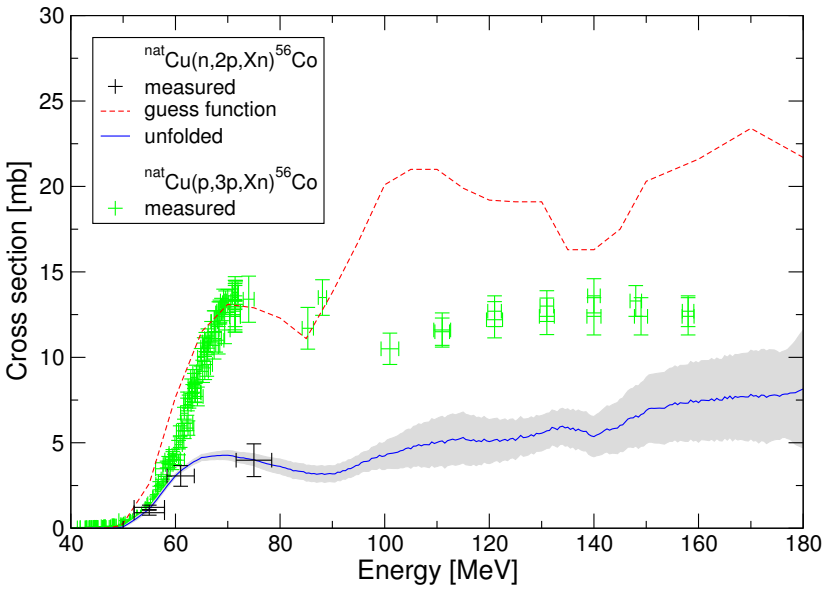

Figure 5.14: Unfolded excitation function with uncertainties for the reaction $^{\text{nat}}\text{Cu}(n, 2pXn)^{56}\text{Co}$ compared to the theoretical excitation function calculated using the ALICE-IPPE code and the data from [108]. Also shown are the measured cross sections for corresponding proton induced reaction $^{\text{nat}}\text{Cu}(p, 3pXn)^{56}\text{Co}$ from [36].

each energy point. This is exemplified for reaction $^{\text{nat}}\text{Cu}(n, 2pXn)^{56}\text{Co}$ in Fig. 5.14. Here again the guess function was calculated using the ALICE-IPPE code. As can be seen, the unfolded excitation function perfectly fits the few available data from [108]. Also shown are the cross sections for corresponding proton induced reaction $^{\text{nat}}\text{Cu}(p, 3pXn)^{56}\text{Co}$ measured in [36]. The differences emphasize the importance to distinguish between residual nuclide production in proton induced and neutron induced nuclear reactions.

The evaluation for other reactions is currently in progress.

6 Conclusions

This work was dedicated to the modeling of cosmic ray interactions with terrestrial and extraterrestrial matter and above all to the neutron interactions. First, the Monte Carlo model for (n,γ) production of cosmogenic nuclides in chondrites was presented. Second, the influence of the selection of neutron cross sections on the terrestrial nuclide production rate calculations was investigated. Finally, presented were the neutron transport calculations for activation experiments that were used for the evaluation of neutron excitation functions for residual nuclide production.

6.1 Neutron capture production in chondrites

The investigation of the neutron fluxes and the neutron capture production of cosmogenic nuclides ^{36}Cl, ^{41}Ca, ^{60}Co, ^{59}Ni, and ^{129}I in chondrites showed strong dependence on the size of the meteorite as well as on the depth of the sample below the surface. Meteoroids with radii below ≈ 35 cm are too small to moderate neutrons to thermal energies, so the n-capture production is usually much lower than spallation production. For $R < 85$ cm the production rates increase monotonically from the surface to the center. For larger radii there is a maximum at depth about 80 cm (for $R = 100$ cm) that is shifted in surface direction with increasing size, reaching 50 cm for 2π irradiation. For larger depths, the production rate decreases monotonically to the center.

Depending on the shape of the excitation function for the particular (n,γ) reaction, the shapes of the depth profiles for individual nuclides are slightly different. This difference is significant only in the case of ^{129}I for which the n-capture production is quite high already for radius 20 cm and the maximum production rate was obtained in the center of meteoroid with radius of 65 cm. This is caused by fairly increased production of ^{129}I by epithermal neutrons

Unlike spallation production, for neutron capture we found differences when considering different bulk chemical compositions of individual chondrite classes. Depending on the shape of the excitation function, these differences can change the nuclide production rate and/or the shape of its depth profile. For ordinary chondrites we obtained different values of the production rate ratio between L-, LL- and H-chondrites for each isotope. In meteorites with $R > 50$ cm the ratios were constant for all depths and sizes. In smaller meteorites the ratios

are size and eventually also depth dependent.

In CI-chondrites the presence of hydrogen in the bulk composition causes faster moderation of neutrons. Therefore there are high thermal neutron fluxes already at depths of about 15 cm. Consequently the n-capture production rate also increases faster reaching its maximum value at depth 65 cm and then decreases slower than in ordinary chondrites.

The effects of bulk composition imply the necessity of new calculations for each meteorite class and for new falls or finds of meteorites with unusual composition. This is particulary important for meteorites containing hydrogen.

The presented calculations are based on a purely physical model based on Monte Carlo simulation of particle transport and evaluated excitation functions using one free parameter – the total number of GCR particles at the meteoroid orbits. As the experimental depth profiles from meteorites are not available, we determined this parameter by adjusting calculated production rates to ^{41}Ca depth profiles measured in Apollo 15 drill core [9] and considering the heliocentric gradient of the GCR flux [64, 65]. The obtained value of $J_0(E > 10\ \mathrm{MeV}) = 2.99\ \mathrm{cm^{-2}\,s^{-1}}$ is slightly higher than the value determined in [66], most probably due to different model of the Moon and different primary particle spectrum. On the other hand, it differs significantly from both J_0 values obtained by adjusting the calculated spallation production rates of cosmogenic nuclides to the depth profiles from the L-chondrite Knyahinya in [52] and [46]. The reasons for this difference remain unknown.

The comparison of the calculated production rates to the measured cosmogenic nuclide concentrations showed a good agreement which makes it possible to conclude that this model can be used with reasonable confidence for a wide range of applications. However, improvements can be made especially when the excitation functions for the (n, γ) reactions on ^{35}Cl and ^{40}Ca are available. The model can easily be extended to other neutron capture produced nuclides which turns it into a general tool for the investigation of meteorites as well as other cosmic ray irradiated bodies in general.

6.2 Neutron cross sections and terrestrial nuclide production

The importance of the selection of the cross section set used for the calculation of cosmogenic nuclide production rate was shown before for extraterrestrial objects [7, 46]. The two sets of cross sections from the group of Reedy and the group of Michel, both widely used in cosmochemical applications, show significant differences especially for neutron induced reactions. Whereas both these sets were used successfully to describe the spallogenic production of cosmogenic nuclides in meteoroids, for the Earth's atmosphere and terrestrial surface rocks these result in different production rate predictions. The differences arise mainly from differences in neutron excitation functions.

The atmospheric production of ^{10}Be and ^{7}Be calculated using Michel's cross sections is significantly higher than that calculated using Reedy's cross sections, so the two combinations

"*cross sections* – J_0" of the group of Reedy and the group of Michel that give very similar production rate results for meteorites are not equivalent for the atmosphere. However, the comparison with experimental data is rather problematic for the atmosphere as it is not clear wheather the cosmogenic nuclide concentrations measured in the archives represent a real global average or the contribution of the local effects is significant.

For the surface rocks the irradiation geometry and studied reactions are the same as for extraterrestrial matter and therefore also the agreement for the two cross section sets is much better than for the atmosphere. For the *in-situ* produced nuclides most problems with deposition and mixing disappear. Therefore also a direct comparison to the experimental data is possible.

Generally, the use of newer cross sections from the group of Michel usually leads to higher production rates even with lower J_0 value used. As the calculation using the Reedy's cross sections underestimated the in-situ production for most nuclides when compared to the experimental data [51], the calculation using Michel's cross sections results in better agreement. However, the uncertainties of the calculations are much higher than the differences arising from different cross sections used and also from the comparison to the measured data.

Presented investigation showed that the cross sections, especially for neutron induced reactions, are crucial quantities for a proper description of the cosmogenic nuclide production in extraterrestrial as well as in terrestrial matter. Therefore a further development of experimental and calculational methods is needed for the improvement of the excitation functions for all relevant nuclear reactions.

6.3 Neutron transport for activation experiments

Irradiation experiments with quasi-monoenergetic neutron beam produced in the ^{7}Li$(p,n)^{7}$Be reaction were performed within HINDAS project in order to determine excitation functions for the production of residual radionuclides from a variety of target elements up to 175 MeV. Within this work, 6 irradiations performed at UCL/Louvain-la-Neuve, Belgium and 16 irradiations performed at TSL/Uppsala, Sweden were simulated.

The unfolding procedure used to obtain the excitation functions requires the detail description of the neutron field inside each irradiated target. As the measured neutron spectrum in a beam was not always available, semi-empirical model was used to calculate the quasi-monoenergetic neutron spectrum for such irradiations. The LAHET Code System was also used for the Monte Carlo calculation of the primary neutron spectra but it proved not to be feasible to satisfactory reproduce the measured neutron spectra.

The transport of neutrons inside the target was simulated using the LCS. The simulation covered neutron fluxes from thermal energies to energies up to 180 MeV and resulted in full neutron spectrum for all individual foils in target stack. The development of the neutron field along the stack depends on the individual foil materials used and their order in the

stack for particular irradiation. Generally, it shows the same principal characteristics for all irradiations. Moderation of neutrons in the stack but mainly the production of low-energy secondary neutrons cause an increase of neutron fluxes with energies below $\approx$ 50 MeV at the beginning of the stack. At the same time neutrons of all energies can be absorbed while passing through the stack material. For low-energy neutrons an equilibrium between production and absorption occurs in the first half of the stack where the maximum in total neutron fluxes can be seen. Further in the stack the absorption outbalances the secondary neutron production for all energies and there is an overall decrease in neutron fluxes. For higher energies only the decrease can be seen.

From the calculation it is clear that the primary effect the presence of the stack has on the energy distribution of neutrons is the decrease of fluxes at all energies. However, the relative decrease is higher at lower energies and therefore the relative energy distribution changes in favour of high energies after neutrons passed the stack.

As there were measured neutron spectra before and after passing the target stack available for all of the UCL simulated irradiations, it was possible to test the accuracy of the transport calculation. The comparison of the neutron spectrum calculated at the spectrometer position after transporting the input spectrum through the stack to the spectrum measured at that position showed very good agreement for all energies.

Measured cross sections are usually not available for neutron induced residual nuclide production and the accuracy of the theoretical excitation functions calculated using present available codes is not satisfactory not only for neutron induced reactions but also for those induced by protons. Therefore in most cases only an indirect comparison to the experimental data can be made by measuring and calculating the production rate of a particular nuclide under well known irradiation conditions including the exact description of particle fluxes. However, a few experimental data exist for some reactions and the preliminary unfolded excitation functions showed a good agreement in all such cases.

The total results of the study, for which the neutron transport calculations were done within this work, will comprise excitation functions for about 120 reactions and will, among others, provide a basis to scrutinize the capabilities of models and codes to describe adequately the differences in neutron- and proton-induced reactions.

References

[1] D. Lal and B. Peters, Cosmic ray produced radioactivity on the Earth, in *Handbuch der Physik XLVI/2*, pages 551–612, 1967.

[2] M. Honda, Spallation Products Distributed in a Thick Iron Target Bombarded by 3-Bev Protons, J. Geophys. Res. **67**, 4847 (1962).

[3] R. C. Reedy and J. R. Arnold, Interaction of solar and galactic cosmic-ray particles with the Moon, J. Geophys. Res. **77**, 537–555 (1972).

[4] K. O'Brien, Secular variations in the production of cosmogenic isotopes in the Earth's atmosphere, J. Geophys. Res. **84**, 423–431 (1979).

[5] P. Eberhardt, J. Geiss, and H. Lutz, Neutrons in meteorites, in *Earth Science and Meteoritics*, edited by J. Geiss and E. D. Goldberg, pages 143–168, North Holland, Amsterdam, 1963.

[6] J. Masarik and J. Beer, Simulation of particle fluxes and cosmogenic nuclide production in the Earth's atmosphere, J. Geophys. Res. **104**, 12099–12112 (1999).

[7] J. Masarik and R. C. Reedy, Effects of bulk composition on nuclide production processes in meteorites, Geochim. Cosmochim. Acta **58**, 5307–5317 (1994).

[8] I. Leya, H.-J. Lange, S. Neumann, R. Wieler, and R. Michel, The production of cosmogenic nuclides in stony meteoroids by galactic cosmic ray particles, Meteorit. Planet. Sci. **35**, 259–286 (2000).

[9] K. Nishiizumi, D. Fink, J. Klein, R. Middleton, J. Masarik, R. C. Reedy, and J. R. Arnold, Depth profile of ^{41}Ca in an Apollo 15 drill core and the low-energy neutron flux in the Moon, Earth Planet. Sci. Lett. **148**, 545–552 (1997).

[10] K. C. Welten, K. Nishiizumi, J. Masarik, M. W. Caffee, A. J. T. Jull, S. E. Klandrud, and R. Wieler, Cosmic-ray exposure history of two Frontier Mountain H-chondrite showers from spallation and neutron-capture products, Meteorit. Planet. Sci. **36**, 301–317 (2001).

[11] R. Michel and P. Nagel, *Internetional codes and model intercomparison for intermediate energy activation yields*, NEA/OECD Paris, NSC/DOC(97)-1, 1997.

[12] A. Koning, H. Beijers, J. Benlliure, O. Bersillon, J. Blomgren, J. Cugnon, M. Duijvestijn, P. Eudes, D. Filges, F. Haddad, S. Hilaire, C. Lebrun, F.-R. Lecolley, S. Leray, J.-P. Meulders, R. Michel, R. Neef, R. Nolte, N. Olsson, R. Ostendorf, E. Ramstroem, K.-H. Schmidt, H. Schuhmacher, I. Slypen, H.-A. Synal, and R. Weinreich, HINDAS – A European nuclear data program for accelerator-driven systems, J. Nucl. Sci. Techn., Suppl. 2 , 1161–1166 (2002).

[13] R. C. Reedy, J. R. Arnold, and D. Lal, Cosmic-ray record in solar system matter, Science **219**, 127–135 (1983).

[14] J. A. Simpson, Elemental and isotopic composition of the galactic cosmic rays, Ann. Rev. Nucl. Part. Sci. **33**, 323–381 (1983).

[15] D. A. Bryant, G. I. Powell, and C. H. Perry, The origin of high-energy cosmic rays, Nature **356**, 582–583 (1992).

[16] G. Castagnoli and D. Lal, Solar modulation effects in terrestrial production of carbon-14, Radiocarbon **22**, 133–158 (1980).

[17] R. E. McGuire, T. T. von Rosenvinge, and F. B. McDonald, The composition of solar energetic particles, Astrophys. J. **301**, 938–961 (1986).

[18] J. N. Goswami, R. E. McGuire, R. C. Reedy, D. Lal, and R. Jha, Solar flare protons and alpha particles during the last three solar cycles, J. Geophys. Res. **93**, 7195–7205 (1988).

[19] K. C. Hsieh and J. A. Simpson, The Relative Abundances and Energy Spectra of ^{3}He and ^{4}He from Solar Flares, Astrophys. J. **162**, L191–L196 (1970).

[20] M. A. I. van Hollebeke, L. S. Ma Sung, and F. B. McDonald, The variation of solar proton energy spectra and size distribution with heliolongitude, Solar Phys. **41**, 189–223 (1975).

[21] R. E. McGuire and T. T. von Rosenvinge, The energy spectra of solar energetic particles, Adv. in Space Res. **4**, 117–125 (1984).

[22] R. C. Reedy and K. Marti, Solar-cosmic-ray fluxes during the last ten million years, in *The Sun in Time*, edited by C. P. Sonett and M. S. Giampapa, M. S. Matthews, pages 260–287, University of Arizona Press, 1991.

[23] J. T. Wasson, *Meteorites: Classification and properties*, New York, Springer-Verlag New York, Inc. (Minerals and Rocks. Volume 10), 1974.

[24] A. M. Shea and F. D. Smart, A wold grid of calculated cosmic ray vertical cutoff rigidities for 1980. 0, Proc. 18th Int. Cosmic Ray Conf. **3**, 415–417 (1983).

[25] G. Wagner, J. Masarik, J. Beer, S. Baumgartner, D. Imboden, P. W. Kubik, H.-A. Synal, and M. Suter, Reconstruction of the geomagnetic field between 20 and 60 kyr BP from cosmogenic radionuclides in the GRIP ice core, NIMB **172**, 597–604 (2000).

[26] M. Frank, B. Schwarz, S. Baumann, P. W. Kubik, M. Suter, and A. Mangini, A 200 kyr record of cosmogenic radionuclide production rate and geomagnetic field intensity from ^{10}Be in globally stacked deep-sea sediments, Earth Planet. Sci. Lett. **149**, 121–129 (1997).

[27] Z. Y. Gu, D. Lal, T. S. Liu, J. Southon, M. W. Caffee, Z. T. Guo, and M. Y. Chen, Five million year ^{10}Be record in Chinese loess and red-clay: climate and weathering relationships, Earth Planet. Sci. Lett. **144**, 273–287 (1996).

[28] Z. Ceplecha, Luminous efficiency based on photographic observations of the Lost City fireball and implications for the influx of interplanetary bodies onto Earth., Astronomy And Astrophys. **311**, 329–332 (1996).

[29] C. Passow, Phenomenologische Theorie zur Berechnung einer Kaskade aus schweren Teilchen (Nukleonenkaskade) in der Materie, DESY Notiz A 285, 1962.

[30] K. O'Brien, A. de La Zerda Lerner, M. A. Shea, and D. F. Smart, The production of cosmogenic isotopes in the Earth's atmosphere and their inventories, in *The Sun in Time*, edited by C. P. Sonett and M. S. Giampapa, M. S. Matthews, pages 317–342, University of Arizona Press, 1991.

[31] R. E. Prael and H. Lichtenstein, *User guide to LCS: The LAHET Code System*, Los Alamos National Laboratory report, LA-UR-89-3014, 1989.

[32] P. Cloth, D. Filges, R. D. Neef, G. Sterzenbach, C. Reul, T. W. Armstrong, B. L. Colborn, B. Anders, and H. Brueckmann, *HERMES – High Energy Radiation Monte Carlo Elaborate System*, Juel-2203, 1988.

[33] *GEANT – detector description and simulation tool*, CERN Program Library W5013, 1994.

[34] GEANT4 home, CERN Geneva, `http://wwwinfo.cern.ch/asd/geant4/`.

[35] R. Michel, M. Gloris, H.-J. Lange, I. Leya, M. Lüpke, U. Herpers, B. Dittrich-Hannen, R. Rösel, T. Schiekel, D. Filges, P. Dragovitsch, M. Suter, H.-J. Hofmann, W. Wölfli, P. W. Kubik, H. Baur, and R. Wieler, Nuclide production by proton-induced reactions on elements ($6 \leq Z \leq 29$) in the energy range from 800 to 2600 MeV, NIMB **103**, 183–222 (1995).

[36] R. Michel, R. Bodemann, H. Busemann, R. Daunke, M. Gloris, H.-J. Lange, B. Klug, A. Krins, I. Leya, M. Lüpke, S. Neumann, H. Reinhardt, M. Schnatz-Büttgen, U. Herpers, T. Schiekel, F. Sudbrock, B. Holmqvist, H. Condé, P. Malmborg, M. Suter, B. Dittrich-Hannen, P.-W. Kubik, H.-A. Synal, and D. Filges, Cross sections for the production of residual nuclides by low- and medium-energy protons from the target elements C, N, O, Mg, Al, Si, Ca, Ti, V, Mn, Fe, Co, Ni, Cu, Sr, Y, Zr, Nb, Ba and Au, NIMB **129**, 153–193 (1997).

[37] M. Imamura, S. Shibata, K. Nishiizumi, and M. W. Caffee, Measurements of proton-induced production cross sections for ^{36}Cl from Ca and K, NIMB **123**, 330–333 (1997).

[38] C. Stan-Sion, D. Huggle, E. Nolte, A. Blinov, and M. Dumitru, AMS measurements of the production cross sections of ^{36}Cl with protons up to 1 GeV, NIMB **117**, 26–30 (1996).

[39] J. M. Sisterson, K. Kim, A. Beverding, P. A. J. Englert, M. Caffee, A. J. T. Jull, D. J. Donahue, L. McHargue, C. Castaneda, J. Vincent, and R. C. Reedy, Measurement of proton production cross sections of ^{10}Be and ^{26}Al from elements found in lunar rocks, NIMB **123**, 324–329 (1997).

[40] V. McLane, *EXFOR basics - A short guide to the nuclear reaction data exchange format*, IAEA report IAEA-NDS-206, 2000, `http://www-nds.iaea.or.at/exfor/`.

[41] Y. N. Shubin, V. P. Lunev, A. Y. Konobeyev, and A. I. Dityuk, *Cross-secton data library MENDL-2 to study activation and transmutation of materials irradiated by nucleons of intermediate energies*, IAEA report INDC(CCP)-385, 1995.

[42] A. I. Dityuk, A. Y. Konobeyev, V. P. Lunev, and Y. N. Shubin, *New advanced version of computer code ALICE-IPPE*, IAEA report INDC(CCP)-410, 1998.

[43] V. McLane and members of the cross section evaluation working group, *ENDF-201, ENDF/B-VI summary documentation supplement*, NNDC BNL report, BNL-NCS-17541, 1991, `http://www.nndc.bnl.gov/nndc/endf/`.

[44] J. Rowlands, *The JEF-2.2 nuclear data library*, OECD/NEA Data Bank, JEFF report 17, 2000, `http://t2.lanl.gov/cgi-bin/nuclides/jefind`.

[45] K. Shibata, T. Nakagawa, T. Asami, T. Fukahori, T. Narita, S. Chiba, M. Mizumoto, A. Hasegawa, Y. Kikuchi, Y. Nakajima, and S. Igarasi, *JENDL-3*, JAERI report 1319, 1990, `http://wwwndc.tokai.jaeri.go.jp/jendl/jendl.html`.

[46] I. Leya, H.-J. Lange, M. Lüpke, U. Neupert, R. Daunke, O. Fanenbruck, R. Michel, R. Rösel, B. Meltzow, T. Schiekel, F. Sudbrock, U. Herpers, D. Filges, G. Bonani,

B. Dittrich-Hannen, M. Suter, P. W. Kubik, and H.-A. Synal, Simulation of the interaction of GCR protons with meteoroids: On the production of radionuclides in thick gabbro and iron targets irradiated isotropically with 1.6 GeV protons, Meteorit. Planet. Sci. **35**, 287–318 (2000).

[47] J. M. Sisterson, D. T. L. Jones, F. D. Brooks, A. Buffler, M. S. Allie, M. S. Herbert, M. R. Nchodu, S. Makupula, J. Ullmann, and R. C. Reedy, Revised calculations of the production rates for Co isotopes in meteorites using new cross sections for neutron-induced reactions, in *Lunar Planet. Sci. Conf. Abstracts*, volume 33, pages 1541+, 2002.

[48] T. Nakamura, H. Sugita, M. Imamura, Y. Uwamino, H. Nagai, and K. Kobayashi, Measurement of the long-lived ^{26}Al production cross section in the ^{27}Al(n,2n) reaction, Phys. Rev. C **43**, 1831–1837 (1991).

[49] T. Nakamura, H. Sugita, M. Imamura, Y. Uwamino, S. Shibata, H. Nagai, M. Takabatake, and K. Kobayashi, Measurement of long-lived ^{10}Be, ^{14}C and ^{26}Al production cross section for $10-40$ MeV neutrons by accelerator mass spectrometry, in *Nucl. Data for Sci. and Technology Conf. Proc.*, pages 714–716, Springer Verlag, Berlin, 1991.

[50] R. C. Reedy, A model for GCR-particle fluxes in stony meteorites and production rates of cosmogenic nuclides, J. Geophys. Res. **90**, 722 (1985).

[51] J. Masarik and R. C. Reedy, Terrestrial cosmogenic-nuclide production systematics calculated from numerical simulations, Earth Planet. Sci. Lett. **136**, 381–395 (1995).

[52] R. C. Reedy, J. Masarik, K. Nishiizumi, J. R. Arnold, R. C. Finkel, M. W. Caffee, J. Southon, A. J. T. Jull, and D. J. Donahue, Cosmogenic-radionuclide profiles in Knyahinya: New measurements and models, in *Lunar Planet. Sci. Conf. Abstracts*, volume 24, pages 1195–1196, 1993.

[53] R. C. Reedy and J. Masarik, Cosmogenic-nuclide depth profiles in the lunar surface, in *Lunar Planet. Sci. Conf. Abstracts*, volume 25, pages 1119–1120, 1994.

[54] I. Leya, S. Neumann, R. Wieler, and R. Michel, The production of cosmogenic nuclides by galactic cosmic-ray particles for 2π exposure geometries, Meteorit. Planet. Sci. **36**, 1547–1561 (2001).

[55] M. Wahlen, R. C. Finkel, M. Imamura, C. P. Kohl, and J. R. Arnold, ^{60}Co in lunar samples, Earth Planet. Sci. Lett. **19**, 315–320 (1973).

[56] D. S. Woolum and D. S. Burnett, In-situ measurement of the rate of ^{235}U fission induced by lunar neutrons, Earth Planet. Sci. Lett. **21**, 153–163 (1973).

[57] M. S. Spergel, R. C. Reedy, O. W. Lazareth, P. W. Levy, and L. A. Slatest, Cosmogenic neutron-capture-produced nuclides in stony meteorites, J. Geophys. Res. **91**, 483–494 (1986).

[58] R. E. Lingenfelter, E. H. Canfield, and V. E. Hampel, The lunar neutron flux revisited, Earth and Planetary Science Letters **16**, 355–369 (1972).

[59] O. Fanenbruck, Produktion kosmogener Nuklide in Meteoroiden durch niederenergetische Neutronen, Master's thesis, University of Hanover, Germany, 1994.

[60] J. F. Breismeister, *MCNP—A Monte Carlo N-Particle Transport Code, version 4B*, Los Alamos National Laboratory report, LA-12625-M, 1997.

[61] B. Mason, Cosmochemistry Part 1. Meteorites, in *Data of geochemistry*, edited by M. Fleischer, US Govt. Printing Office, Washington DC, 1979.

[62] J. T. Wasson and G. W. Kallemeyn, Compositions of chondrites, Royal Society of London Philosophical Transactions Series **325**, 535–544 (1988).

[63] C. Schnabel, I. Leya, M. Gloris, R. Michel, J. M. López-Gutiérrez, M. Suter, U. Herpers, J. Kuhnhenn, and H. Synal, Production rates and proton induced production cross sections of ^{129}I from Te and Ba and an attempt to model the ^{129}I in meteorites, Meteorit. Planet. Sci. submitted (2003).

[64] J. A. van Allen and B. A. Randall, Interplanetary cosmic ray intensity – 1972–1984 and out to 32 AU, J. Geophys. Res. **90**, 1399–1412 (1985).

[65] W. R. Webber and J. A. Lockwood, Interplanetary cosmic-ray radial and latitudinal gradients derived in 1984 using IMP 8, Voyager, and Pioneer data, Astrophys. J. **302**, 511–516 (1986).

[66] I. Leya, R. Wieler, and A. N. Halliday, The influence of cosmic-ray production on extinct nuclide systems, Geochim. Cosmochim. Acta **67**, 529–541 (2003).

[67] G. Heusser, Z. Ouyang, T. Kirsten, U. Herpers, and P. Englert, Conditions of the cosmic ray exposure of the Jilin chondrite, Earth Planet. Sci. Lett. **72**, 263–272 (1985).

[68] M. Honda, K. Nishiizumi, M. Imamura, N. Takaoka, O. Nitoh, K. Horie, and K. Komura, Cosmogenic nuclides in the Kirin chondrite, Earth Planet. Sci. Lett. **57**, 101–109 (1982).

[69] J. Klein, D. Fink, R. Middleton, S. Vogt, and G. F. Herzog, ^{41}Ca in the Jilin (H5) Chondrite: A Matter of Size, LPI Contributions **766**, 120 (1991).

[70] D. D. Bogard, L. E. Nyquist, B. M. Bansal, D. H. Garrison, H. Wiesmann, G. F. Herzog, A. A. Albrecht, S. Vogt, and J. Klein, Neutron-capture ^{36}Cl, ^{41}Ca, ^{36}Ar, and ^{150}Sm in large chondrites: Evidence for high fluences of thermalized neutrons, J. Geophys. Res. **100**, 9401–9416 (1995).

[71] R. Michel, P. Dragovitsch, P. Englert, F. Peiffer, R. Stück, S. Theis, F. Begemann, H. Weber, P. Signer, R. Wieler, D. Filgesand, and P. Cloth, On the depth dependence of spallation reactions in a spherical thick diorite target homogeneously irradiated by 600 MeV protons : Simulation of production of cosmogenic nuclides in small meteorites, NIMB **16**, 61–82 (1986).

[72] R. Michel, F. Peiffer, S. Theis, F. Begemann, H. Weber, P. Signer, R. Wieler, P. Cloth, P. Dragovitsch, D. Filges, and P. Englert, Production of Stable and Radioactive Nuclides in Thick Stony Targets (r = 15 and 25 Cm) Isotropically Irradiated with 600 Mev Protons and Simulation of the Production of Cosmogenic Nuclides in Meteorites, NIMB **42**, 76–100 (1989).

[73] R. Michel, I. Leya, and L. Borges, Production of cosmogenic nuclides in meteoroids: Accelerator experiments and model calculations to decipher the cosmic ray record in extraterrestrial matter, NIMB **113**, 434–444 (1996).

[74] J. Beer, F. Joos, C. Lukasczyk, W. Mendel, J. Rodriguez, U. Siegenhalter, and R. Stellmacher, ^{10}Be as an indicator of solar variability and climate, in *The Solar Engine and Its Influence on Terrestrial Atmosphere and Climate*, edited by E. Nesme-Ribes, pages 221–233, Springer Verlag, New York, 1994.

[75] M. C. Monaghan, S. Krishnaswami, and K. K. Turekian, The global-average production rate of ^{10}Be, Earth Planet. Sci. Lett. **76**, 279–287 (1986).

[76] J.-L. Reyss, Y. Yokoyama, and F. Guichard, Production cross sections of ^{26}Al, ^{22}Na, ^{7}Be from argon and of ^{10}Be, ^{7}Be from nitrogen – Implications for production rates of ^{26}Al and ^{10}Be in the atmosphere, Earth Planet. Sci. Lett. **53**, 203–210 (1981).

[77] K. Nishiizumi, C. P. Kohl, E. L. Winterer, J. Klein, and R. Middleton, Cosmic ray production rates of ^{10}Be and ^{26}Al in quartz from glacially polished rocks, J. Geophys. Res. **94**, 17907–17915 (1989).

[78] K. Nishiizumi, C. P. Kohl, J. R. Arnold, J. Klein, and D. Fink, Cosmic ray produced ^{10}Be and ^{26}Al in Antarctic rocks – Exposure and erosion history, Earth Planet. Sci. Lett. **104**, 440–454 (1991).

[79] E. T. Brown, J. M. Edmond, G. M. Raisbeck, F. Yiou, M. D. Kurz, and E. J. Brook, Examination of surface exposure ages of Antarctic moraines using in situ produced ^{10}Be and ^{26}Al, Geochim. Cosmochim. Acta **55**, 2269–2283 (1991).

[80] A. J. T. Jull, N. Lifton, W. M. Phillips, and J. Quade, Studies of the production rate of cosmic-ray produced ^{14}C in rock surfaces, NIMB **92**, 308–310 (1994).

[81] S. Niedermann, T. Graf, J. S. Kim, C. P. Kohl, K. Marti, and K. Nishiizumi, Cosmic-ray-produced ^{21}Ne in terrestrial quartz: The neon inventory of Sierra Nevada quartz separates, Earth Planet. Sci. Lett. **125**, 341–355 (1994).

[82] M. G. Zerda, F. M. Phillips, D. Elmore, P. W. Kubik, P. Sharma, and R. I. Dorn, Cosmogenic chlorine-36 production rates in terrestrial rocks, Earth Planet. Sci. Lett. **105**, 94–109 (1991).

[83] J. Stone, G. L. Allan, L. K. Fifield, J. M. Evans, and A. R. Chivas, Limestone erosion measurements with cosmogenic chlorine-36 in calcite – preliminary results from Australia, NIMB **92**, 311–316 (1994).

[84] D. Lal, In situ-produced cosmogenic isotopes in terrestrial rocks, Ann. Rev. Earth Planet. Sci. **16**, 355–358 (1988).

[85] I. Leya and Michel, Determination of neutron cross section for nuclide production at intermediate energies by deconvolution of thick-target production rates, in *Nucl. Data for Sci. and Technology Conf. Proc.*, volume 59, pages 1463–1467, 1998.

[86] F. G. Perey, Least-squares dosimetry unfolding: The program STAY'SL, ORNL report ORNL/TM-6062, ENDF-254, NEA Data Bank, 1977.

[87] U. J. Schrewe, H. J. Brede, M. Matzke, R. Nolte, J. P. Meulders, H. Schumacher, and I. Slypen, ^{107,109}Ag$(n, 3/5n)^{105}$Ag reaction cross section for 20 MeV $< E_n <$ 70 MeV, in *Nucl. Data for Sci. and Technology Conf. Proc.*, pages 669–671, Springer Verlag, Berlin, 1991.

[88] S. Neumann, *Aktivierungsexperimente mit Neutronen mitlerer Energie und die Produktion kosmogener Nuklide in extraterrestrischer Materie*, PhD thesis, Universität Hannover, 1999.

[89] S. Neumann, R. Michel, F. Sudbrock, U. Herpers, P. Malmborg, O. Jonsson, B. Holmqvist, H. Condé, P.-W. Kubik, and M. Suter, A new facility at the Svedberg Laboratory for activation experiments with medium energy neutrons, in *Nucl. Data for Sci. and Technology Conf. Proc.*, volume 59, pages 379–383, 1998.

[90] A. D. Carlson, S. Chiba, F.-J. Hambsch, N. Olsson, and A. N. Smirnov, Update to "Nuclear data standards for nuclear measurements", in *Nucl. Data for Sci. and Technology Conf. Proc.*, volume 59, pages 1223–1229, 1997.

[91] R. Michel, W. Glasser, S. Neumann, U. Herpers, A. N. Smirnov, A. V. Prokofiev, P. Malmborg, and O. Jonsson, Activation experiments with medium-energy neutrons for the determination of residual nuclide production cross section, TSL report 1998/99, 2000.

[92] A. Bol, P. Leleux, P. Lipnik, P. Macq, and A. Ninane, A novel design for a fast intense neutron beam, NIMA **214**, 169–173 (1983).

[93] H. Schuhmacher, B. R. L. Siebert, and H. J. Brede, Measurement of neutron fluence for energies between 20 MeV and 65 MeV using a proton recoil telescope, in *Proceedings of a specialists' meeting on neutron cross section standards for the energy region above 20 MeV*, pages 123–134, NEA, OECD, Paris, 1991.

[94] V. Dangendorf, R. Nolte, F. Roos, H. Schuhmacher, B. R. L. Siebert, and M. Weyrauch, Proton recoil telescopes for fluence measurement in neutron beams of 20–200 MeV energy, NIMA **469**, 205–215 (2001).

[95] H. Schuhmacher, H. J. Brede, V. Dangendorf, M. Kuhfuss, J. P. Meulders, W. D. Newhauser, and R. Nolte, Quasi-monoenergetic neutron beams with energies from 25 to 70 MeV, NIMA **421**, 284–295 (1999).

[96] K. S. Krane, *Introductory nuclear physics*, John Wiley & Sons, New York, 1987.

[97] C. H. Poppe, J. D. Anderson, J. C. Davis, S. M. Grimes, and C. Wong, Cross sections for the ^{7}Li$(p,n)^7$Be reaction between 4.2 and 26 MeV, Phys. Rev. C **14**, 438–445 (1976).

[98] C. J. Batty, B. E. Bonner, E. Friedman, C. Tschalar, L. E. Williams, A. S. Clough, and J. B. Hunt, The ^{6}Li$(p,n)^6$Be and ^{7}Li$(p,n)^7$Be reactions at intermediate proton energies, Nucl. Phys. A **120**, 297–320 (1986).

[99] H. H. Andersen and J. F. Ziegler, *Stopping Powers and ranges in all elements*, volume 3, Pergamon Press, 1977.

[100] N. Nakao, Y. Uwamino, T. Nakamura, T. Shibata, N. Nakanishi, M. Takada, E. Kim, and T. Kurosawa, Development of a quasi-monoenergetic neutron field using the ^{7}Li$(p,n)^7$Be reaction in the 70–210 MeV energy range at RIKEN, NIMA **420**, 218–231 (1999).

[101] T. Nakamura, M. Takada, N. Nakao, M. Baba, T. Iwasaki, H. Nakashima, S. Tanaka, S. Meigo, Y. Sakamoto, Y. Nakane, S. Tanaka, Y. Uwamino, and N. Nakanishi, Quasi-monoenergetic neutron fields for neutron cross section and shielding experiments in the energy range of 20 to 200 MeV, in *Nucl. Data for Sci. and Technology Conf. Proc.*, volume 59, pages 1508–1512, 1997.

[102] M. Baba, T. Kiyosumi, T. Iwasaki, M. Yoshioka, S. Matsuyama, N. Hirakawa, T. Nakamura, S. Tanaka, R. Tanaka, S. Tanaka, H. Nakashima, and S. Meigo, Characterization and application of 20–90 MeV ^{7}Li(p,n) neutron source at TIARA, in *Nucl. Data for Sci. and Technology Conf. Proc.*, pages 90–92, 1994.

[103] M. Baba, Y. Nauchi, T. Iwasaki, T. Kiyosumi, M. Yoshioka, S. Matsuyama, N. Hirakawa, T. Nakamura, S. Tanaka, S. Meigo, H. Nakashima, S. Tanaka, and N. Nakao, Characterization of a 40–90 MeV ^{7}Li(p,n) neutron source at TIARA using a proton recoil telescope and a TOF method, NIMA **428**, 454–465 (1999).

[104] G. G. Ohlsen, Kinematic relations in reactions of the form $A+B \longrightarrow C+D+E$, NIM **37**, 240–248 (1965).

[105] A. S. Botvina, A. S. Iljinov, I. N. Mishustin, J. P. Bondorf, R. Donangelo, and K. Sneppen, Statistical simulation of the breakup of highly excited nuclei, Nucl. Phys. **A 475**, 663–686 (1987).

[106] U. J. Schrewe, W. D. Newhauser, H. J. Brede, V. Dangendorf, P. M. DeLuca, Jr, S. Gerdung, R. Nolte, P. Schmelzbach, H. Schuhmacher, and T. Lim, Measurement of neutron kerma factors in C and O: Neutron energy range of 20 MeV to 70 MeV, Rad. Prot. Dosim. **61**, 275–280 (1995).

[107] M. B. Chadwick, P. M. DeLuca, Jr., and R. C. Haight, Nuclear data needs for neutron therapy and radiation protection, Rad. Prot. Dosim. **70**, 1–12 (1997).

[108] E. J. Kim, T. Nakamura, Y. Uwamino, N. Nakanishi, M. Imamura, N. Nakao, S. Shibata, and S. Tanaka, Measurements of activation cross sections on spalation reactions for ^{59}Co and $^{\mathrm{nat}}$Cu at incident neutron energies of 40 to 120 MeV, J. Nucl. Sci. Techn. **36**, 29–40 (2002).

[109] W. Glasser, R. Michel, S. Neumann, H. Schuhmacher, H. J. Brede, V. Dagendorf, R. Nolte, U. Herpers, A. N. Smirnov, I. Ryzhov, P. A. V., P. Malmborg, D. Kollar, and J. P. Meulders, Radionuclide production from lead by neutron induced reactions up to 175 MeV, Nucl. Data for Sci. and Techn., Supplement 2 , 373–376 (2002).

Zhrnutie

Modelovanie interakcií kozmického žiarenia s objektami Slnečnej sústavy a konkrétne modelovanie produkcie kozmogénnych nuklidov je nutnou súčasťou interpretácie nameraných dát pre široké spektrum aplikácií. Táto práca sa sústreďuje na tri hlavné problémy patriace do problematiky modelovania interakcií kozmického žiarenia.

Ako prvý je prezentovaný model na produkciu kozmogénnych nuklidov v reakciách neutrónového záchytu v mimozemských objektoch Slnečnej sústavy. Motiváciou na vývoj takéhoto modelu bola neexistencia systematiky pre (n, γ) reakcie v meteoritoch a povrchoch planét založenej na Monte Carlo simulácii transportu častíc. Keďže pre spalačné reakcie takéto systematiky existujú [46, 51], snahou bolo ich rozšírenie aj na reakcie neutrónového záchytu. Toky častíc v meteoroidoch rôznych veľkostí a chemického zloženia boli simulované pomocou programového balíka LCS [31], ktorý zahŕňa kód MCNP [60] na simuláciu transportu neutrónov až do termálnych energií. Na výpočet produkčných rýchlostí kozmogénnych rádionuklidov ^{36}Cl, ^{41}Ca, ^{60}Co, ^{59}Ni a ^{129}I ako funkcií veľkosti meteoroidu a hĺbky pod jeho povrchom boli použité excitačné funkcie z evaluovaných súborov ENDF/B-VI [43] a JEF-2.2 [44].

Ukazuje sa, že produkčné rýchlosti uvedených izotopov silne závisia od veľkosti ožarovaného meteoroidu ako aj od hĺbky pod jeho povrchom. Na rozdiel od produktov spalačných reakcií sú však pri reakciách neutrónového záchytu zreteľné aj rozdiely spôsobené malými odchýlkami v chemickom zložení medzi jednotlivými triedami meteoritov. Pri L-, LL- a H- podtriedach obyčajných chondritov sme pre meteoroidy s $R > 50$ cm zistili konštantné rozdiely produkcií medzi podtriedami s meniacou sa veľkosťou aj hĺbkou. Tieto rozdiely sú spôsobené hlavne odlišnou koncentráciou ľahkých prvkov (hlavne kyslíka), ktoré majú lepšie moderačné schopnosti a tiež rozdielmi v koncentrácii železa, ktoré má vysoký účinný prierez pre záchyt termálnych neutrónov. Pre jednotlivé nuklidy sa tieto rozdiely v závislosti od excitačných funkcií pre ich produkciu pohybujú v rozmedzí 2–30%. Pre CI-chondrity, ktoré obsahujú vodík, sa hĺbkové profily produkčných rýchlostí výrazne odlišujú od profilov v obyčajných chondritoch. Z týchto efektov spôsobených odlišným chemickým zložením vyplýva potreba samostatných výpočtov pre každú triedu meteoritov a predovšetkým pre meteority s nezvyčajným chemickým zložením.

Jediný voľný parameter modelu, stredný tok častíc galaktického kozmického žiarenia, je

možné určit' porovnaním napočítaných hĺbkových profilov s profilmi nameranými v meteoritoch. Keďže však tieto nie sú k dispozícii, určili sme tento parameter porovnaním s profilom ^{41}Ca nameranom v mesačných vzorkách z Apolla 15 [9] a zahrnutím gradientu heliomagnetického poľa [64, 65]. Získaná hodnota $J_0(E > 10\ \mathrm{MeV}) = 2.99\ \mathrm{cm^{-2}\,s^{-1}}$ sa výrazne odlišuje od hodnôt určených porovnaním napočítaných produkcií spalačných produktov s hĺbkovými profilmi nameranými v L-chondrite Knyahinya ($4.8\ \mathrm{cm^{-2}\,s^{-1}}$ [51], resp. $4.06\ \mathrm{cm^{-2}\,s^{-1}}$ [46]). Príčina tohoto rozdielu je neznáma a poukazuje na potrebu d'alšieho výskumu v tejto oblasti.

Porovnanie napočítaných produkčných rýchlostí s koncentráciami nuklidov nameranými v meteoritoch ukazuje na dobrú zhodu. Je preto možné použit' tento model s postačujúcou presnost'ou pre široké spektrum aplikácií. Model je možné jednoducho rozšírit' o d'alšie kozmogénne nuklidy, čo z neho robí univerzálny nástroj na skúmanie meteoritov ako aj d'alších vesmírnych objektov.

Ďalším skúmaným problémom je štúdium vplyvu výberu sady neutrónových účinných prierezov na produkciu kozmogénnych nuklidov v zemskej atmosfére a na zemskom povrchu. Dôležitost' tohoto výberu bola ukázaná pre mimozemské objekty. Dve sady účinných prierezov vyvíjané skupinami Rolfa Michela a Roberta C. Reedyho, obe často používané v kozmochemických aplikáciách [napr. 46, 51], ukazujú značné rozdiely hlavne pre jadrové reakcie indukované neutrónmi. Zatiaľčo obidve tieto sady boli úspešne použité na popis spalačnej produkcie kozmogénnych nuklidov v meteoroidoch, pre zemskú atmosféru a zemský povrch pri ich použití vychádzajú rozdielne predpovede produkčných rýchlostí. Ako už bolo spomenuté, tieto rozdiely vyplývajú prevažne z rozdielov v použitých neutronových účinných prierezoch.

Produkčné rýchlosti ^{10}Be a ^{7}Be v atmosfére napočítané pomocou Michelových účinných prierezov sú podstatne vyššie ako napočítané pomocou Reedyho účinných prierezov, takže dve kombinácie parametrov „*účinné prierezy* – J_0" (Reedy – $J_0 = 4.8\ \mathrm{cm^{-2}\,s^{-1}}$, Michel – $J_0 = 4.06\ \mathrm{cm^{-2}\,s^{-1}}$), ktoré dávali podobné výsledky pre meteority, nie sú ekvivalentné pre zemskú atmosféru . Pre zemský povrch je situácia lepšia. Je to spôsobené tým, že geometria ožarovania aj uvažované reakcie sú tie isté ako v prípade mimozemských objektov, na ktorých boli obidve sady účinných prierezov vyvíjané.

Vo všeobecnosti sa dá povedat', že použitie novšej Michelovej sady účinných prierezov vedie k vyšším produkčným rýchlostiam a to aj napriek nižšej hodnote použitého stredného toku častíc galaktického kozmického žiarenia J_0. Porovnanie s experimentálnymi dátami vedie k lepšej zhode pri použití Michelovych účinných prierezov, avšak rozdiely medzi výslednými produkciami sú pod hranicou presnosti výpočtov.

Z uvedeného vyplýva potreba d'alších experimentov zameraných na meranie účinných prierezov predovšetkým pre reakcie indukované neutrónmi ako aj d'alšie štúdium teórie jadrových reakcií, ktoré by umožnilo vývoj spoľahlivých kódov na výpočet excitačných funkcií jadrových reakcií.

V poslednej časti práce sú prezentované simulácie transportu neutrónov pre neutrónové aktivačné experimenty. Tieto experimenty boli uskutočnené v rámci projektu HINDAS [12] s cieľom určiť excitačné funkcie pre produkciu zostatkových rádionuklidov z mnohých terčových prvkov až do energií neutrónov dosahujúcich 175 MeV. V práci je nasimulovaných 6 ožarovaní na urýchľovači v UCL/Louvain-la-Neuve v Belgicku a 16 ožarovaní na urýchľovači v TSL/Uppsala vo Švédsku kvázimonoenergenickým zväzkom neutrónov produkovaným v reakcii $^{7}\mathrm{Li}(p,n)^{7}\mathrm{Be}$.

Na získanie excitačných funkcii jednotlivých reakcií je potrebný detailný popis neutrónového poľa v každom ožarovanom terči. Keďže namerané spektrum neutrónov vo zväzku nebolo k dispozícii pre všetky uvažované experimenty, boli otestované dva modely na jeho výpočet: semiempirický model [88] a stochastický Monte Carlo model. V porovnaní s experimentálnymi kvázimonoenergetickými spektrami neutrónov lepšie obstál semiempirický model, ktorý bol potom použitý pre všetky ožarovania, pri ktorých nebolo spektrum vo zväzku merané.

Transport neutrónov v terčoch bol simulovaný pomocou programového balíka LCS. Simulácia pokrývala toky neutrónov od termálnych energií až do energie 180 MeV a jej výsledkom bolo úplné neutrónové spektrum pre každú fóliu v terči pri danom ožarovaní. Vývoj spektra pozdĺž terča závisí od materiálov jednotlivých fólií ako aj na poradí fólií v danom terči a vykazuje podobné vlastnosti pre všetky ožarovania. Moderácia neutrónov v terči ako aj produkcia nízkoenergetických sekundárnych neutrónov prispievajú k zvýšeniu toku neutrónov s energiou pod ≈ 50 MeV na začiatku terča. Zároveň však dochádza k absorpcii neutrónov. Pri nízkoenergetických neutrónoch nastáva v prvej polovici terča rovnováha medzi produkciou a absorpciou, ktorá sa prejavuje ako maximum toku neutrónov. Ďalej v terči presahuje absorpcia neutrónov ich produkciu pre všetky energie a dochádza k poklesu toku neutrónov. Pre vysokoenergetické neutróny je pozorovaný len pokles toku pozdĺž celého terča.

Dobrá zhoda nasimulovaných a nameraných spektier neutrónov po prechode terčom poukazuje na správnosť použitej metódy a dáva predpoklady na získanie čo možno najpresnejších excitačných funkcií. Aj keď nie sú namerané účinné prierezy pre neutrónmi indukované spalačné jadrové reakcie väčšinou k dispozícii, prvé získané excitačné funkcie sú s existujúcimi dátami v dobrej zhode. V súčasnosti prebieha vyhodnocovanie dát z experimentov a výsledky budú zahŕňať excitačné funkcie pre približne 120 reakcií.

APPENDICES

A Examples of input files for LCS calculations

Isotropic irradiation of spherical meteoroid

INH input file for the LAHET run for the irradiation of spherical L-chondrite with radius 20 cm:

```
1-20

689426811
10000,34,01,23,1e7, 1e9,,,,, ,0.0/
,-1,,1,12,1/
0,0,0,0,-1,0,0,1/
0,0,1,1,1,1,1,1,1,1,1,1,1,1,1,1,1,1/
,,/
20001.,,,,,,,,,,,8.0,,8.0/
0.0,47,47/
  6,  12,  1.5618e-04,  5
  6,  13,  1.7531e-06,  5
  8,  16,  4.9547e-02,  7
  8,  17,  1.8873e-05,  7
  8,  18,  9.9331e-05,  7
 11,  23,  6.4177e-04,  8
 12,  24,  1.0207e-02,  8
 12,  25,  1.2921e-03,  8
 12,  26,  1.4226e-03,  8
 13,  27,  9.5304e-04,  8
 14,  28,  1.2805e-02,  9
 14,  29,  6.4837e-04,  9
 14,  30,  4.3040e-04,  9
 15,  31,  6.4647e-05, 10
 16,  32,  1.3741e-03, 10
 16,  33,  1.0846e-05, 10
 16,  34,  6.0881e-05, 10
 16,  36,  2.8922e-07, 10
 19,  39,  4.1979e-05, 10
 19,  40,  5.2666e-09, 10
 19,  41,  3.0295e-06, 10
 20,  40,  6.6787e-04, 11
 20,  42,  4.4575e-06, 11
 20,  43,  9.3007e-07, 11
 20,  44,  1.4371e-05, 11
 20,  46,  2.7558e-08, 11
 20,  48,  1.2883e-06, 11
 22,  46,  2.2886e-06, 11
 22,  47,  2.0639e-06, 11
 22,  48,  2.0451e-05, 11
 22,  49,  1.5008e-06, 11
 22,  50,  1.4370e-06, 11
 24,  50,  6.8339e-06, 12
 24,  52,  1.3179e-04, 12
 24,  53,  1.4943e-05, 12
 24,  54,  3.7197e-06, 12
 25,  55,  9.8600e-05, 13
 26,  54,  4.7430e-04, 13
 26,  56,  7.4456e-03, 13
 26,  57,  1.7195e-04, 13
 26,  58,  2.2883e-05, 13
 27,  59,  2.1101e-05, 13
 28,  58,  2.9337e-04, 14
 28,  60,  1.1300e-04, 14
 28,  61,  4.9126e-06, 14
 28,  62,  1.5669e-05, 14
 28,  64,  3.9904e-06, 14
1      1   -3.5    -2 3
2      1   -3.5    -3 4
3      1   -3.5    -4 5
4      1   -3.5    -5 6
5      1   -3.5    -6 7
6      1   -3.5    -7 8
7      1   -3.5    -8 9
8      1   -3.5    -9 10
9      1   -3.5    -10 11
10     1   -3.5    -11 12
11     1   -3.5    -12 13
12     1   -3.5    -13 14
13     1   -3.5    -14 15
14     1   -3.5    -15 16
15     1   -3.5    -16 17
16     1   -3.5    -17 18
17     1   -3.5    -18 19
18     1   -3.5    -19 20
19     1   -3.5    -20 21
20     1   -3.5    -21
21     0           -1 2
22     0            1

1      so   21.0
2      so   20.0
3      so   19.0
4      so   18.0
5      so   17.0
6      so   16.0
7      so   15.0
```

```
8       so   14.0
9       so   13.0
10      so   12.0
11      so   11.0
12      so   10.0
13      so   9.0
14      so   8.0
15      so   7.0
16      so   6.0
17      so   5.0
18      so   4.0
19      so   3.0
20      so   2.0
21      so   1.0

in      1 20r 0
print

15,,0.0,,20.1/
0.1,10.,11.678,13.638,15.926,18.598,21.719,
25.363,29.619,34.589,40.394,47.171,55.087,
64.33,75.125,87.731,102.45,119.64,139.72,
163.16,190.54,222.51,259.85,303.46,354.38,
413.84,483.28,564.37,659.08,769.67,898.82,
1049.6,1225.8,1431.4,1671.6,1952.1,2279.7,
2662.2,3109.,3630.6,4239.8,4951.3,5782.1,
6752.3,7885.4,9208.5,10754.,12558.,14665.,
17126.,20000./
0.,0.000267,0.000319,0.00039,0.000485,
0.000615,0.00079,0.001026,0.001345,
0.001773,0.002348,0.003117,0.004143,
0.005508,0.007316,0.009699,0.012826,
0.016903,0.022186,0.028976,0.037633,
0.048565,0.062227,0.079101,0.099672,
0.124402,0.153684,0.187787,0.226818,
0.270647,0.31891,0.370951,0.425932,
0.482669,0.539993,0.596595,0.651248,
0.702847,0.750543,0.793699,0.832002,
0.865377,0.89396,0.91807,0.938134,
0.954629,0.96806,0.978896,0.987582,
0.994506,1./
```

INP input file for the HMCNP run for the irradiation of spherical L-chondrite with radius 20 cm:

```
l-20
1       1   -3.5    -2 3
2       1   -3.5    -3 4
3       1   -3.5    -4 5
4       1   -3.5    -5 6
5       1   -3.5    -6 7
6       1   -3.5    -7 8
7       1   -3.5    -8 9
8       1   -3.5    -9 10
9       1   -3.5    -10 11
10      1   -3.5    -11 12
11      1   -3.5    -12 13
12      1   -3.5    -13 14
13      1   -3.5    -14 15
14      1   -3.5    -15 16
15      1   -3.5    -16 17
16      1   -3.5    -17 18
17      1   -3.5    -18 19
18      1   -3.5    -19 20
19      1   -3.5    -20 21
20      1   -3.5    -21
21      0           -1 2
22      0            1

1       so   21.0
2       so   20.0
3       so   19.0
4       so   18.0
5       so   17.0
6       so   16.0
7       so   15.0
8       so   14.0
9       so   13.0
10      so   12.0
11      so   11.0
12      so   10.0
13      so   9.0
14      so   8.0
15      so   7.0
16      so   6.0
17      so   5.0
18      so   4.0
19      so   3.0
20      so   2.0
21      so   1.0

imp:n  1 20r 0
files  77 neutp s u 0  70 11mh. s u 0
m1      6000.50c  -0.90000e-03
        8016.50c  -0.37700e+00
       11023.50c  -0.70000e-02
       12000.50c  -0.14900e+00
       13027.50c  -0.12200e-01
       14000.50c  -0.18500e+00
       15031.50c  -0.95000e-03
       16032.50c  -0.22000e-01
       19000.50c  -0.82500e-03
       20000.50c  -0.13100e-01
       22000.50c  -0.63000e-03
       24000.50c  -0.38800e-02
       25055.50c  -0.25700e-02
       26000.55c  -0.21500e+00
       27059.50c  -0.59000e-03
       28000.50c  -0.12000e-01
f4:n   1 2 3 4 5 6 7 8 9 10 11 12 13 14
       15 16 17 18 19 20
e4     1e-12 1e-11 1e-10 2e-10 3e-10 4e-10
       5e-10 6e-10 7e-10 8e-10 9e-10 1e-9
       2e-9 4e-9 7e-9 1e-8 2e-8 5e-8 7e-8
       1e-7 2e-7 3e-7 4e-7 5e-7 6e-7 7e-7
       8e-7 9e-7 1e-6 2e-6 3e-6 4e-6 5e-6
       6e-6 7e-6 8e-6 9e-6 1e-5 2e-5 3e-5
       4e-5 5e-5 6e-5 7e-5 8e-5 9e-5 1e-4
       2e-4 3e-4 4e-4 5e-4 6e-4 7e-4 8e-4
       9e-4 1e-3 2e-3 3e-3 4e-3 5e-3 6e-3
       7e-3 8e-3 9e-3 1e-2 2e-2 3e-2 4e-2
       5e-2 6e-2 7e-2 8e-2 9e-2 0.1 0.2
       0.3 0.4 0.5 0.6 0.7 0.8 0.9 1.0
       2.0 3.0 4.0 5.0 6.0 7.0 8.0 9.0
       10.0 11.0 12.0 13.0 14.0 15.0 16.0
       17.0 18.0 19.0 20.0
wwg:n  4 1 0 0. 0. 0.
print
```

INT input file for the HTAPE run for the irradiation of spherical L-chondrite with radius 20 cm with output neutrons:

```
l-20: neutrons/
/
4,-38,0,1,0,20/
30.,40.,50.,60.,70.,80.,90.,100.,120.,
140.,160.,180.,200.,250.,300.,350.,400.,
450.,500.,550.,600.,700.,800.,900.,1000.,
1500.,2000.,2500.,3000.,3500.,4000.,
4500.,5000.,6000.,7000.,8000.,9000.,
10000./
1/
1,2,3,4,5,6,7,8,9,10,11,12,13,14,15,16,
17,18,19,20/
```

INT input file for the HTAPE run for the irradiation of spherical L-chondrite with radius 20 cm with output protons:

```
l-20: protons/
/
2,-58,0,1,0,19/
1.0,2.0,3.0,4.0,5.0,6.0,7.0,8.0,9.0,10.0,
11.0,12.0,13.0,14.0,15.0,16.0,17.0,18.0,
19.0,20.,30.,40.,50.,60.,70.,80.,90.,
100.,120.,140.,160.,180.,200.,250.,300.,
350.,400.,450.,500.,550.,600.,700.,800.,
900.,1000.,1500.,2000.,2500.,3000.,3500.,
4000.,4500.,5000.,6000.,7000.,8000.,
9000.,10000./
0/
3,4,5,6,7,8,9,10,11,12,13,14,15,16,17,
18,19,20,21/
```

Neutron transport for activation experiments

INH input file for LAHET run for *louv04* irradiation:

```
LOUV04

128517231
100000,7,11,23,1e8,1e9,,,,,,,,/
1,-1,,,,1/
0,0,0,0,-1,0,0,0/
1,0,1,1,1,1,1,1,1,1,1,1,1,1,1,1,1/
,,/
65.0,,20.0,,,,,,,,8.0,,8.0/
0.0,2,2/
29,63,0.0585363,14/
29,65,0.02609,14/
0.0,4,4/
82,204,0.00046183,22/
82,206,0.00795,22/
82,207,0.0072902,22/
82,208,0.0172855,22/
0,2,2/
47,107,0.0303823,17/
47,109,0.0282369,17/
0,5,5/
28,58,0.0621649,14/
28,60,0.0239457,14/
28,61,0.001041,14/
28,62,0.0033184,14/
28,64,0.00084558,14/
0,1,1/
27,59,0.090944,13/
0,4,4/
26,54,0.0049604,13/
26,56,0.0778681,13/
26,57,0.0017983,13/
26,58,0.00023932,13/
0,1,1/
13,27,0.0603,8/
0,6,6/
8,16,0.0453586,7/
8,17,0.00001728,7/
8,18,0.00009093,7/
14,28,0.020336,9/
14,29,0.0010297,9/
14,30,0.00068355,9/
0,2,2/
6,12, 0.1115577,5/
6,13, 0.0012522,5/
0,8,8/
52,120,0.00002832,18/
52,122,0.0007678,18/
52,123,0.00026783,18/
52,124,0.0014206,18/
52,125,0.0021058,18/
52,126,0.0055902,18/
52,128,0.0093466,18/
52,130,0.0099696,18/
0,3,3/
14,28,0.1771912,9/
14,29,0.0089719,9/
14,30,0.0059557,9/
  1  0           1 -2 3 -4 5 -9
  2  1 -8.93     1 -2 3 -4 7 9 -10
  3  1 -8.93     9 -10 -7
  4  2 -11.35    1 -2 3 -4 7 10 -11
  5  2 -11.35    10 -11 -7
  6  1 -8.93     1 -2 3 -4 7 11 -12
  7  1 -8.93     11 -12 -7
  8 10 -6.25     1 -2 3 -4 8 12 -13
  9 10 -6.25     12 -13 -8
 10  1 -8.93     1 -2 3 -4 7 13 -14
 11  1 -8.93     13 -14 -7
 12  3 -10.5     1 -2 3 -4 7 14 -15
 13  3 -10.5     14 -15 -7
 14  1 -8.93     1 -2 3 -4 7 15 -16
 15  1 -8.93     15 -16 -7
 16  4 -8.9      1 -2 3 -4 7 16 -17
 17  4 -8.9      16 -17 -7
 18  1 -8.93     1 -2 3 -4 7 17 -18
 19  1 -8.93     17 -18 -7
 20  5 -8.9      1 -2 3 -4 7 18 -19
 21  5 -8.9      18 -19 -7
 22  1 -8.93     1 -2 3 -4 7 19 -20
```

```
 23  1 -8.93      19 -20 -7
 24  6 -7.87      1 -2 3 -4 7 20 -21
 25  6 -7.87      20 -21 -7
 26  1 -8.93      1 -2 3 -4 7 21 -22
 27  1 -8.93      21 -22 -7
 28 11 -8.96      1 -2 3 -4 7 22 -23
 29 11 -8.96      22 -23 -7
 30  1 -8.93      1 -2 3 -4 7 23 -24
 31  1 -8.93      23 -24 -7
 32  7 -2.7       1 -2 3 -4 7 24 -25
 33  7 -2.7       24 -25 -7
 34  1 -8.93      1 -2 3 -4 7 25 -26
 35  1 -8.93      25 -26 -7
 36  8 -2.2       1 -2 3 -4 7 26 -27
 37  8 -2.2       26 -27 -7
 38  1 -8.93      1 -2 3 -4 7 27 -28
 39  1 -8.93      27 -28 -7
 40  9 -2.25      1 -2 3 -4 7 28 -29
 41  9 -2.25      28 -29 -7
 42  1 -8.93      1 -2 3 -4 7 29 -30
 43  1 -8.93      29 -30 -7
 44  0            1 -2 3 -4 30 -6
 45  0            -1:2:-3:4:-5:6

  1  px   -5.0
  2  px    5.0
  3  py   -5.0
  4  py    5.0
  5  pz   -0.2
  6  pz    6.0
  7  cz    1.25
  8  cz    1.0
  9  pz    0.0
 10  pz    0.2
 11  pz    0.4
 12  pz    0.8
 13  pz    0.9
 14  pz    1.1
 15  pz    1.5
 16  pz    1.7
 17  pz    2.0
 18  pz    2.2
 19  pz    2.5
 20  pz    2.7
 21  pz    3.0
 22  pz    3.2
 23  pz    3.6
 24  pz    3.8
 25  pz    4.1
 26  pz    4.3
 27  pz    4.6
 28  pz    4.8
 29  pz    5.3
 30  pz    5.5

in   1 43r 0
print

14,,1.,-0.1,5.0,5.0/
0.5,1.5,2.5,3.5,4.5,5.5,6.5,7.5,8.5,9.5,
10.5,11.5,12.5,13.5,14.5,15.5,16.5,17.5,
18.5,19.5,20.5,21.5,22.5,23.5,24.5,25.5,
26.5,27.5,28.5,29.5,30.5,31.5,32.5,33.5,
34.5,35.5,36.5,37.5,38.5,39.5,40.5,41.5,
42.5,43.5,44.5,45.5,46.5,47.5,48.5,49.5,
50.5,51.5,52.5,53.5,54.5,55.5,56.5,57.5,
58.5,59.5,60.5,61.5/
0.0,0.005290,0.021760,0.033891,0.045841,
0.060951,0.070751,0.081652,0.094182,
0.107932,0.120312,0.134473,0.143673,
0.155953,0.167353,0.177604,0.187084,
0.204764,0.215964,0.226235,0.237535,
0.248945,0.261785,0.274785,0.290226,
0.306416,0.320346,0.335797,0.352067,
0.367187,0.380778,0.394258,0.407178,
0.421468,0.433139,0.445369,0.457309,
0.469049,0.483440,0.495600,0.506300,
0.518130,0.530041,0.542391,0.557721,
0.569851,0.583032,0.598672,0.611512,
0.622062,0.634453,0.646823,0.659183,
0.671533,0.683864,0.696184,0.708494,
0.720784,0.752195,0.860007,0.967719,1.0/
```

INP input file for MCNP run for *louv04* irradiation:

```
LOUV04
  1  0            1 -2 3 -4 5 -9
  2  1 -8.93      1 -2 3 -4 7 9 -10
  3  1 -8.93      9 -10 -7
  4  2 -11.35     1 -2 3 -4 7 10 -11
  5  2 -11.35     10 -11 -7
  6  1 -8.93      1 -2 3 -4 7 11 -12
  7  1 -8.93      11 -12 -7
  8 10 -6.25      1 -2 3 -4 8 12 -13
  9 10 -6.25      12 -13 -8
 10  1 -8.93      1 -2 3 -4 7 13 -14
 11  1 -8.93      13 -14 -7
 12  3 -10.5      1 -2 3 -4 7 14 -15
 13  3 -10.5      14 -15 -7
 14  1 -8.93      1 -2 3 -4 7 15 -16
 15  1 -8.93      15 -16 -7
 16  4 -8.9       1 -2 3 -4 7 16 -17
 17  4 -8.9       16 -17 -7
 18  1 -8.93      1 -2 3 -4 7 17 -18
 19  1 -8.93      17 -18 -7
 20  5 -8.9       1 -2 3 -4 7 18 -19
 21  5 -8.9       18 -19 -7
 22  1 -8.93      1 -2 3 -4 7 19 -20
 23  1 -8.93      19 -20 -7
 24  6 -7.87      1 -2 3 -4 7 20 -21
 25  6 -7.87      20 -21 -7
 26  1 -8.93      1 -2 3 -4 7 21 -22
 27  1 -8.93      21 -22 -7
 28 11 -8.96      1 -2 3 -4 7 22 -23
 29 11 -8.96      22 -23 -7
 30  1 -8.93      1 -2 3 -4 7 23 -24
 31  1 -8.93      23 -24 -7
 32  7 -2.7       1 -2 3 -4 7 24 -25
 33  7 -2.7       24 -25 -7
 34  1 -8.93      1 -2 3 -4 7 25 -26
 35  1 -8.93      25 -26 -7
 36  8 -2.2       1 -2 3 -4 7 26 -27
 37  8 -2.2       26 -27 -7
 38  1 -8.93      1 -2 3 -4 7 27 -28
 39  1 -8.93      27 -28 -7
 40  9 -2.25      1 -2 3 -4 7 28 -29
 41  9 -2.25      28 -29 -7
 42  1 -8.93      1 -2 3 -4 7 29 -30
 43  1 -8.93      29 -30 -7
 44  0            1 -2 3 -4 30 -6
 45  0            -1:2:-3:4:-5:6
```

```
  1  px   -5.0
  2  px    5.0
  3  py   -5.0
  4  py    5.0
  5  pz   -0.2
  6  pz    6.0
  7  cz    1.25
  8  cz    1.0
  9  pz    0.0
 10  pz    0.2
 11  pz    0.4
 12  pz    0.8
 13  pz    0.9
 14  pz    1.1
 15  pz    1.5
 16  pz    1.7
 17  pz    2.0
 18  pz    2.2
 19  pz    2.5
 20  pz    2.7
 21  pz    3.0
 22  pz    3.2
 23  pz    3.6
 24  pz    3.8
 25  pz    4.1
 26  pz    4.3
 27  pz    4.6
 28  pz    4.8
 29  pz    5.3
 30  pz    5.5

imp:n   1 43r 0
files  77  neutp s u 0  70 11mh. s u 0
m1    29000.50c  1.0
m2    82000.50c  1.0
m3    47000.55c  1.0
m4    28000.50c  1.0
m5    27059.50c  1.0
m6    26000.50c  1.0
m7    13027.50c  1.0
m8    14000.50c  0.333334 8016.50c 0.666666
m9    6000.50c  1.0
m10   53127.55c 1.0
m11   14000.50c 1.0
f4:n  3 5 7 9 11 13 15 17 19 21 23 25 27 29
      31 33 35 37 39 41 43 44
e4    1 2 3 4 5 6 7 8 9 10 11 12 13 14 15
      16 17 18 19 20
print
```

INT input file for HTAPE run for *louv04* irradiation:

```
LOUV04/
/
4,-136,0,1,0,22/
20.,21.,22.,23.,24.,25.,26.,27.,28.,29.,
30.,31.,32.,33.,34.,35.,36.,37.,38.,39.,
40.,41.,42.,43.,44.,45.,46.,47.,48.,49.,
50.,51.,52.,53.,54.,55.,56.,57.,58.,59.,
60.,61.,62.,63.,64.,65.,66.,67.,68.,69.,
70.,71.,72.,73.,74.,75.,76.,77.,78.,79.,
80.,81.,82.,83.,84.,85.,86.,87.,88.,89.,
90.,91.,92.,93.,94.,95.,96.,97.,98.,99.,
100.,101.,102.,103.,104.,105.,106.,107.,
108.,109.,110.,111.,112.,113.,114.,115.,
116.,117.,118.,119.,120.,121.,122.,123.,
124.,125.,126.,127.,128.,129.,130.,132.,
134.,136.,138.,140.,142.,144.,146.,148.,
150.,152.,154.,156.,158.,160.,162.,164.,
166.,168.,170.,172.,174.,176.,178.,180./
1/
3,5,7,9,11,13,15,17,19,21,23,25,27,29,
31,33,35,37,39,41,43,44/
```

B Cross sections used for calculations

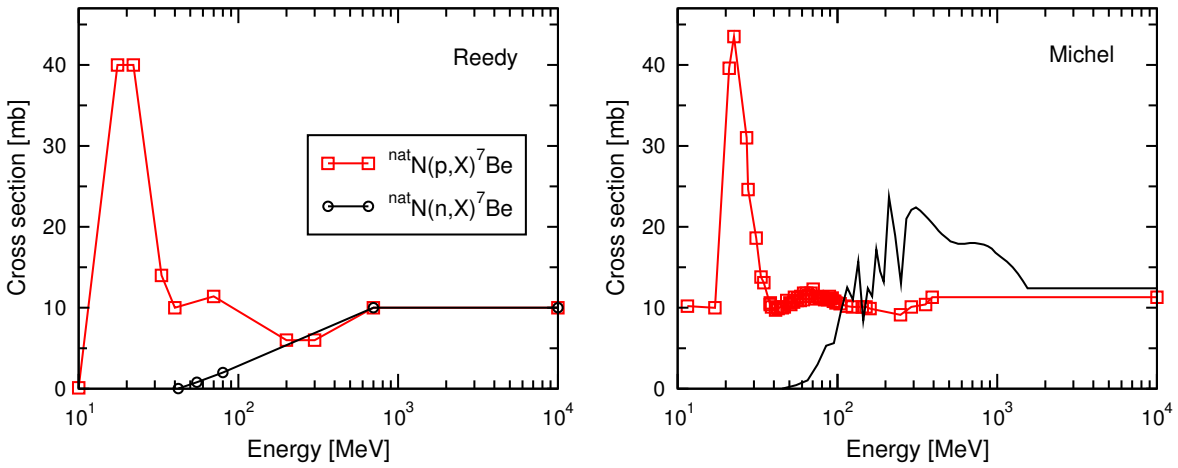

Figure B.1: Cross sections for spallation production of ^{7}Be in reactions on nitrogen.

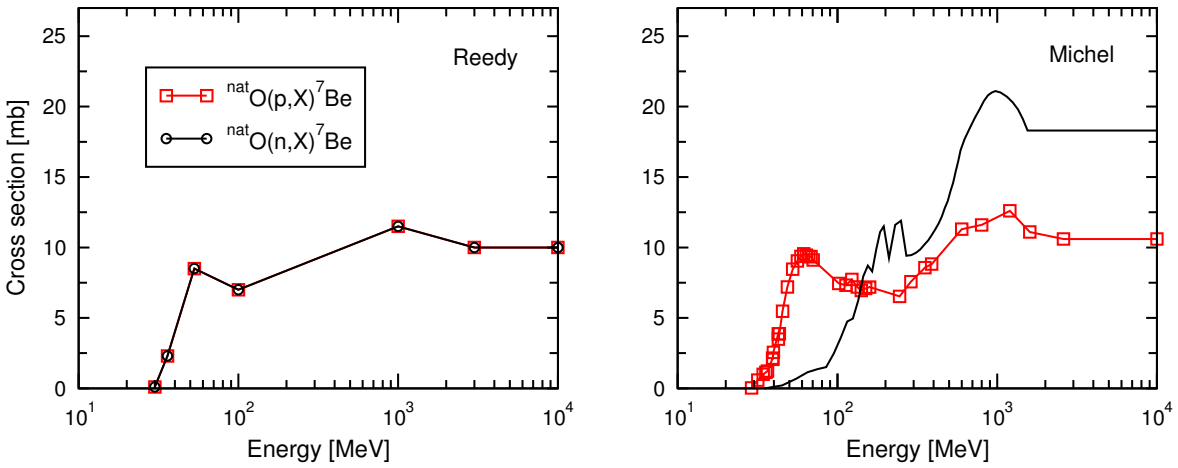

Figure B.2: Cross sections for spallation production of ^{7}Be in reactions on oxygen.

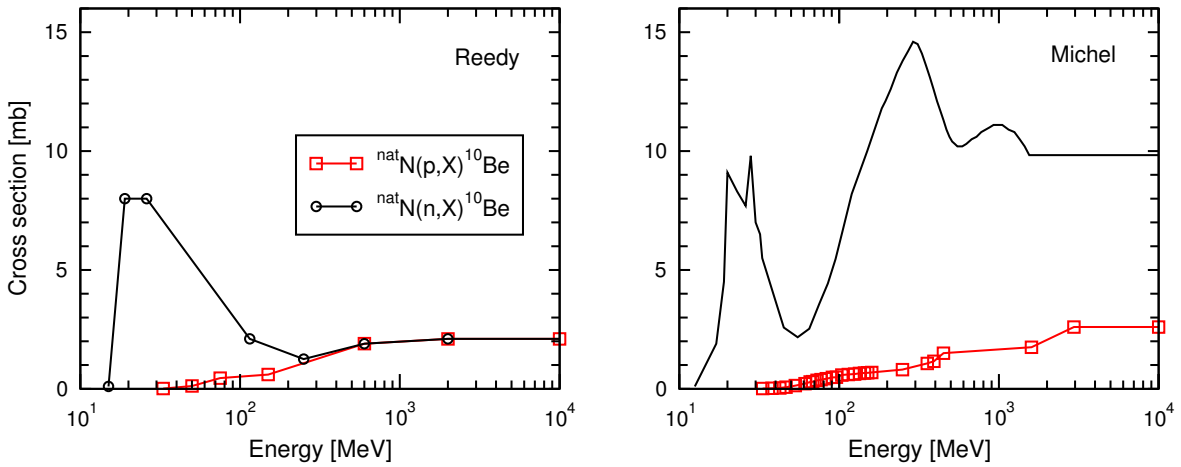

Figure B.3: Cross sections for spallation production of ^{10}Be in reactions on nitrogen.

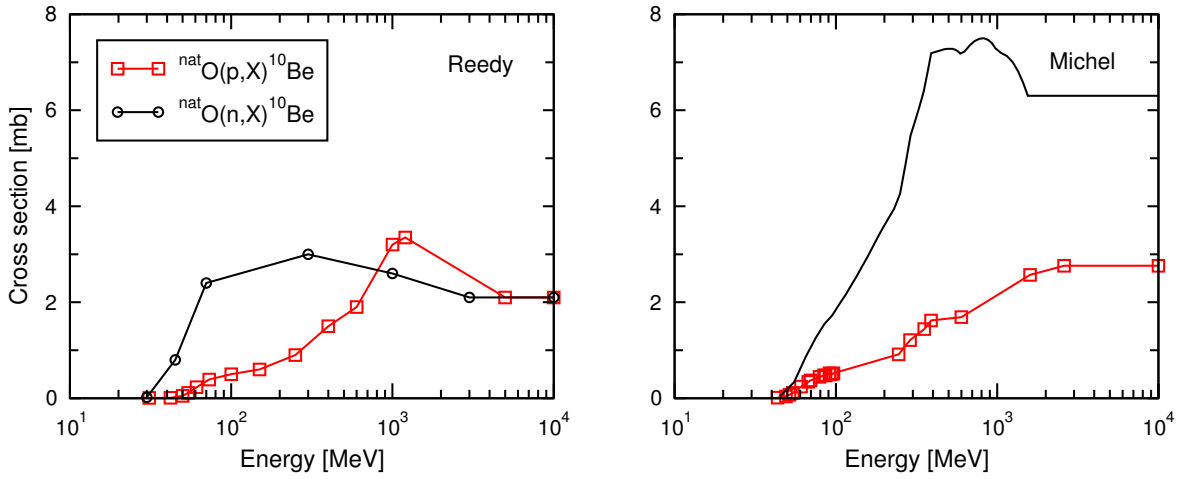

Figure B.4: Cross sections for spallation production of ^{10}Be in reactions on oxygen.

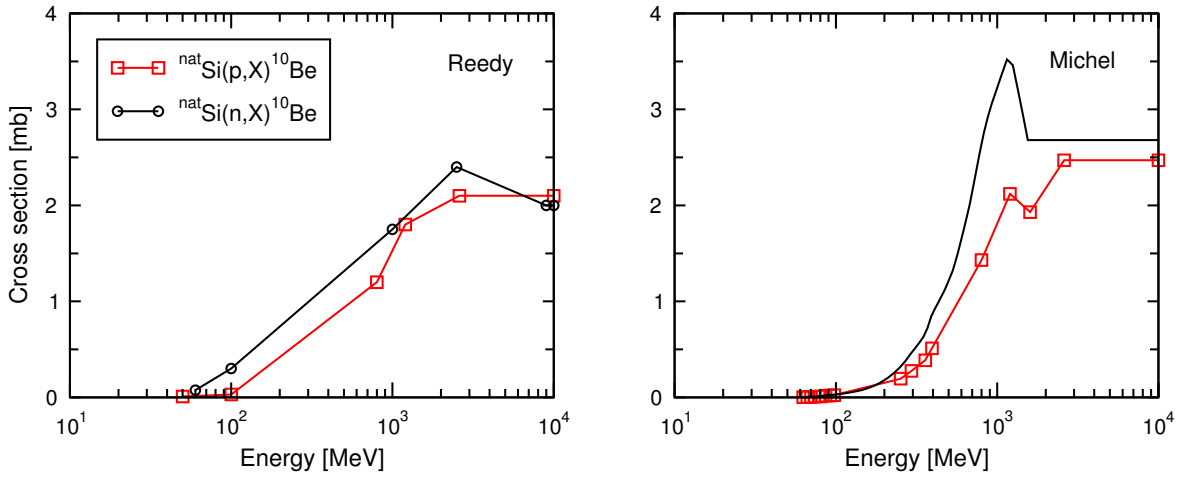

Figure B.5: Cross sections for spallation production of ^{10}Be in reactions on silicon.

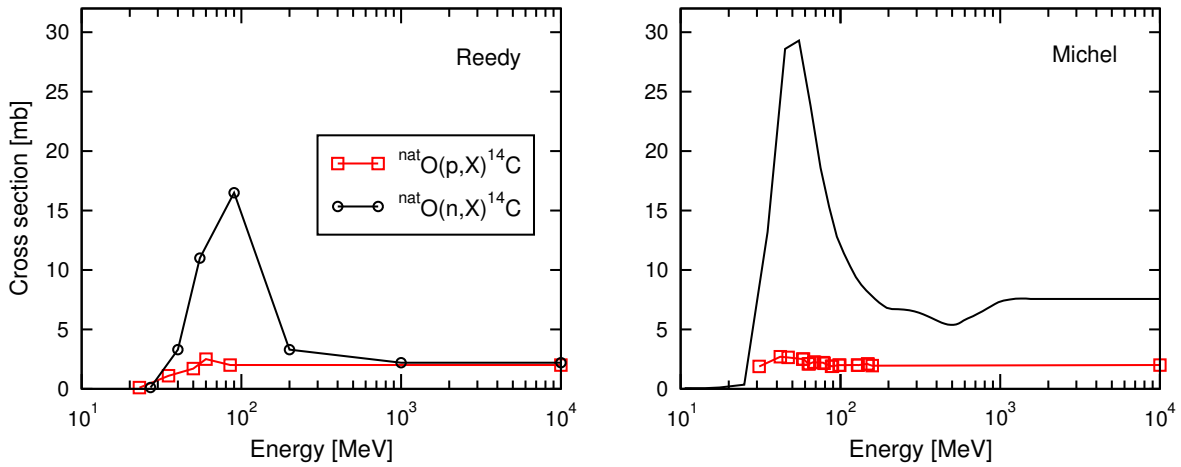

Figure B.6: Cross sections for spallation production of ^{14}C in reactions on oxygen.

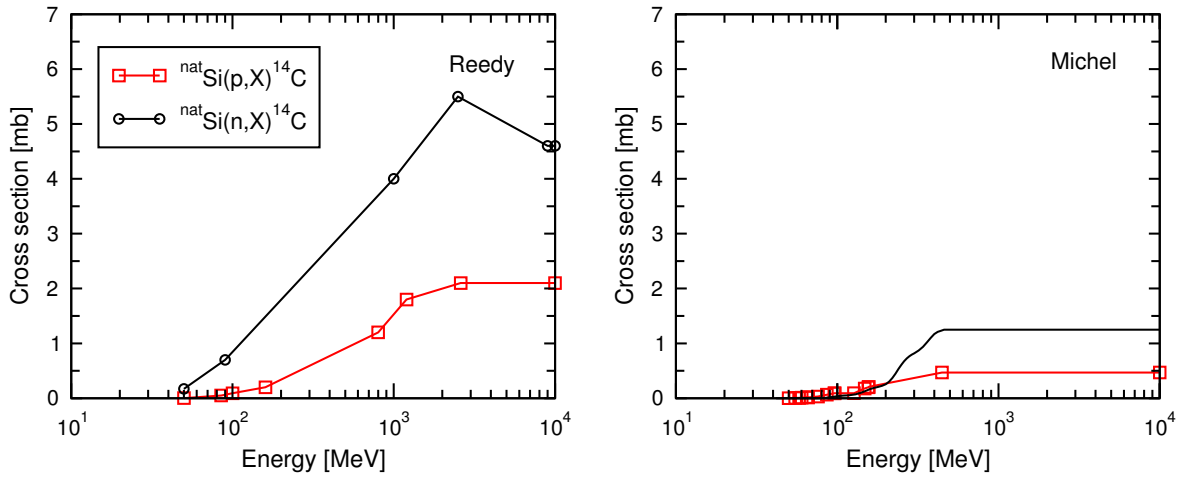

Figure B.7: Cross sections for spallation production of ^{14}C in reactions on silicon.

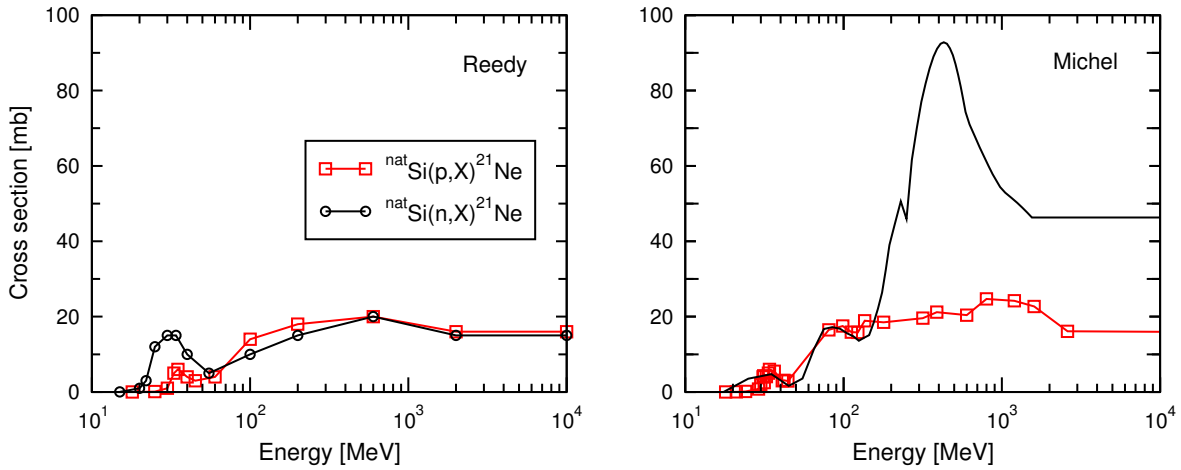

Figure B.8: Cross sections for spallation production of ^{21}Ne in reactions on silicon.

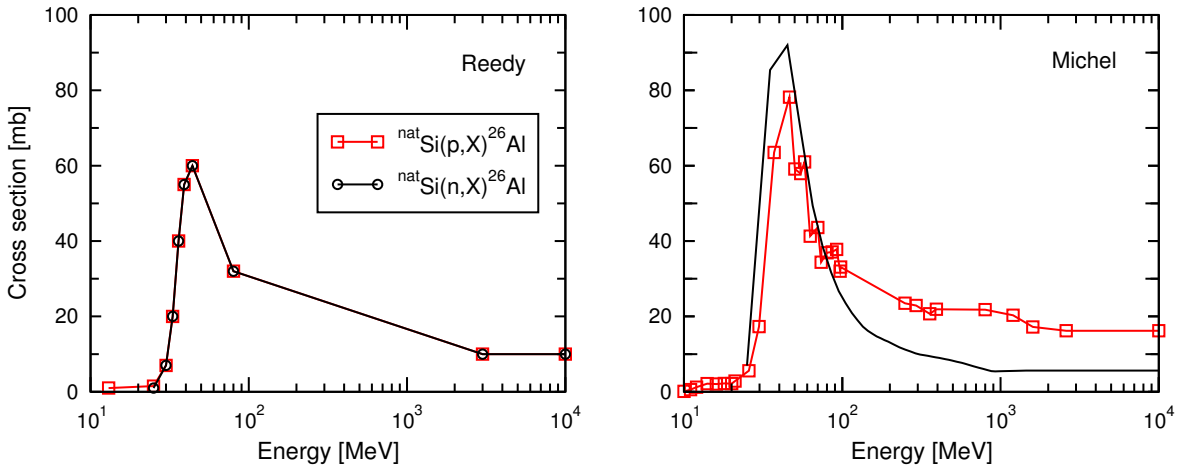

Figure B.9: Cross sections for spallation production of ^{26}Al in reactions on silicon.

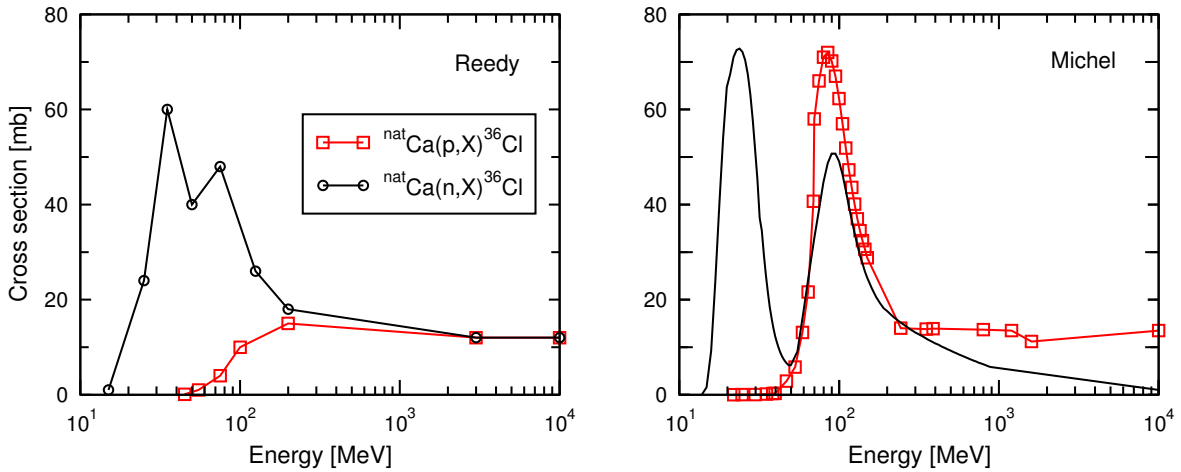

Figure B.10: Cross sections for spallation production of ^{36}Cl in reactions on silicon.

C Parameters for neutron irradiation experiments

Table C.1: Detailed information about neutron irradiations performed at UCL/Lovain-la-Neuve. The neutrons were produced by protons with energy E_p on a d thick Li target, E_n is mean energy of neutrons in peak.

Irradiation	louv02	louv03	louv04	louv05	louv06	louv07
Date	10/97	04/98	11/98	12/00	05/01	11/01
E_p [MeV]	36.4	48.5	62.9	48.5	62.9	36.4
E_n [MeV]	32.9	45.4	60.1	45.3	60.0	32.8
d(Li) [mm]	5	5	5	5	5	5
Foils in the stack	Cu	Cu	Cu	Cu	Cu	Cu
	Pb	Pb	Pb	U	U	U
	Cu	Cu	Cu	Cu	Cu	Cu
	Ag	Te	Te			
	Cu	Cu	Cu			
	Ni	Ag	Ag			
	Cu	Cu	Cu			
	Co	Ni	Ni			
	Cu	Cu	Cu			
	Fe	Co	Co			
	Cu	Cu	Cu			
	Al	Fe	Fe			
	Cu	Cu	Cu			
	SiO_2	Si	Si			
	Cu	Cu	Cu			
	C	Al	Al			
	Cu	Cu	Cu			
	Te	SiO_2	SiO_2			
		Cu	Cu			
		C	C			
		Cu	Cu			
Lenght [mm]	50.0	55.0	55.0	8.64	8.64	8.64

Table C.2: Detailed information about neutron irradiations performed at TSL/Uppsala. The neutrons were produced by protons with energy $E_p \pm \Delta E_p$ on a d thick Li target, E_n is mean energy of neutrons in peak. For irradiations with $E_p > 90$ MeV the input spectra were adjusted according to (5.15) using the given value of the parameter A.

Irradiation	uppn09	uppn0b	uppn0e	uppn0f	uppn0h	uppn0k	uppn0l	uppn0m
Date	03/97	05/97	01/98	06/98	09/98	09/98	10/98	05/99
E_p [MeV]	97.5	162.7	98.5	98.6	49.19	69.19	96.8	136.7
ΔE_p [MeV]	0.3	1.0	0.3	0.3	0.1	0.2	0.3	1.0
E_n [MeV]	94.5	159.3	96.1	96.2	46.2	66.4	94.4	133.0
d(Li) [mm]	8	15	4	4	4	4	4	15
A [10^{-3}]	7.0	5.3	7.0	7.0			7.0	5.0
Foils in the stack	Pb	Pb	Cu	Cu	Cu	Cu	Cu	Cu
	Cu	Cu	Ag	Ag	Pb	Pb	Ag	Ag
	Ag	Ag	Cu	Cu	Cu	Cu	Cu	Cu
	Cu	Cu	Pb	Te	Ag	Ag	Te	Co
	Ni	Ni	Cu	Cu	Cu	Cu	Cu	Cu
	Cu	Cu	Co	Si	Co	Co	Mg	Mg
	Co	Co	Cu	Cu	Cu	Cu	Cu	Cu
	Cu	Cu	Si	Al	Fe	Fe	Pb	Pb
	Fe	Fe	Cu	Cu	Cu	Cu	Cu	Cu
	Cu	Cu	SiO_2	Mg	Si	Si	Ni	Ni
	Si	Si	Cu	Cu	Cu	Cu	Cu	Cu
	Cu	Cu	C	Te	Al	Al	Fe	Fe
	SiO_2	SiO_2	Cu	Cu	Cu	Cu	Cu	Cu
	Cu		Ag	Si	SiO_2	SiO_2	Al	Al
	Al		Cu	Cu	Cu	Cu	Cu	Cu
	Cu			Al	C	C	SiO_2	SiO_2
	C			Cu	Cu	Cu	Cu	Cu
	Cu			Mg	Ni	Ni	C	C
				Cu			Cu	Cu
Lenght [mm]	63.0	64.0	50.0	58.0	52.0	52.0	57.0	50.0

Table C.2: (continued)

Irradiation	uppn0n	uppn0o	uppn0p	uppn0q	uppn0r	uppn0s	uppn0t	uppn0u
Date	11/99	12/99	05/00	10/00	02/01	06/01	09/01	02/02
E_p [MeV]	97.9	76.4	178.8	148.4	68.1	137.4	177.3	98.1
ΔE_p [MeV]	1.0	0.2	0.8	0.6	0.2	1.0	1.0	0.3
E_n [MeV]	95.6	73.8	175.5	144.8	65.5	133.8	174.0	95.7
d(Li) [mm]	4	4	15	15	4	15	15	4
A [10^{-3}]	7.0		5.0	5.3		5.0	5.3	7.0
Foils in the stack	Cu	Cu	Cu	Cu	Cu	Cu	Cu	Cu
	Te	Ag	Ag	Ag	U	U	U	U
	Cu	Cu	Cu	Cu	Cu	Cu	Cu	Cu
	Mg	Co	Co	Co				
	Cu	Cu	Cu	Cu				
	Pb	Mg	Mg	Mg				
	Cu	Cu	Cu	Cu				
	Ni	Pb	Pb	Pb				
	Cu	Cu	Cu	Cu				
	Fe	Ni	Ni	U				
	Cu	Cu	Cu	Cu				
	C	Fe	Fe	Ni				
	Cu	Cu	Cu	Cu				
	SiO_2	Al	Al	Fe				
	Cu	Cu	Cu	Cu				
		C	C	Al				
		Cu	Cu	Cu				
		SiO_2	SiO_2	C				
		Cu	Cu	Cu				
				SiO_2				
				Cu				
Lenght [mm]	46.0	49.0	50.0	50.12	5.12	4.96	5.12	5.12